PEOPLE'S DEMOCRATIC REPUBLIC OF ALGERIA

MINISTRY OF HIGHER EDUCATION AND SCIENTIFIC RESEARCH

UNIVERSITY SAAD DAHLEB BLIDA 1

INSTITUTE OF AERONAUTICS AND SPACE STUDIES

DOCTORAL THESIS IN AERONAUTICS

Option: Avionics

Presented by **CHENAOUI Safia**

WIDEBAND AND MULTIBAND ANTENNAS FOR AEROSPACE APPLICATIONS

Jury:

President	OTMANE Fadhéla	MCA	University of Blida 1
Director	MOUFFOK Lila	MCA	University of Blida 1
Co-Director	HEBIB Sami	Professeur	University of Blida 1
Examiner	ADANE Amar	MCA	USTHB
Examiner	MANSOUL Ali	Directeur de recherche	CDTA

The dissertation defense will take place on Wednesday, october the 23rd,2024 in the conferences room of the IAES institute.

Blida,october 2024

Acknowledgements

Praise be to the Almighty God who has given me faith, courage, and patience to carry out this work.

I want to express my deep gratitude to my supervisors Dr. Lila MOUFFOK and Pr. Sami HEBIB for their unwavering guidance, insightful feedback, and endless patience. Their expertise, encouragement, and constructive remarks for the good progress of this work.

I extend my sincere appreciation to laboratory LCIS in France and their research groups for their support. Their expertise, resources, and collaborative spirit have greatly contributed to the success of this research endeavor.

Special thanks to Dr. Pierre Lemaître-AUGER, Pr. Smail TDJINI and Dr.Dahmane ALLANE for providing me invaluable advice and resources throughout the research process.

I am also immensely grateful to the members of my thesis committee, for their valuable insights, constructive criticism, and dedication to ensuring the rigor and integrity of this work. Their collective expertise has significantly enriched the scope and depth of this study.

Finally, I express my deep gratitude to my parents, my brothers, my sisters,my friends and my whole family for their encouragement and prayers that allowed me to achieve this modest job. I am very grateful for the confidence they have placed in me.

Dedication

I dedicate this work to my parents:

May they find here the testimony of my deep gratitude and acknowledgment

To my brothers and my sisters, my grandparents and my family who give love and liveliness.

To all those who have helped me - directly or indirectly - and those who shared with me the emotional moments during the accomplishment of this work and who warmly supported and encouraged throughout my journey.

To all my friends who have always encouraged me, and to whom I wish more success.

Thanks!

Safia CHENAOUI

Abstract

In the aerospace field, the use of compact, low cost and lightweight devices is essential. Printed antenna technology meets these criteria due to its ease of integration into modern wireless systems as satellite communication, mobile communication or RFID systems. Moreover, the implementation of various functions such as localization, communication, and navigation necessitates placing multiple printed antennas on a limited space. All these constraints need specific requirements in terms of frequency and radiation characteristics. One conceivable solution is the use of microstrip wideband or multiband antenna backed with artificial reflectors. This solution overcomes aerodynamic constraints by reducing the thickness of directive antennas and eliminating the need of quarter-wavelength distance between the antenna and its reflector. The objective of this thesis is to propose novel antenna structures based on wideband and multiband artificial reflectors which is a crucial challenge. The first study concentrates on designing artificial reflectors for wideband antennas, with a specific focus on achieving a stable gain in the whole target band, reducing significantly the antenna thickness and enhancing the front-to-back ratio. The first prototype propose a directive low profile bowtie antenna backed with a novel AMC reflector for aerospace C-band applications. It allows a stable gain with a variation of only 0.85 dB over a wide impedance bandwidth of 50% (3.94–6.61 GHz) while maintaining a low profile of $0.084\lambda_L$ (λ_L is the wavelength at 3.94 GHz). The second structure is dedicated to UHF-RFID applications, where the AMC allowed a reduction of 45% of the antenna profile height while maintianing high gain and a front-to-back ratio of more than 5 dB and 24 dB, respectively, across the entire UHF-RFID band. The second study proposes the design of two prototypes using multiband artificial reflectors. A trap-loaded pyramidal antenna backed with a triband artificial magnetic conductor is designed for GNSS system. The triband AMC reflector has been proposed to replace the bulky metallic cutoff open-ended waveguide used in a previous version of the pyramidal

antenna. Indeed, a significant reduction in the overall antenna size by 37%, 37% and 67% along x, y, and z-axes, respectively, is achieved while maintaining similar performances. Finally, a dual-band antenna associated with a dual-band AMC reflector for 5G systems is proposed for gain enhancement. The proposed structure exhibits a broadside gains of 6.83 dB and 5.20 dB at the operating frequencies of 3.40 GHz and 6.10 GHz, respectively. The proposed Antenna structures have been simulated using CST Microwave Studio software, fabricated, and measured, confirming their proper operation.

Keywords: Bowtie antenna, gain stability, pyramidal antenna, multiband antenna , triband AMC reflector, UHF-RFID U-slot antenna, wideband antenna, , wideband AMC reflector.

Résumé

Dans le domaine aérospatial, l'utilisation de dispositifs de télécommunications légers, peu encombrants et de faible coût est primordiale. La technologie des antennes imprimées permet de répondre à ces critères grâce à leur facilité d'intégration dans divers systèmes modernes sans fil tels que les communications satellitaires, communication mobile ou RFID. D'autre part, la mise en œuvre de nombreuses fonctions telles que la localisation, les communications et la navigation se traduit par une nécessité d'implanter de nombreuses antennes imprimées sur des dispositifs à espace limité. L'ensemble de ces contraintes nécessite des besoins spécifiques en termes de bande passante et d'efficacité de rayonnement. L'objectif de ce travail de thèse de doctorat est de pallier à ces contraintes, par la conception de nouvelles structures d'antennes compactes large-bandes et multi-bandes associées à des réflecteurs artificiels, ce qui est un véritable chalenge.

Dans un premier temps, la conception d'un réflecteur artificiel large bande associé à une antenne bowtie a permis d'avoir un gain stable avec une variation de 0.85 dB (variant entre 5.9 et 6.75 dB) sur une largeur de bande relative de 50% (3,94 - 6,61 GHz), en présentant une épaisseur de $0.084\lambda_L$ (avec λ_L la longueur d'onde correspondante à 3.94 GHz). Ensuite, la conception d'un AMC (Artificiel Magnétique Conducator) large bande pour les applications RFID (860-960 MHz) a permis la réduction de 45% de l'épaisseur de l'antenne initiale avec un gain élevé et un rapport avant-arrière de plus de 5 dB,24 dB sur l'ensemble de la bande UHF-RFID.

D'autre part, une réflectrice artificielle tri-bande a été proposée pour remplacer le guide d'onde d'une antenne pyramidale, pour les systèmes GNSS. Le guide d'onde a été utilisé initialement pour éliminer le rayonnement arrière. Une réduction significative de la taille globale de l'antenne de 37%, 37% et 67% le long des axes x, y et z est obtenue, tout en maintenant des performances similaires. Enfin, une antenne bi-bande associée à un réflecteur AMC bi-bande pour les systèmes 5G à été conçue afin d'améliorer les gains. Cette structure présente un gain de 6.83 dB et de 5.20 dB aux fréquences de fonctionnement de 3.40 GHz et 6.10 GHz, respectivement. Les prototypes

d'antennes ont été simulés avec le logiciel CST Micro ave Studio, réalisés et mesurés confirmant ainsi leur bon fonctionnement.

Mots clés : Antenne large bande, stabilité du gain, antenne pyramidale, antenne U-slot UHF-RFID, antenne à large bande, antenne multi-bande, réflecteur AMC large bande, réflecteur AMC tri-bande, trappes, réflecteur AMC à fentes.

ملخص

في مجال الطيران والفضاء، يعتبر استخدام الأجهزة الصغيرة الحجم والمنخفضة التكلفة والخفيفة الوزن أمراً ضروريا. تلبي تكنولوجيا الهوائيات المطبوعة هذه المعايير بسبب سهولة دمجها في أنظمة الاتصالات ، اللاسلكية الحديثة مثل الاتصالات الفضائية وشبكات الاتصالات المتنقلة و أنظمة RFID. علاوة على ذلك، يتطلب أدائها وظائف متعددة مثل: التحديد والاتصال ، الملاحة والتوجيه ، وضع العديد من الهوائيات المطبوعة على مساحة محدودة. جميع هذه القيود تتطلب متطلبات محددة فيما يتعلق بعرض النطاق الترددي وكفاءة الإشعاع. إحدى الحلول الممكنة هي استخدام هوائيات النطاق العريض أو متعددة النطاقات المدعومة برفلكتور اصطناعي. تتغلب هذه الحلول على القيود الديناميكية عن طريق تقليل سمك الهوائيات والتخلص من الحاجة إلى مسافة ربع طول موجة بين الهوائي ورفلكتور. هدف هذه الرسالة هو اقتراح نماذج هوائية جديدة مبتكرة تعتمد على رفلكتورات AMC صناعية عريضة ومتعددة النطاقات وهو تحدي حاسم. الدراسة الأولى مركزة على تصميم الرفلكتورات الاصطناعية للهوائيات عريضة النطاق، مع التركيز الخاص على تحقيق اكتساب ثابت في النطاق المثير للاهتمام بأكمله وتقليل سمك الهوائي مع تحسين نسبة نسبة الأمام إلى الخلف. يقترح النموذج الأول هوائي على شكل الفراشة مدعوم برفلكتور AMC جديد لتطبيقات الفضاء نطاق C. يسمح بكسب مستقر مع تباين يبلغ 0.85 dB فقط على عرض نطاق مقاومة واسع بنسبة 50%. بالإضافة إلى ذلك، يحقق ارتفاعاً منخفضاً بقيمة $0.084\ \lambda_L$ حيث λ_L هو الطول الموجي عند 3.94 GHz. النموذج الثاني هوائي الفتحة U مخصص لتطبيقات UHF-RFID حيث سمح AMC رفلكتور اصطناعي بتقليل 45% من سمك الهوائي. بالإضافة إلى ذلك، حقق ارتفاعاً في الكسب ونسبة نسبة الأمام إلى الخلف تزيد عن 5 dB، 24 dB عبر كامل نطاق UHF-RFID. الدراسة الثانية تقترح تصميم اثنين من النماذج باستخدام رفلكتورات اصطناعية متعددة النطاقات. تم تصميم هوائي هرمي مدعوم برفلكتور AMC اصطناعي ثلاثي النطاقات لنظام GNSS(GPS/GALILEO/MicroSat).

تم اقتراح رفلكتور ثلاثية النطاقات لتحل موجّه الموجة المستخدم في النسخة السابقة من الهوائي الهرمي. في الواقع، تم تحقيق تقليل كبير في حجم الهوائي الإجمالي بنسبة 37% على طول محاور X و Y و 67% على Z على التوالي، مع الحفاظ على الأداء المماثل. بالإضافة إلى ذلك، يُقدم

هوائي ذو النطاق المزدوج المقترن رفلكتور اصطناعي مغناطيسي مزدوج النطاق لتطبيقات الجيل الخامس تحت 6 GHz (n78) وتحت 7 GHz (n96) يتم تحميل AMC رفلكتور اصطناعي مغناطيسي على ظهر نموذج الهوائي لتعزيز كسبه. يظهر التكوين المقترح كسب بمقدار 6.83 dB و 5.20 dB عند الترددين التشغيليين 3.40 GHz و 6.10 GHz، على التوالي. تمت محاكاة نماذج الهوائي باستخدام برنامج CST Microwave Studi، وتم تصنيعها وقياسها، مما يؤكد أدائها السليم.

كلمات مفتاحية: هوائي الفراشة، إستقرار الكسب، هوائي هرمي، هوائي الفتحة U UHF-RFID ، هوائي عريض النطاق، هوائي متعدد النطاقات AMC رفلكتور عريض النطاق، AMC رفلكتور متعدد النطاقات .

Contents

List of Figures

List of Tables

List of Abbreviations

AMC:	Artificial magnetic conductor
AUT:	Antenna Under Test
BALUN:	Balnced-Unbalanced
BLTSA:	Broken Line Tapered Slot Antenna
BW :	Bandwidth
CPS:	Coplanar stripline
CPW:	Coplanar Waveguide
CRLH-TL:	Composite Right/Left-Handed-Transmission line
CRPA:	Controlled Radiation Pattern Antennas
CSRR:	Complementary Split Ring Resonator
CST:	Computer Simulation Technology
CW:	Clockwise
CCW:	Counterclockwise
CWSA:	Constant Width tapered Slot Antenna
DUT:	Device Under Test
DGS:	Defected Ground Structure
EBG:	Electromagnetic Band Gap
ESM:	Electronic Support Measures
ETSA:	Exponentially Tapered Slot Antenna
F/B:	Front-to-back ratio
FEM:	Finite Element Method
FIT:	Finite Integration Technique
FNBW:	First-Null Beamwidth
FDTD:	Finite Difference Time Domain
GPS:	Global Positioning System
GNSS:	Global Navigation Satellite System
HPBW:	Half-Power Beamwidth

HIS: High Impedance Surfaces
IEEE: Institute of Electrical and Electronics Engineers
ISM: Industrial Scientific and Medical
ITU: International Telecommunication Union
LHCP: Left Hand Circular Polarization
LSP: Ladder Slotted Patch
LTSA: Linearly Tapered Slot Antenna
MCS: Microstrip line
MCS: Modifieed Crossed-Shaped
MOM: Method of Moments
MIMO: Mltiple Input Multiple-Output
MSA: Microstrip antenna
MVG: Microwave Vision Group
MWS: Microwave Studio
PBC: Periodic Boundary Conditions
PCB: Printed Circuit Board
PEC: Perfect Electric Conductor
PIFA: Planar Inverted-F Antenna
PMC: Perfect Magnetic Conductor
RADAR: RAdio Detection And Ranging
RADALT: Radio Altimeter
RFID: Radio Frequency Identification
RHCP: Right Hand Circular Polarization
RSRR: Rectangular Split Ring Resonator
RUAG: Rüstungs Unternehmen Aktiengesellschaft
SAR: Specific Absorption Rate
SMA: SubMiniature version A
SPA: Suspended Plate Antenna
SRR: Split Ring Resonator
SSP: Standard Square Patch
SST: Surrey Satellite Technology
SATIMO: Société d'Applications Technologiques de l'Imagerie Micro-Onde
TE: Transverse Electric
TM: Transverse Magnetic

TSA: Tapered Slot Antenna
UAV: Unmanned Aerial Vehicle
UHF: Ultra High Frequency
VIA: Vertical Interconnect Access
VSWR: Voltage Standing Wave Ratio.
WLAN: Wireless Local Area Network
WIMAX: Worldwide Interoperability for Microwave Access
WBAN: Wireless Body Area Network
WIFI: Wireless Fidelity.

General introduction

In an era defined by rapid technological evolution and growing demands in aerospace communications, the design of antennas capable of operating across a wide frequency band with multifunction capabilities has emerged as an essential research area. The aerospace domain, encompassing satellite communications and unmanned aerial vehicles (UAVs), requires antennas that can efficiently transmit and receive signals while adhering to strict performance criteria related to bandwidth and radiation efficiency within a confined space. One of the potential solutions lies in the use of wideband or multiband antennas with artificial magnetic reflector (AMC) technology. The AMC is a periodic structure commonly positioned behind the antenna to serve as a reflector. This structure helps overcome aerodynamic constraints by reducing the thickness of directive antennas and eliminating the need for a quarter-wavelength distance between the antenna and its reflector. In addition, a good radiation efficiency is preserved since the reflection coefficient of the structure is equal to +1. However, the major drawback of these materials is their "narrowband" operation. Unlike a conventional single-band AMC reflector, which typically feature only one zero-phase in the reflection coefficient, multiband AMC reflector require two or more zero phases. Therefore, achieving desirable performance across multiple operating bands is quite a challenging task.
The current research aims to introduce innovative AMC structures for miniaturizing and enhancing the performance of wideband and multiband antenna solutions. These solutions are not limited to the aerospace sector but also extend to the field of telecommunications. Indeed, modern wireless systems such as 5G and RFID systems require compact wideband and multiband antennas with improved characteristics, making the task particularly challenging. Several contributions have been explored in this thesis, which can be categorized into two main parts, focusing on the investigation of wideband and multiband antennas based on AMC reflectors. The aim is to enhance gain stability, achieve low profile and miniaturization, and reduce backward radiation. Through this exploration, four antenna prototypes based on AMC reflectors have been developed.

The first part is dedicated to examine the efficacy of wideband AMC surfaces when employed as reflectors for wideband antennas, with a specific focus on their potential advantages in stabilizing gain, reducing the antenna profile height and enhancing the front-to-back ratio. Therefore, two antenna prototypes have been proposed, the first prototype is a directive low profile bowtie antenna backed with a novel AMC reflector for aerospace C-band applications. By integrating the AMC surfaces as reflector, a stable gain is achieved with a low gain variation of only 0.85 dB across a wide impedance bandwidth of 50% (3.94 – 6.61 GHz). The second prototype is dedicated to achieving a low profile UHF-RFID reader antenna with high front-to-back ratio using an original slotted AMC reflector. The AMC allowed a reduction of 45% the antenna thickness compared to the initial design without AMC reflector while maintaining high gain and a front-to-back ratio of more than 24 dB across the entire UHF-RFID band.

The second part is dedicated to introducing the potential of multiband AMC reflectors when employed as reflectors for multiband antennas, focusing on their advantages in miniaturization, reducing backward radiation, and enhancing gain across multiple operating bands. Therefore, two multiband antenna prototypes have been proposed. In the first prototype, a trap-loaded pyramidal antenna backed with a triband artificial magnetic conductor is designed for GNSS system (GPS/GALILEO/MicroSat). The triband AMC reflector serves as an alternative solution to the bulky metallic cutoff open-ended waveguide used in a previous version of the pyramidal antenna. Significant reduction in the overall antenna along the x, y, and z-axes are achieved while maintaining reduced backward radiation across the three operating frequencies (1.197 GHz, 1.575 GHz, 2.245 GHz) intended for GPS/GALILEO/MicroSat. Additionally, in the second prototype, a dual band slotted monopole antenna associated with dual band artificial magnetic conductor (AMC) reflector-based SRR structures is presented for 5G application (sub 6 GHz (n78)-sub7 GHz (n96)). The AMC reflector is loaded on the back of the antenna structure to enhance gain. The proposed configuration exhibits enhanced directional gain across the two operating frequency, affirming the effectiveness of the AMC reflector in enhancing gain across multiple bands.

Throughout this work, various forms of AMC surfaces have been proposed to meet our objectives. The selection of these AMC shapes is based on the surface current methodology, which plays a significant role in explaining the degradation of antenna

performance. Additionally, several parametric studies and optimizations have been conducted to achieve our desired performance. The antenna prototypes have been simulated using CST Microwave Studio software, fabricated, and measured, confirming their proper operation. Finally, the obtained results were compared to similar published works, demonstrating the highly attractive performance of the AMC reflector across various applications.

This thesis is organized as follows: the first chapter introduces wideband and multiband microstrip antenna designs. It covers a basic knowledge of microstrip antenna design, including characteristics, feeding techniques, and the most effective methods to achieve wideband and multiband behavior. Additionally, it provides an overview of the most useful wideband and multiband antennas in aerospace applications. The second chapter introduces artificial reflectors. Firstly, it highlights the limitation of conventional reflectors then reflectors based on artificial materials are presented as solution. This section includes definitions and the analytical and numerical methods. It also provides an overview of wideband and multiband antennas based on these artificial materials. The third and fourth chapter are devoted to highlight the contribution of AMC to enhance the performances wideband and multiband antenna, focusing on enhancing specific key features including: bandwidth and gain enhcmenents, gain stabilization, achieving low profile and miniaturization and reducing the backward radiation.
Finally, a conclusion is provided at the end of this thesis, summarizing the main results obtained and offers insights into future research directions.

Chapter 1

Microstrip wideband and multiband antennas

1.1 Introduction

Progress in frequency band multiplication has generated a growing need for multiband and wideband antennas. These antennas have gained widespread usage across various applications, particularly in aerospace applications, owing to their versatility, conserving space by combining multiple antennas into one, cost-effectiveness, and ease of integration. However the requirement and the diversity of characteristics of different antenna frequency band such as radiation pattern shapes, polarization type, and required bandwidth, pose a significant challenge in designing these antennas.
This chapter places particular emphasis on wideband and multiband antennas . Initially, wideband antennas are presented, exploring their types and applications within the aerospace domain. Subsequently, our focus shifts to multiband antennas. Finally, we draw conclusions through a comparative analysis, selecting the most pertinent techniques for acquiring required antennas.

1.2 Microstrip wideband antenna

Microstrip Antenna (MSA) consists of a radiating patch on one side of a dielectric substrate and a ground plane on the other side. Figure 1.1 illustrates the top and side view of a rectangular MSA . These antennas are often referred to as patch antennas, their radiating elements and feed lines are typically printed on the dielectric substrate.

The radiating patch can take various shapes, including square, rectangular, thin strip (dipole), circular, elliptical, triangular, or any other configuration, as depicted in Figure 1.2. Among these shapes, square, rectangular, dipole (strip), and circular configurations are the most common due to their ease of analysis and fabrication, as well as their favorable radiation characteristics, particularly low cross-polarization radiation. [1, 2].

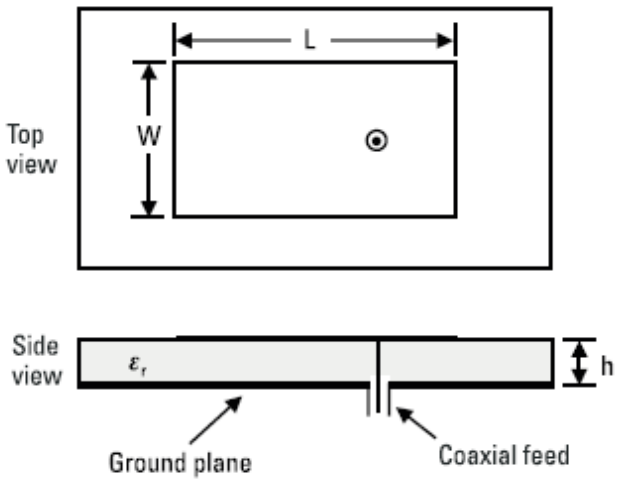

Figure 1.1: MSA configuration [1].

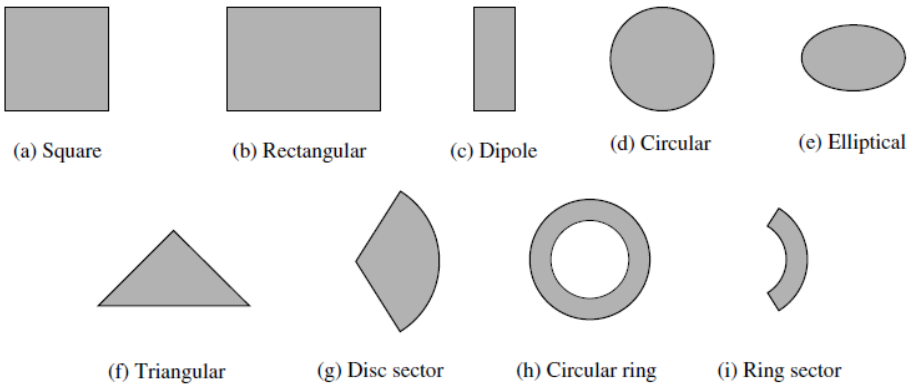

Figure 1.2: Various shapes of microstrip patch antenna [2].

The concept of the MSA was initially proposed by Deschamps in 1953 [3]. However, practical antennas based on this concept were developed by Munson [4, 5] and Howell [6] in the 1970s. They feature several important advantages including [7]:

- Low profile: their thickness is typically less than 0.03 λ_0 (λ_0 is the guided wavelength

in free space) which making it very suitable for applications where space is limited or where a low profile antenna is desired.

• Light weight: they are typically constructed from perfectly electrically conducting (PEC) foil attached to a dielectric substrate.

• Low cost: they are commonly fabricated using inexpensive printed circuit techniques.

• Ease of integrate: it can be integrated into a printed-circuit board (PCB) alongside other planar circuits.

• Versatility: microstrip patch antennas offer versatility in terms of impedance, resonant frequency, radiation pattern, polarization, and operating mode. This versatility is achieved through various design parameters such as shape and feeding arrangement.

Microstrip antennas have attracted much attention from researchers and engineers due to their advantages. They are highly suitable for numerous applications where size, weight, cost, performance, ease of installation are required including: aircraft, spacecraft, satellite, and missile applications, radio-frequency identification (RFID), multiple input multiple-output (MIMO) systems, vehicle collision avoidance system, satellite communications, surveillance systems, direction founding, radar systems, remote sensing, biological imaging, guidance [1]:

• In missile technology, MSAs serve as telemetry and communication antennas, offering the advantage of being thin and conformal, thus meeting strict design requirements.

• Radar altimeters utilize compact arrays of microstrip radiators, benefiting from the efficient and compact nature of MSAs.

• Aircraft applications often rely on MSAs for antennas in telephone and satellite communications systems (GPS receiver), where their lightweight and low profile design are advantageous. MSAs are integral components in satellite imaging systems, providing reliable and efficient performance in space applications. Smart weapon systems also can benefit from the thin profile of MSAs, enabling their integration into weapon platforms without compromising performance. Despite their advantages, they are constrained by several limitations like: low gain and poor impedance bandwidth. Narrow impedance and radiation bandwidths are the main drawbacks of microstrip patch antennas, caused by frequency-dependent efficiency, radiation direction, or polarization characteristics and restrict their applications. However, significant efforts have been dedicated to developing broadband techniques to overcome narrow bandwidth limitations and enhance their performances which is the emphasis of of section 1.4.

1.3 Feeding methods

Microstrip antennas employ various feeding techniques to deliver power to the radiating patch. They can be excited through direct methods such as a coaxial probe or a microstrip line. Alternatively, indirect excitation methods involve electromagnetic coupling or aperture coupling in which the metallic contact between the feed line and the patch is not required. Figure 1.3 illustrates the four most popular techniques used to feed the micrpostrip antenna [2].

Figure 1.3(a), shows a patch antenna excited by microstip line. This line can be etched on the same substrate, so the total structure remains planar. In addition, it is easy to fabricate, simple to model. The main drawback of this technique is that as the substrate thickness increases, certain undesirable effects can occur. Specifically, surface waves and spurious feed radiation tend to increase with thicker substrates. These phenomena contribute to limitations in the antenna's bandwidth, which is typically constrained to a narrow range, often between 2% and 5%.

The coaxial or probe feed is shown in Figure 1.3(b). In this feeding technique, the inner conductor of the coaxial cable is connected to the radiation patch, while the outer conductor is linked to the ground plane. Coaxial probe feeds offer several advantages, including ease of fabrication and matching, as well as minimal spurious radiation. However, they also exhibit limitations such as: narrow bandwidth and increased complexity in modeling, particularly for thicker substrates. Both microstrip feed line and coaxial probe feeding methods exhibit asymmetries, leading to the generation of higher-order modes that result in cross-polarized radiation. To address these challenges, non-contact aperture-coupling feeds are employed (see Figure 1.3(c) and Figure 1.3(d)).

Figure 1.3(c), illustrates the third technique used to feed the microstrip antenna. In this method, power is coupled to the radiating patch through electromagnetic coupling between the feed line and the patch. The feed line is positioned between the patch and the ground plane, which are separated by two dielectric substrates. The proximity coupling method offers the largest bandwidth among the feeding techniques for microstrip antennas, reaching up to 13%.

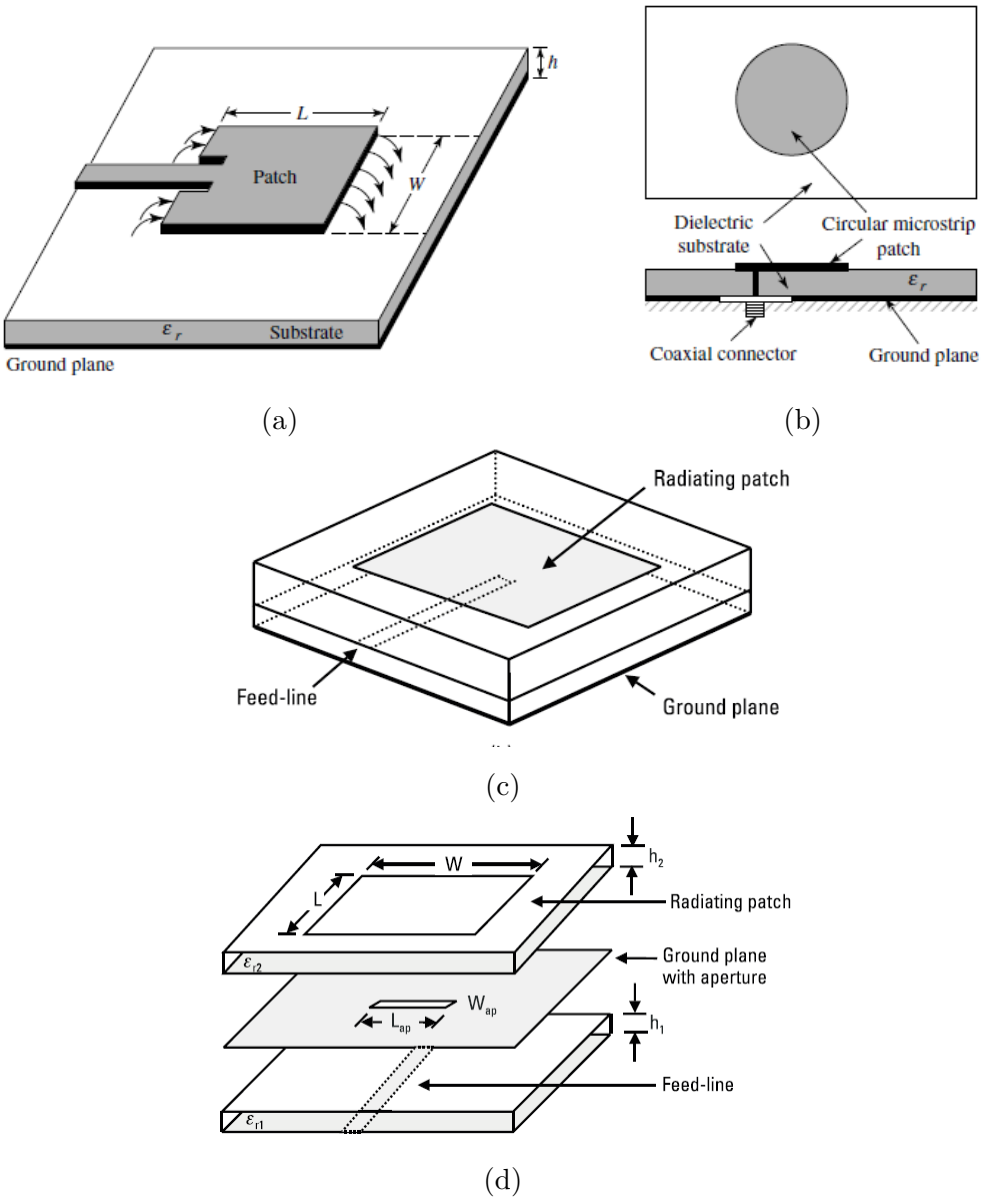

Figure 1.3: Feeding techniques of microstrip antenna [1], (a) Microstip line, (b) Probe feed, (c) The proximity-coupled feed, (d) Aperture-coupled feed

It is easy to model and exhibits low levels of unwanted radiation. However, its fabrication process is more complex compared to other feeding techniques. Additionally, proper alignment of the two layers is necessary, which results in an overall increase in the thickness of the antenna. Another method for indirectly exciting a patch utilizes aperture coupling. In the aperture-coupled microstrip antenna configuration, the field is transferred from the microstrip line feed to the radiating patch through a small aperture or slot cut in the ground plane. This configuration is depicted in Figure 1.3(d).

Typically, the coupling aperture is positioned centrally under the patch, which promotes lower cross-polarization owing to the symmetry of the setup. one disadvantage of the aperture-coupled MSA configuration is the complexity of fabrication compared to other feeding techniques. Aligning the coupling aperture accurately with respect to the radiating patch requires precision manufacturing processes, increasing the cost and complexity of production. Moreover, the design of aperture-coupled MSAs may be sensitive to substrate thickness and dielectric properties, making optimization challenging [2].

1.4 Broadband techniques for microstrip antenna

The operation of an antenna within a frequency band typically involves a reasonable matching of the antenna for all frequencies within the band. This matching is defined by a reflection coefficient or a Voltage Standing Wave Ratio (VSWR) at the antenna input that is lower than a specified value. (commonly: -10 dB, -15 dB, or -20 dB for the reflection coefficient, and 2, 1.5, 1.2 for the VSWR). The antenna bandwidth (matching bandwidth) is the ability of the antenna to extract from a generator or transmit to a receiver a maximum amount of energy. It can be expressed either relatively (1.1) or absolutely (1.2):

$$BW = \frac{2(f_{max} - f_{min})}{(f_{max} + f_{min})} \tag{1.1}$$

$$BW = \frac{f_{max}}{f_{min}} : 1 \tag{1.2}$$

Where, f_{max} and f_{min} are the upper and lower transmitted frequencies at -10 dB . An antenna can be considered "wideband" when it covers at least 5% of the bandwidth or an octave, depending on the criteria chosen. The development of wideband antennas traces its origins to the 1940s, marking a significant evolution in antenna technology. Since then, multiples categories of printed wideband antennas have explored, each offering unique advantages and applications.

Multiple broadband techniques have been developed to broaden the impedance bandwidth of microstrip antenna such as: shapes radiators, inserting matching network, using suspended plate antenna, using slotting and notching antenna and using parasitic elements.

1.4.1 Shape radiator

Radiator shape can affect the antenna input characteristics and frequency band. Broadband performance can be achieved through gradual geometrical modifications like: frequency independent antennas and progressive transition antennas or using monopole antennas [7].

a Frequency independent antennas

Frequency independent antennas are wideband antennas whose geometry is defined by angles and are considered to have infinite dimensions. Their operation is based on the principle that if all dimensions of the structure are modified by a factor K, only the resonance frequency will be shifted by the same factor. They are characterized by presenting a radiation pattern, input impedance, and polarization virtually unchanged over an almost infinite frequency band. As an example of this class of antennas, two major groups can be noted: equiangular antennas (such as the logarithmic spiral antenna, Archimedes antenna) and log-periodic antennas [8], as it is shown in Figure 1.4 .

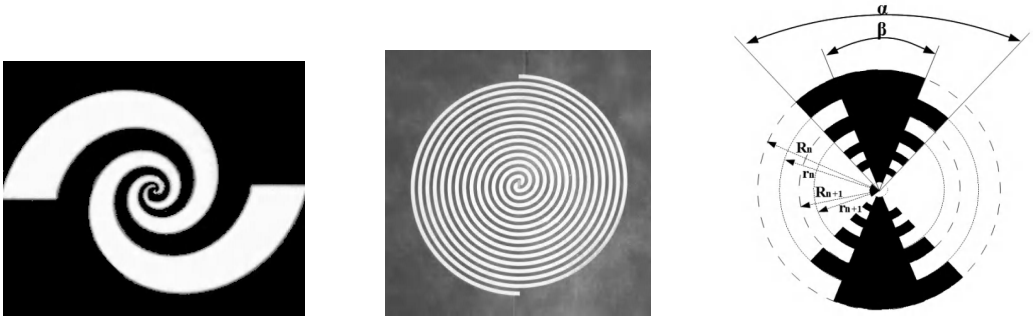

(a) (b) (c)

Figure 1.4: Equiangular antenna types: (a) Log-spiral antenna, (b) Archimedes spiral antenna, (c) log perioidc antenna (circular log-periodic antenna)[8].

b Antennas with progressive transition

They typically consist of a line that matches the antenna's feeding system, followed by a transition section compared to an impedance transformer. This transition section raises the structure's characteristic impedance to that of free space. The flared shape of this transition creates a radiation aperture that matches the impedance of free space. Its design aims to minimize reflections at the structure's end [8].

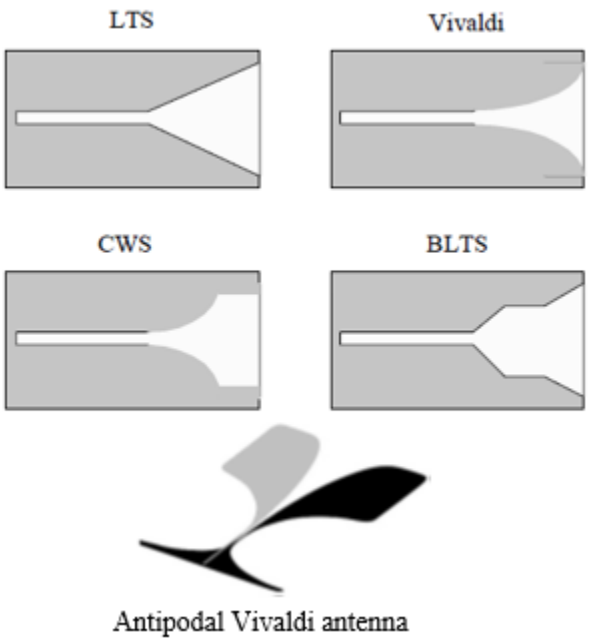

Figure 1.5: Tapered slot antenna types [8].

Tapered Slot Antennas (TSA) are planar structures that feature a transition starting from a printed line or waveguide. They were first introduced in 1974 by Lewis and Gibson with the Vivaldi antenna. Typically, they consist of a line with slot widening gradually until reaching a final discontinuity, following a specific profile. Therefore, the Vivaldi antenna, also known as the ETSA (Exponentially Tapered Slot Antenna), features an exponential or elliptical transition profile and is known for its low cross-polarization. However, other types of transitions have been studied as it is illustrated in Figure 1.5 , such as: Antipodal Vivaldi antenna , the linearly tapered slot antenna (LTSA), broken line tapered slot antenna (BLTSA), or exponentially tapered slot antenna with a constant width (CWSA).

c Elementary antennas

The antennas referred to as "elementary" are essentially an advancement from basic dipoles or monopoles, whose characteristics are widely known in electromagnetic community. This category of antennas is undoubtedly employed in communications due to their ability to maintain the desirable characteristics of an omnidirectional radiation as well as relatively compact structures. In this category, we can mention monopoles antennas which can take various shapes [8], such as: circular, elliptical, triangular, trapezoidal, rectangular and bowtie antenna which we will be particularly interested

in chapter 3. Bowtie antenna, also known as the butterfly antenna, is a planar version of the finite biconical antenna. It is a symmetric and simple structure compared to the infinite biconical antenna. The main advantages of this antenna are its lightweight design, low cost due to its geometric simplicity, and compact size [8].
Bowtie antennas provide notable advantages over monopole antennas, particularly in terms of bandwidth and gain. They typically offer wider bandwidth and higher gain, especially in applications requiring broader frequency coverage. This versatility makes bowtie antennas well-suited for various applications .
The basic bowtie antenna geometry is defined based on three main parameters, (see Figure 1.6):

- α is the escape angle for a butterfly antenna formed by two triangles.
- H is the height of the triangles.
- L is the length of the equal sides of the isosceles triangle.

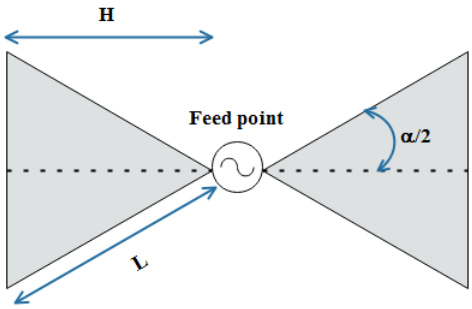

Figure 1.6: Bowtie antenna geometry.

Its input impedance primarily depends upon the flaring angle and the relative bandwidth can exceed 100%. The radiation pattern is similar to a dipole radiation; it is omnidirectional in the plane perpendicular to the antenna with a gain ranging from 0 to 3 dB. The bowtie antenna is a symmetrical (balanced) antenna which requires the use of balanced feeding, leading to the use of balun to adapt the antenna to the feeding system. Different type of wideband balun are suggested including: marched balun [9] , tapered balun [10] and microstrip to CPS (CoPlanar Symmetrical) transition balun [11]. This latter will be detailed in the next section.

1.4.2 Insert matching network

An impedance matching network can be introduced to realize good matching between a radiator having frequency-dependent impedance and a feed structure with a constant characteristic impedance. This naturally leads to a broader bandwidth. In microstrip patch antennas, there are two common approaches (see Figure 1.7). One involves adding a separate matching network without changing the radiator.

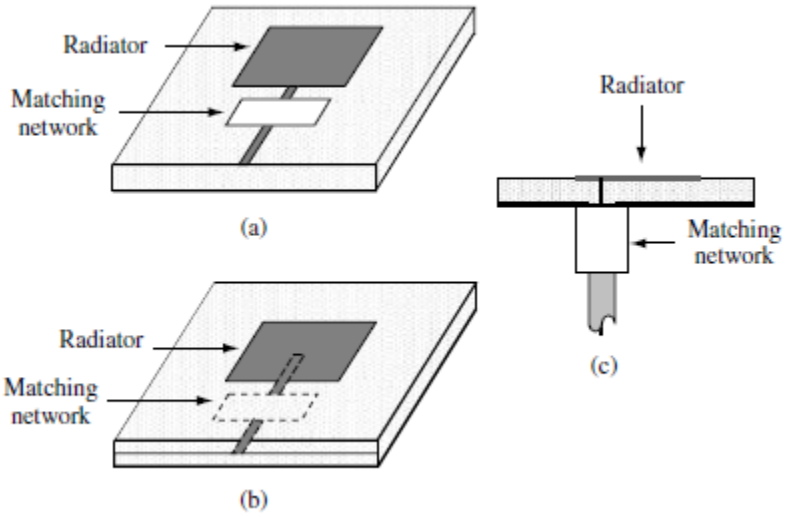

Figure 1.7: Impedance matching networks without modifying the radiators [7]

The other method is to integrate a matching network directly into the radiator by creating slots or notches. Both methods involve inserting an impedance matching network, either lossy or lossless, between the antenna and the feeding structure. This directly enhances the impedance bandwidth of the antenna.This approach is widely employed across different antenna applications [7]. The impedance network can be implemented in various configurations, depicted in Figure 1.7. In Figure 1.7(a) and Figure 1.7(b), the matching network and the feeding strip can be incorporated on the same plane, or separately as shown in Figure 1.7(c). The matching network can be a quarter-wavelength impedance transformer, tuning stubs, active components, or their variants, as illustrated in Figure 1.8(a) and Figure 1.8(b). Adding an on-patch matching network, which involves creating a slot or notch on the radiating patch, effectively forms an inset on the patch.

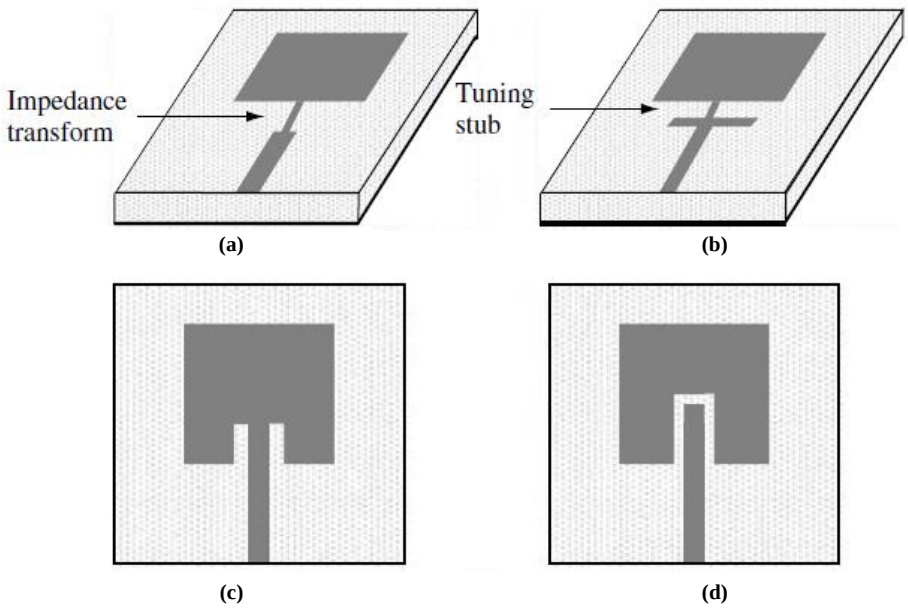

Figure 1.8: Components used in impedance matching networks [7].

This configuration helps in transferring the higher impedance at the radiating edge of the patch to the lower 50 ohm characteristic impedance of the feeding structure [7]. In Figure 1.8(c) and Figure 1.8(d), various inset-fed patches are depicted, featuring striplines as feeding structures. For the bowtie antenna, an impedance matching network like: wideband balun (balanced-unbalanced) is necessary to convert the balanced transmission line to unbalanced, minimizing signal reflections. The chosen balun for the proposed bowtie design in Chapter 3 is a microstrip to CPS (CoPlanar Symmetrical) transition balun. This method is extensively described in [11] and will be elaborated upon here. Figure 1.9 shows electric field lines at various sections along the transition. In a microstrip line, the electric field lines terminate perpendicularly to the substrate ground, as demonstrated in section A'-A. In a coplanar strip (CPS), the electric field lines are concentrated across the two conductive strips, as indicated in D'-D. By gradually modifying the ground plane of the transition (between sections B'-B and C'-C), the electric field lines of the microstrip line transform into CPS as the signal propagates along the transition. It is reported in [11], that to optimally match the characteristic impedances between the microstrip line and the coplanar strip, the ground plane width of the transition is gradually reduced until it aligns with the width of the coplanar strip line containing vias. Therefore, the characteristic impedance of the transition becomes very close to that of the coplanar strip.

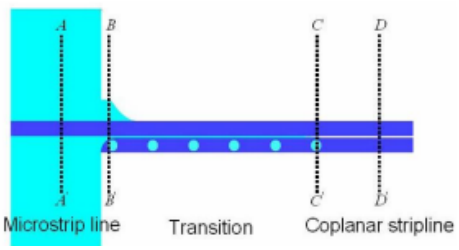

(a)

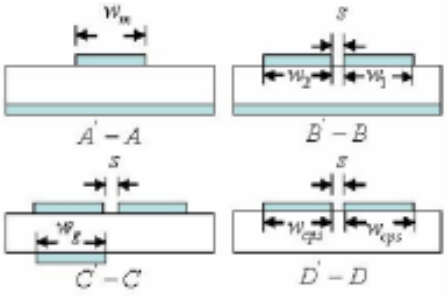

(b)

Figure 1.9: Balun transition concept, (a) Transition structure from microstrip to CPS, (b) Side view of each section [11].

1.4.3 Using suspended plate antenna

The bandwidth of the Microstrip Antenna (MSA) generally expands as the substrate thickness increases and the dielectric constant of the substrate decreases. With a thick substrate and low dielectric constant, a bandwidth ranging from 5% to 10% can be attained. However, it's important to note that, further increases in substrate thickness may lead to decreased efficiency of the MSA and higher levels of cross polarization due to the surface wave propagation [1]. Reducing the permittivity of the substrate offers a practical means to suppress surface waves in antenna designs. By utilizing materials with lower permittivity or incorporating air-filled substrates like foam, engineers can effectively minimize the propagation of surface waves. Foam substrates, with their relative permittivity hovering around 1.07, prove particularly advantageous in this regard. Moreover, the use of air as a substrate further eliminates the surface wave, providing a medium with minimal dielectric properties. This approaches is called, suspended plate antenna. By adjusting the dimensions and geometry of the main radiator, as well as the spacing between this radiator and the ground plane, a broadband impedance matching and radiation characteristics can be achieved,as it is illustrated in Figure 1.10.

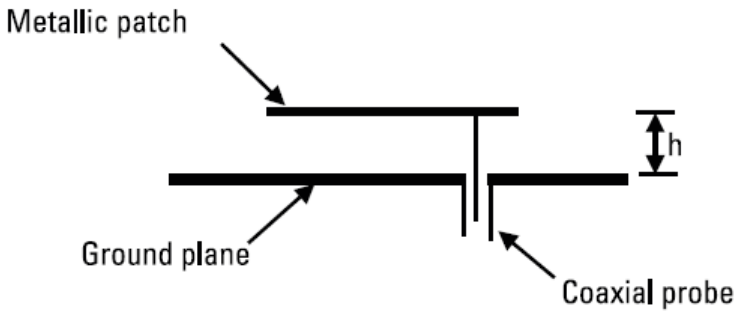

Figure 1.10: MSA suspended in air [1].

1.4.4 Slotting the main radiator

Additional approach used to improve the impedance bandwidth of microstrip patch antenna is by slotting the main radiator (patch). Introducing one slot or multiple slots of various shapes on the radiating plate can significantly introduce additional resonant modes, thereby broadening the antenna's bandwidth. Figure 1.11 illustrates a single-layered single-element Suspended Plate Antenna (SPA) presented by Huynh and Lee in 1995 [12]. The antenna design features a long U-shaped slot symmetrically cut from the radiating plate. This slot serves a crucial role in offsetting the significant input inductance resulting from the long probe. As a result, the SPA achieves an impressive impedance bandwidth ranging between 10% and 40% using only a single layer and without the need for any parasitic elements. This innovative approach highlights the effectiveness of slot-based modifications in enhancing the performance of SPA designs, allowing for broader frequency coverage and improved overall efficiency.

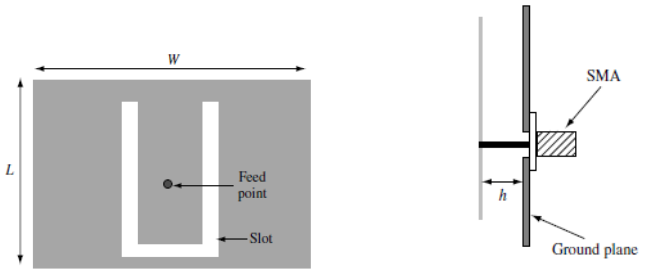

(a) (b)

Figure 1.11: Slotting the main radiator with u-slot shape [1], (a) Top view, (b) side view.

1.4.5 Using parasitic elements

An effective method to enhance the input impedance bandwidth of microstrip patch antennas involves introducing additional radiating patches positioned in close proximity to the main radiator. These supplementary patches, known as parasitic patches, excited through electromagnetic coupling with the main patch. As indicated in Figure 1.12, parasitic patches can be situated in the same plane as the main patch or stacked above it. When placed in the same plane, they interact with the main patch to alter its radiation pattern and the impedance. Alternatively, stacking the parasitic patches above the main patch allows for more intricate control over the antenna's characteristics, such as beam shaping and polarization. By exploiting electromagnetic coupling between the main patch and parasitic patches, antennas can achieve desired performance enhancements without significantly increasing their complexity.

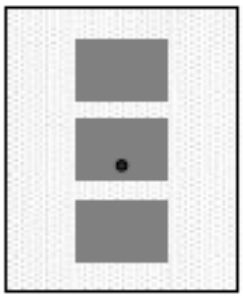

(a)

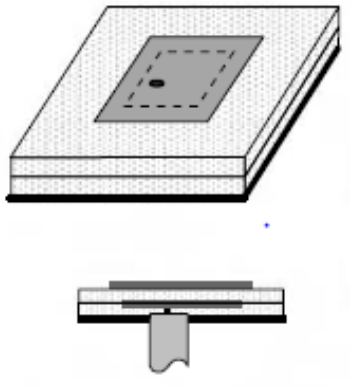

(b)

Figure 1.12: Parasitic element approach for enhancing the impedance bandwidth of MSA [1], (a) Co-planar coupling scheme, (b) Stacked coupling scheme.

1.5 Multiband antennas

Multiple applications like: aerospace applications necessitate the employment of multiple antennas onboard systems and the use of multiple frequency bands. These requirements emphasize the importance of devices capable of covering multiple bands simultaneously, thereby reducing the total number of antennas onboard. For antennas, these devices are known as multiband antennas. A multiband antenna is an antenna that operates in two or more frequency bands with reasonably similar performance across these bands. Several techniques have been employed to achieve multiband behavior, including the use of multiple radiating elements, PIFA (Planar Inverted-F Antenna) types, fractal geometries, and trap-loading techniques. Each of these techniques has its own strengths and weaknesses points, which will be discussed in the next section.

1.5.1 Combining multiple radiating elements

The most classic technique for obtaining multiband antennas is the combination of two or more single band radiating elements (resonators). Each element create their own resonance frequency, resulting in multiband behavior. These single band elements can be of the same type [13, 14] or different from each other[15, 16] (see Figure 1.13). Further, there is multiple techniques to place the radiating element, especially for the case of printed antenna, it can be placed in two different ways: either these elements are juxtaposed in the same plane [17] , or they are stacked on top of each other[18, 19, 20, 21].

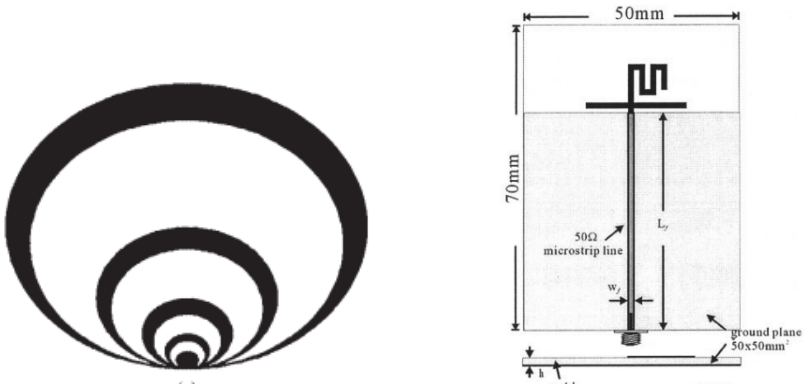

(a) (b)

Figure 1.13: Parasitic elements configurations, (a) Same type of parasitic elements [13] ,(b) Different types of parasitic elements [15].

The elements constituting these multiband antennas can be fed in two different ways: direct feeding through an excitation port (active elements) or feeding through electromagnetic coupling with a neighboring radiating element that is directly fed (parasitic or passive elements). This techniques gives advantages like : good efficiency with uniform radiation across the entire covered bandwidth but it also exhibits some limitations including :bulky structures with complexity in positioning of the various radiating elements.

1.5.2 Planar Inverted-F Antenna (PIFA)

The Planar Inverted-F Antenna (PIFA) is a compact antenna with simple profile used for realizing multiband antennas. The PIFA antenna is achieved by placing a short circuit (plane, wire, or tab-type) between the half-wave resonator and the ground plane. It finds wide applications in wireless communication devices such as mobile phones [22, 23, 24]. However, a major drawback of these antennas is their narrow bandwidth [25]. Moreover, PIFA antennas are complex, and their volumetric (3-dimensional) configuration makes their fabrication difficult and costly [26]

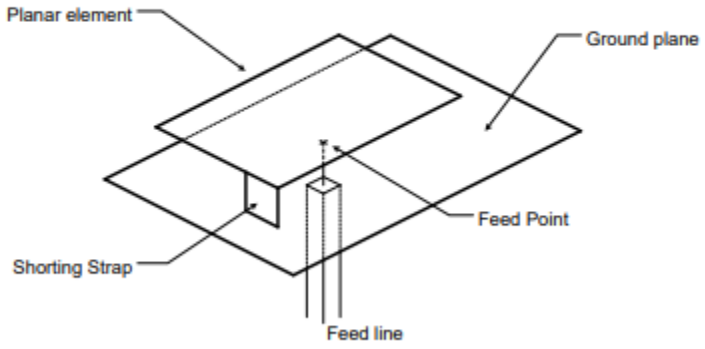

Figure 1.14: Basic Planar Inverted-F Antenna (PIFA) [22].

An elementary PIFA antenna, like the one shown in Figure 1.14, is single band. To achieve the multiband behavior, several techniques can be used, including: modification of the radiating element (triangles [27], meanders [28]), addition of short circuits [29], addition of parasitic resonators [30], insertion of slots in the radiating element [31] and using of localized or distributed capacitive/inductive loading [32].

1.5.3 Fractal antennas

Fractal geometry is an extension of Euclidean geometry. Its introduction has provided antenna designers with an opportunity to explore new antenna configurations. The antennas may exhibit fractal-like shapes due to iterative processes (infinite iteration).

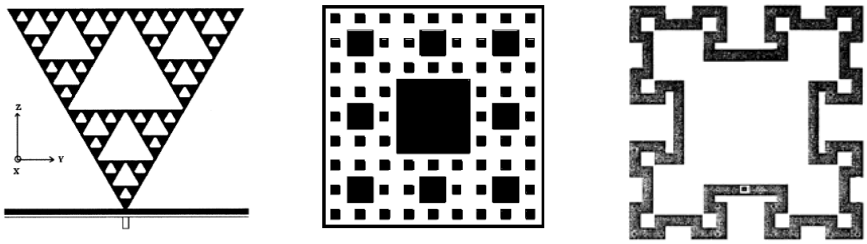

(a) (b) (c)

Figure 1.15: Fractal antenna geometries,(a) Sierpinski triangle antenna [33], (b) Sierpinski carpet antenna [34], (c) Square curve fractal antenna [37].

Several fractal geometries have been employed for the design of multiband antennas including: Sierpinski triangle antenna [33] (Figure 1.15(a)), Sierpinski carpet antenna [34] (Figure 1.15(b)), triangular and circular fractal antenna [35, 36] and square curve fractal antenna [37] (Figure 1.15(c)). The authors of these geometries attribute the property of resonating at multiple frequencies of these structures to their self-similarity. The main advantage of these structures is that are compact structures that can be used for miniaturization but they also suffer from limitation including: The lack of design rules, the control of the resonance frequencies.

1.5.4 Trap-loaded antennas

One of the oldest concepts for achieving multiband wire antennas involves integrating discrete loads (capacitor and/or indicator) into a wire antenna, typically a dipole. These loads are commonly referred to as "traps". The development of this concept occurs in two stages: first, the resonant antenna at the low frequency is designed, then the loads are introduced at specific locations to achieve the desired high resonance. This concept was patented in 1941 [38] and widely used for obtaining multiband antennas [39]. Figure 1.16 shows a dual band antenna based on this concept. The low frequency of this antenna corresponds to the total length of the dipole $2(l_1+l_2)$. The high frequency

corresponds to the length of the dipole limited by the loads $2l_1$. These loads have little effect on the position of the low frequency and on the characteristics of the dipole at this frequency. At the high frequency, these loads cut off the current that no longer flows on the outer lines (of length l_2): these lines do not disturb either the position of the high frequency or the characteristics of the antenna at this frequency. The positions of these loads can be calculated simply in the case of a monopole or straight dipole. Moreover, the use of traps with a high quality factor systematically reduces the bandwidths of the antenna. For this reason, these multiband antenna architectures have often been reserved for low frequency systems.

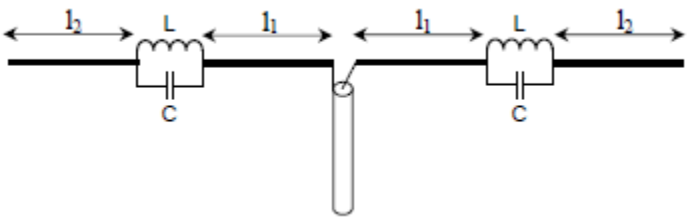

Figure 1.16: Trap-loaded dipole antenna [38].

The motivation for such an approach is very advantage of these trap structures to resonate at multiple frequencies while maintaining the same electromagnetic characteristics. Moreover, the sizing of these antennas is relatively straightforward since each operating frequency is directly linked to the corresponding resonator. To achieve dual band operation, traps have been used in a quadrifilar helix antenna for GPS navigation systems [40], in fractal antennas such as the Sierpinski triangle [41]. Recently, even triple-band operation has been achieved by placing traps on an inverted L-type antenna for GPS applications [42].

1.6 Wideband and multiband antennas for aerospace applications

In aerospace applications, both wideband and multiband antennas play crucial role in enabling reliable communication links, radar systems, navigation,surveillance capabilities for aircraft and other critical functions. The choice between wideband and multiband antennas depends on factors such as the specific frequency bands of interest, system requirements, antenna size and weight constraints, and the desired trade-offs

between bandwidth, efficiency, and performance in each frequency band.
For aerospace communication, different satellite bands can be used [43] :

- L-Band (1-2 GHz) is used on aircacfrt often satellite communications (SATCOM), including cockpit communications, air traffic control, and passenger connectivity.
- C-Band (4-8 GHz) are utilized for SATCOM systems in aircraft, primarily for data communications and broadband internet access.
- Ku-Band (12-18 GHz) is commonly used for in-flight connectivity (IFC) services on aircraft, offering higher data transfer rates compared to L-Band and C-Band systems. Ku-Band satellite systems are extensively deployed for providing broadband internet access to passengers and crew members during flight.
- X-Band (8-12 GHz) is less commonly used in commercial aviation. However, it may be utilized in specific military or government applications for secure communications or specialized data links.

A non-exhaustive list of antennas used in aerospace is presented in this section. Figure 1.17, shows a photograph of the S-band micro strip-patch antenna utilized at Surrey Satellite Technology (SSTL) [44]. This antenna features a circular microstrip patch in size of 82 x 82 x 20 mm, which is fed by a 50 Ω probe feed located at the bottom. It is capable of operating within a tunable frequency range spanning from 2.0 to 2.5 GHz With a maximum gain of approximately 6.5 dB, either left-hand or right-hand circular polarization are employed .

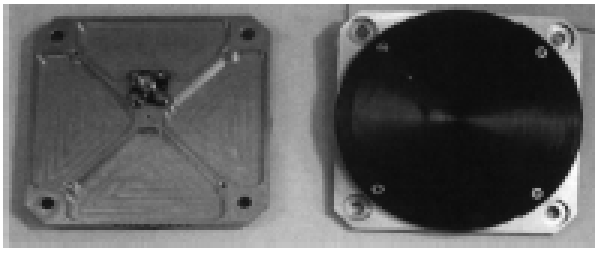

Figure 1.17: S-band antenna used for satellite communication [44].

The GPS antennas used on aircraft typically consist of one or more circular patch antenna elements. These patch antennas are generally limited in their power handling capability, typically around 5 W, and are primarily used as receive antennas. Circular polarization is achieved with these patch antennas by feeding them at a specific point,

allowing for optimal performance in various aerospace applications [45, 46].
Figure 1.18 shows the patch-excited cup antenna developed at Rüstungs Unternehmen Aktiengesellschaft RUAG Aerospace Sweden [45]. It consists of two patches placed in circular cup. To obtain a stable antenna covering two GPS frequency bands (Ll, L2). Moreover, the patch can be employed in RADALT radar altimeter as it is depicted in Figure 1.19. It measures altitude above the terrain presently beneath an aircraft or spacecraft, UAV [47] .

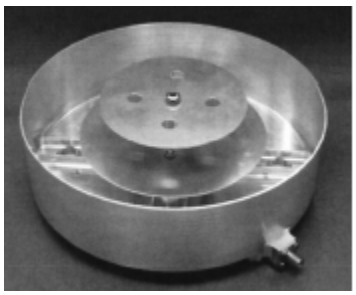

Figure 1.18: GPS circular patch antenna at RUAG Aerospace Sweden [45].

Figure 1.19: Radar altimeter [47].

Furthermore, patch array antenna also can be employed on board an aircraft. It consists of multiple patch elements arranged in an array configuration. This array design allows for increased signal reception compared to single patch antennas, as multiple elements can capture signals from different satellites,simultaneously. This helps improve the overall reception quality and accuracy of the GPS system onboard the aircraft. This is mean that the array of patch antennas creates a narrower beam. In the case of military aircraft, it employs null steering. Null steering involves forming the beam pattern in such a way that there is a null (a region of minimal radiation) in the direction of an unwanted interfering or jamming signal. These specialized antennas are known as Controlled Radiation Pattern Antennas (CRPA). As it is shown in Figure 1.20, a typical CRPA configuration consists of seven-element arrays, with a central patch

surrounded by six elements arranged symmetrically around it. This arrangement allows for precise control over the radiation pattern of the antenna. By adjusting the phase and amplitude of the signals fed to each element, the antenna system can create nulls in specific directions while maintaining high gain in the desired direction [46].

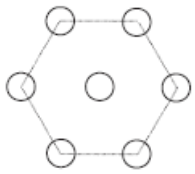

Figure 1.20: GPS CRPA method [45].

Spiral antennas are compact, can cover a broad frequency range, and provide circular polarization. They're useful in various fields, particularly in GNSS applications where right-hand circularly polarized (RHCP) antennas are preferred. Moreover they're also valuable in defense industries for sensing tasks like ESM (Electronic Support Measures). Typically, airborne spiral antennas are typically unidirectional and are often implemented on printed circuit boards (PCBs) backed by a cavity with radiation-absorbing material to absorb back radiation. This design configuration helps to enhance the antenna's directivity and radiation efficiency by minimizing unwanted radiation in directions other than the desired direction of propagation. The cavity behind the PCB serves to prevent reflections and interference, while the radiation-absorbing material helps to absorb any radiation that may be emitted in undesirable directions, thus improving the antenna's performance and effectiveness in airborne applications[46] but present a bulky structure .

1.7 Conclusion

In conclusion, wideband and multiband antennas offer versatile and efficient solutions for a variety of communication and data transmission applications especially for aerospace applications. Their ability to operate over a broad range of frequencies makes them particularly suitable for environments where spectrum availability is limited or fluctuating. Additionally, their design often allows for reduced overall system complexity, providing cost and deployment ease benefits.

Chapter 2

Antenna reflectors based on artificial materials

2.1 Introduction

In the context of electromagnetic compatibility, it's crucial to ensure that different electronic systems and antennas operating in close proximity do not interfere with each other. Therefore, antennas should be designed to minimize interference and maintaining stable performances. Reflectors are common solution which allows the antenna to radiate in only one half-space, focusing its radiation in one specific direction which minimizes interferences with neighboring systems.
The first part of this chapter describes conventional reflectors and their limitations. To mitigate these issues, special types of reflectors based on artificial materials are described, and their main analytical and numerical methods are synthesized in order to reuse or adapt them to our problem. The second part presents an overview of wideband and multiband antennas using artificial materials as reflector.

2.2 Conventional reflectors

The association of radiating element with a reflector leads to interactions between incident and reflected fields. These phenomena can be described by involving the concept of surface impedance and the theory of images, leading to an efficient approach to solving electromagnetic problems involving conductors. It is particularly useful when analyzing the behavior of electromagnetic fields at the interface of different media, such

as when waves encounter a conductive or dielectric surface. In our case, electric and magnetic conductor are considered to better understand the behavior of electromagnetic waves in vicinity of reflectors. They are denoted by the acronyms PEC (Perfect Electric Conductor), PMC (Perfect Magnetic Conductor). Surface impedance is particularly relevant at the boundary or surface of a material. It describes the relationship between the tangential components of the electric and magnetic fields (Equation 2.1). For a plane wave, the reflection coefficient of the electric field is given by Equation 2.2, where η is the impedance of free space.

$$Z_S = \frac{E_T}{H_T} \tag{2.1}$$

$$\Gamma = \frac{Z_S - \eta}{Z_S + \eta} \tag{2.2}$$

Figure 2.1, illustrates the theory of image concept, in this scenario, the original sources of current are positioned at a distance h from the reflecting plane. In order to simplify the analysis of how real currents interact with reflecting surfaces, an image currents are introduced on the other side of the surface, creating an equivalent problem (without reflecting surfaces) that is easier to solve.

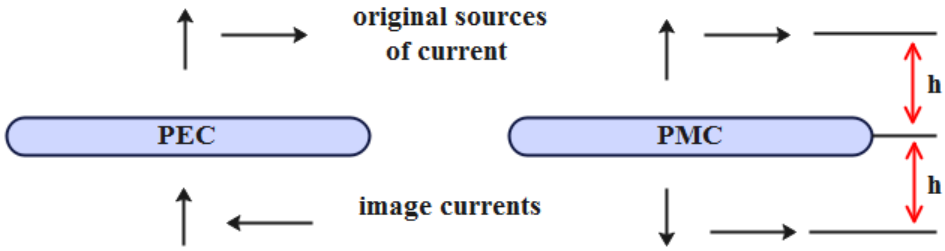

Figure 2.1: Theory of image concept in proximity to PEC and PMC.

2.2.1 Antenna in proximity to an absorbing cavity

An antenna in proximity to an absorbing cavity typically refers to the placement of an antenna close to or near a cavity that is designed to absorb or attenuate electromagnetic waves. It is one of the traditional way that employed to maximize the absorption of the antenna backward radiation and the interferences between front and back radiation.

The radiating element is then placed above a cavity constructed with high dielectric loss or conductive properties. These materials are often carbon-loaded or designed to have a high loss tangent. When electromagnetic waves encounter these materials, they induce currents within the materials, and these induced currents result in energy dissipation in the form of heat. By dissipating the energy in this way, the absorbing materials effectively absorb and attenuate the electromagnetic waves, preventing them from reflecting back towards the antenna or scattering in undesired directions. In the same time this solution suffer from several drawbacks like: large structure, complex design and integration, high cost [48].

2.2.2 Antenna over PEC reflector

The second solution aims to redirect a portion of the radiation in the opposite direction and block or reduce the transmission of electromagnetic waves on the other side of the ground plane using a PEC reflector. Figure 2.2, illustrates the behavior of radiating element when it is placed in proximity of PEC reflector. Despite the advantages of the PEC ground plane, it has a significant drawback, which is the cancellation of the antenna's current with the image current produced by the PEC ground plane. This cancellation deteriorates the antenna's impedance matching and its radiation. One way to avoid this phase shift of π between the original current and its image is to space the antenna from its metal reflector at a height equal to $\lambda/4$ as it is illustrated in Figure 2.2. In this way, two in-phase waves can be obtained; therefore, the antenna performances could be enhanced. The main drawback of this method is that it would results in large structures, especially at low frequency [48].

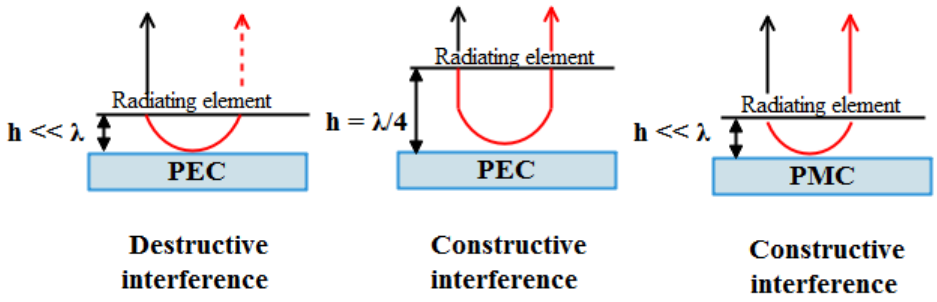

Figure 2.2: Antenna over PEC and PMC reflector.

2.2.3 Antenna over PMC reflector

In contrast to PEC, PMC generates an image current in phase with the real current when a horizontal antenna is placed above it therefore the reflected wave will be in phase with the incident wave, generating a constructive interference. Consequently, the optimal quarter-wavelength distance is no longer necessary and the antenna can be placed very close to the reflector plane, significantly reducing the overall thickness of the antenna structure. Unlike metals, the PMC don't naturally exist. However, recent studies have shown that it is possible to synthesize, within a restricted frequency band, these characteristics[48].

2.3 Artificial materials-based reflectors

In recent years, there has been a growing interest in so-called "artificial" materials". They are the result of continued research initiated on periodic structures [49] and exhibit remarkable properties. By the end of 1990s, Pendry introduced two structures with novel characteristics. The first, composed of a network of metallic wires, exhibits a negative permittivity [50]. The second, made up of split-ring resonators, demonstrates negative permeability [51] . In the early 2000s, Smith, combined the two aforementioned structures and experimentally verified the concept of a material with negative index [52], whose theoretical existence had been suggested by Veselago in 1964 [53]. These studies paved the way for new devices such as "perfect lenses" [54] and "invisibility cloaks" for stealth applications [55]. These materials are collectively referred to as "metamaterials" due to their innovative nature. This relatively recent field of research, spanning multiple disciplines of electromagnetism, is divided into several sub classes of materials, each with its own acronym. This section is dedicated to presenting artificial materials used as reflector planes for antennas.

2.3.1 Artificial Magnetic Conductor

Recent research has demonstrated the possibility of synthesizing PMC property within a specific frequency range. These materials are denoted by the acronyms AMC (Artificial Magnetic conductor). It is an artificial material created by periodic metallic arrangements printed on a metal-backed substrate without shorting pins (via). The AMC surfaces is characterized by distinctive property which the in-phase reflection properties [56]. This property allows the AMC to reflect the incident wave with zero

degree in its resonant frequency. It is represented graphically by phase diagram [57], as shown in Figure 2.3. The phase diagram characterizes the phase difference between the incident and reflected electric fields at the surface of this reflector. The reflection phase generated by this surface is given by equation (2.3):

$$\Phi = Im\left[\ln\left(\frac{Z_S - \eta}{Z_S + \eta}\right)\right] \tag{2.3}$$

Where:

- Z_S is the surface impedance (Equation 2.5).
- $\eta = \sqrt{\epsilon_0/\mu_0}$ is the impedance of free space.

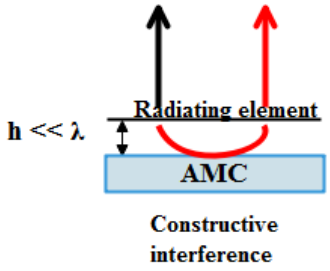

Figure 2.3: Radiating element placed over the AMC reflector.

The AMC surface behaves as a PEC at low frequencies ($\phi = \pi$), then as PMC at a frequency where $\phi = 0$, and to a PEC at high frequencies (ϕ = -π). This transition is illustrated in the phase diagram [56] (see Figure 2.4). Within a specific frequency range, the structure demonstrates nearly zero phase shift, ranging from –90° (F_l) to +90° (F_h), and known as the AMC in-phase bandwidth. Within this bandwidth, the AMC surface effectively produces reflected waves aligned in the same direction as the original incident wave, as depicted in Figure 2.3. Consequently, these reflected waves constructively interfere with the source wave, increasing the antenna's radiation efficiency and gain [57].

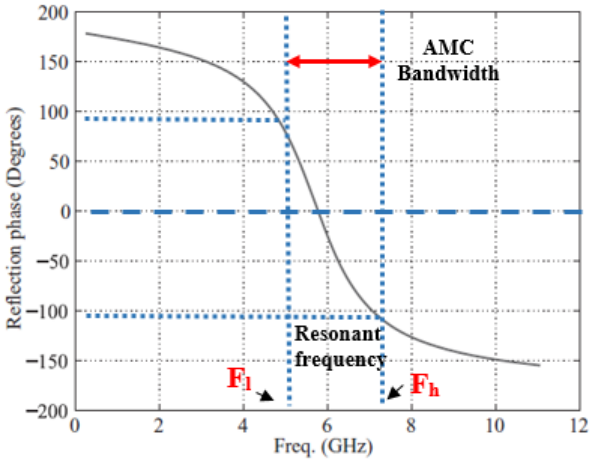

Figure 2.4: Typical reflection phase diagram of AMC [57].

2.3.2 Electromagnetic Band Gap (EBG)

Electromagnetic Band Gap (EBG) structures are commonly formed through the systematic placement of dielectric materials and metallic conductors in a periodic manner. Broadly, these structures can be classified into three categories based on their geometric arrangements: three-dimensional volumetric structures, two-dimensional planar surfaces, and one-dimensional structures, as illustrated in Figure 2.5. These structures show a fascinating characteristics, particularly the presence of band gap feature. This indicates their capability to impede the propagation of specific frequency bands of electromagnetic waves (surface wave propagation). Its concept arise from the optical domain where phonetic band gap (PBG) can forbid light in specific directions. In 1980 Yablonovitch [58], has manufactured the first periodic structure by cylindrical holes drilled in dielectric material which prove the existence of the band gap structure. Later in 1990, Sievnipiper [56] realized the first 2D planer EBG mushroom.

The frequency band gap property of the EBG structures is determined by graphical representation called dispersion diagram. The plot of this dispersion diagram determines the set of modes that the structure can support. It represents the evolution of the wave vector k as a function of frequency in a given propagation direction. To calculate the dispersion diagram of the EBG structure, the Brillouin zone is used in order to simplify the calculation. When the EBG structures elements are periodic arranged in a square lattice, then the Brillouin zone is square.

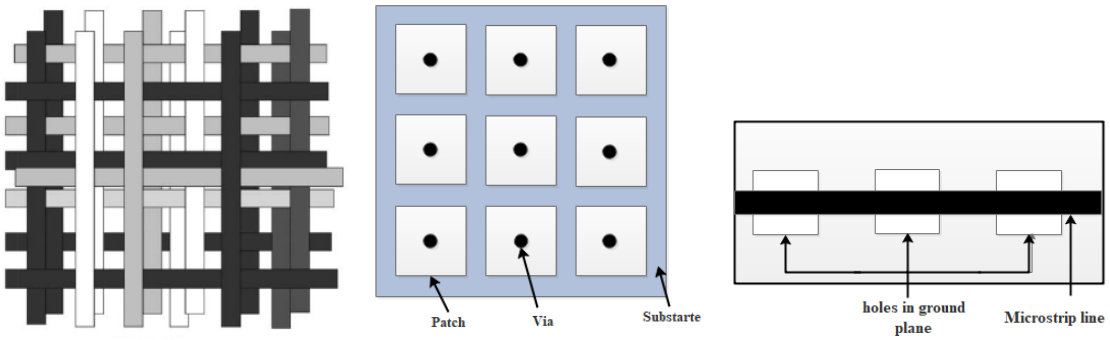

(a) (b) (c)

Figure 2.5: Dimensionality of EBG structures [57], (a) 3D-EBG, (b) 2D-EBG, (c) 1D-EBG.

Figure 2.6 presents an illustrative example of a numerically computed dispersion diagram [56]. It is evident from the diagram that the stop band region lies between the TM and TE modes. This signifies that within this frequency range, no surface waves can propagate in the EBG structure, indicating the presence of a band gap.

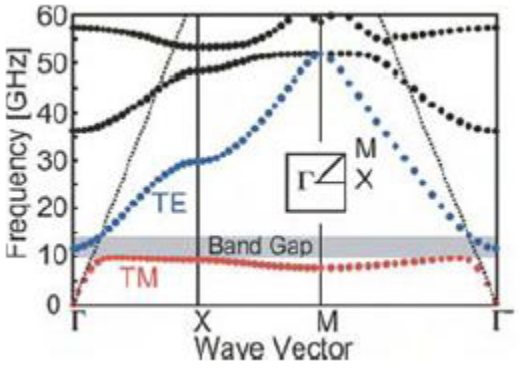

Figure 2.6: Illustration of band gap feature [56].

2.3.3 Sievnipiper EBG mushroom.

An EBG mushroom is artificial material comprises metal patches arranged on the surface of a substrate in a two-dimensional lattice, with each patch separated by a gap. Additionally, each patch is linked to the ground through vias. This structure is introduced by Sievnipiper in 1990 [56], as it is illustrated in Figure 2.7. It is an illustration of a structure exhibiting both AMC and EBG characteristics.

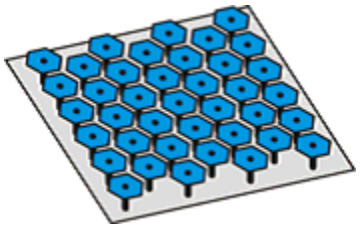

Figure 2.7: EBG mushroom [56].

The AMC behavior (in-phase reflection) arises from the periodic arrangement of metallic patches while the EBG behavior or the band gap feature is linked to the presence of vias, which are equivalent to a network of metallic wires within the dielectric [56]. In the case where the structure does not contain vias, a dielectric overlaying a metallic plane, the wave has a cutoff frequency given by expression (2.4). The TM mode corresponds to even values of n, while the TE mode corresponds to odd values of n. The TM_0 mode has a cutoff frequency of zero and always propagates.

$$f_c = \frac{nc}{4h\sqrt{\epsilon_r - 1}} \tag{2.4}$$

Where:

- c is the Speed of Light
- h and ϵ_r are thickness and relative permittivity of the substrate.

If the structure contains vias, current flows through the via, creating an electrical connection with the ground plane. The structure through which the wave propagates is likened to an equivalent parallel LC circuit with surface impedance given by Equation (2.5):

$$Z_S = \frac{j\omega L}{1 - LC\omega^2} \tag{2.5}$$

When the frequency f is lower than the resonant frequency f_0, Z_S is inductive and only the TM mode can propagate. Conversely, if f is higher than f_0, Z_S is capacitive and only the TE mode propagates. There exists a band, around f_0, in which wave propagation is prohibited which is define as the band gap feature, as shown in Figure 2.6.

2.4 Circuit models

2.4.1 Analytical model

The analytical approach allows for a more straightforward resolution of a problem by simplifying equations. This involves making certain assumptions that lead to favoring certain data over others. Analytical modeling also allows for a better understanding of the underlying physical phenomena and a relatively quick prediction of the overall behavior of a system. In the literature, most analytical models are based on the theory of effective media [56]. This theory enables the description of physical mechanisms using localized elements. For this, it is necessary to consider that the dimensions of the structure are small compared to the wavelength.

a Lumped element model

The lumped element model is the most basic representation, characterizes metasurface as an LC resonant circuit. The operational mechanism of metasuarface structures can be described by employing an effective medium model that employs equivalent lumped LC components [59], illustrated in Figure 2.8. The capacitor is a consequence of the gap between the patches, while the inductor arises from the current flowing along adjacent patches. The impedance of a parallel resonant LC circuit is determined by Equation 2.5, while the resonances frequency is calculated by Equation 2.6:

$$\omega_0 = \frac{1}{\sqrt{LC}} \tag{2.6}$$

The specific values of inductor (L) and capacitor (C) are determined by the metasuarface geometry as depicted in Figure 2.9, where, patch width W, gap width g, substrate thickness h, dielectric constant ϵ_r, and vias radius r.
The derivation of the capacitor can be given by the fringing capacitance between the two neighboring metal patches (gap). Ultimately, it is provided by the following Equation 2.7:

$$C = W\epsilon_0(1+\epsilon_r)\cosh^{-}1\left(\frac{W+g}{g}\right) \tag{2.7}$$

The value of the inductor is derived from the current loop consisting of the vias and metal sheets. It is expressed by Equation 2.8, it mainly relies on the structure's thickness and permeability.

$$L = \mu.h \tag{2.8}$$

By substituting Equation (2.7) and (2.8) into (2.5) and (2.6), one can calculate the surface impedance and resonant frequency. The main drawback of this model is that the result are not accuracy due to the simplified estimation of L and C.

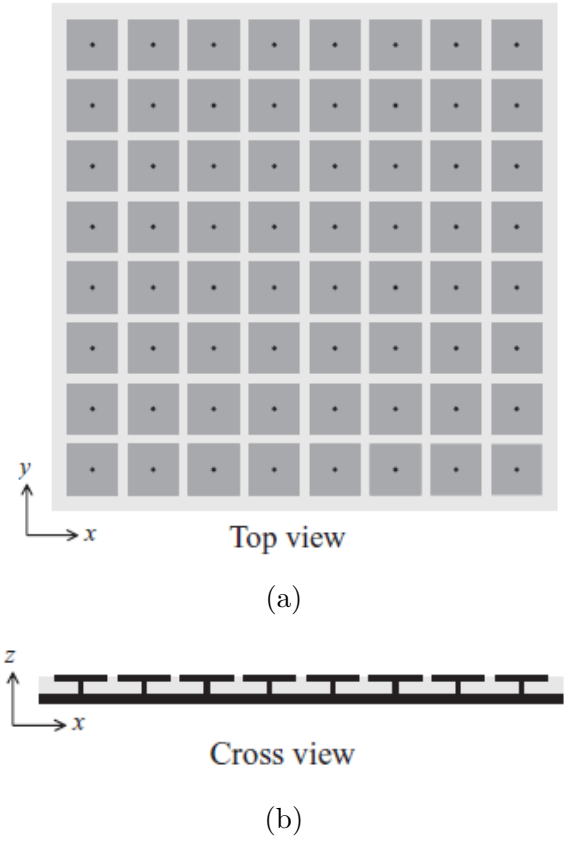

Figure 2.8: Geometry of mushroom structure , (a) Top view, (b) Cross view [59].

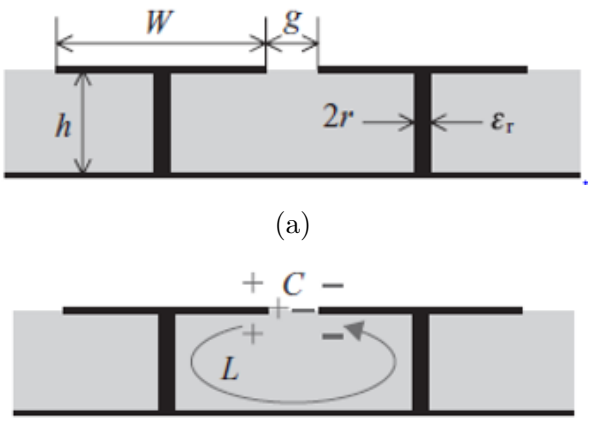

Figure 2.9: Lumped element models of EBG structure, (a) EBG cell geometry, (b) *LC* model [59].

b Transmission line model

Another widely used technique for analyzing metasurafce structures is the periodic transmission line method [60]. The transmission line model of metasurafce structures is presented, with Z_P representing the impedance for each periodic element, and X_C denoting the coupling capacitor as depicted in Figure 2.10.

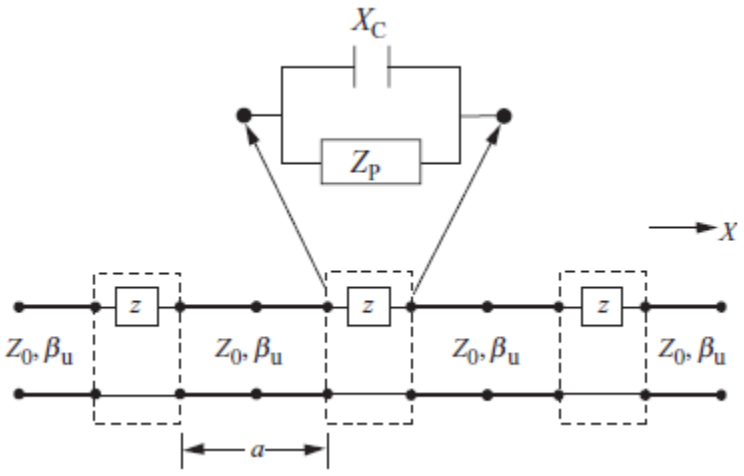

Figure 2.10: Transmission line model [59].

The impedance Z_P of each element is determined using the well-known transmission line formula (Equation 2.9):

$$Z_P = Z_0 \frac{Z_1 + jZ_0 \tan(\beta_u)}{Z_0 + jZ_1 \tan(\beta_u)} \tag{2.9}$$

Where, Z_0 represents the characteristic impedance, and β_u stands for the phase constant of the transmission line. The coupling capacitor X_C between the elements is also calculated using Equation 2.7. Once the impedance of the resonator (Z_P) and the coupling capacitor (X_C) are determined, the structure can be regarded as a transmission line periodically loaded with a lumped impedance Z. The value of Z is derived from the parallel connection of Z_P and X_C.

2.4.2 Numerical methods

Numerical modeling generally allows for more precise results than analytical modeling. Indeed, electromagnetic simulation methods take into account the interactions of waves with the metal-dielectric medium, leakage modes, and periodicity. However, they can result in quite long calculation times depending on the type of simulation . The objective of this paragraph is to briefly present the numerical methods involved in this thesis. In the design phase, the use of electromagnetic simulators is crucial for reducing costs associated with prototyping and measurements. The simulation results presented in this thesis were obtained using CST Microwave Studio (CST MWS).
CST Microwave Studio uses the Finite Integration Technique (FIT), introduced by Weiland in 1977 [61]. It is one of the temporal methods generally well-suited for wideband problems. It involves a spatial-temporal discretization of Maxwell's equations in an integral formulation. The computational domain is decomposed into cubic elemental cells. The FIT is a generalization of the Finite-Difference Time-Domain method (FDTD) [62], one of the most useful numerical methods used to simulate the behavior of electromagnetic fields. It straightforwardly discretizes Maxwell's equations in both time and space domains. The method was first proposed in a seminal 1966 paper by Kane Yee. The FDTD acronym, in turn, was coined later by Taflove in the 1980s [62, 63]. The resolution of the equations is done in a cartesian discretization, which can characterize up to two distinct materials in the same grid cell, offering a considerable advantage over FDTD methods. This allows for a reduction in the overall number of cells required for equivalent precision.

a Reflection phase diagram:

The metasurfaces provide a significant reflection phase response when it react like AMC. Equation 2.3, represents the reflection phase generated by the High Impedance Surface (Φ) when an incident wave is directed perpendicular to its surface. As the surface impedance (Z_S) tends towards infinity (Equation 2.5), the reflection phase of the surface approaches zero. At this condition the metasurface structure, react like AMC surfaces (no shorting pin) [56]. The reflection coefficient can be calculated using CST simulation software with periodic boundary conditions (see Figure 2.11).
This involves positioning a single unit cell within a radiating box with PEC and PMC walls. The unit cell is then exposed to a normally incident wave for analysis [57]. The AMC show its unique characteristic within a limited bandwidth (the in-phase bandwidth) ranging from - 90° (lower frequency) to +90° (higher frequency), as it is shown in Figure.2.12. It is required to resonate at the center frequency where the reflection phase is zero-degree.

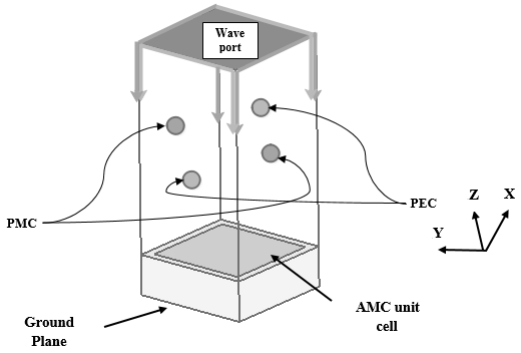

Figure 2.11: The applied boundary condition around AMC unit cell.

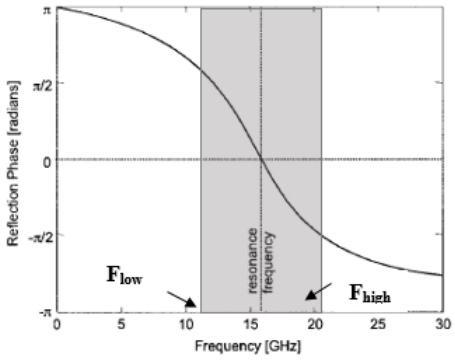

Figure 2.12: Reflection phase responses [56].

b Dispersion diagram

Dispersion diagrams is graphical representation that illustrates how the wavenumber (usually denoted as "k") of waves varies with frequency within a specific guiding structure. The wavenumber (k) represents the spatial frequency of waves in a given medium or structure, how many wave cycles occur per unit length. It is defined as: (Equation 2.10):

$$k = \frac{2\pi}{\lambda} \tag{2.10}$$

Where:

- k is the wavenumber.
- λ is the wavelength of the wave.

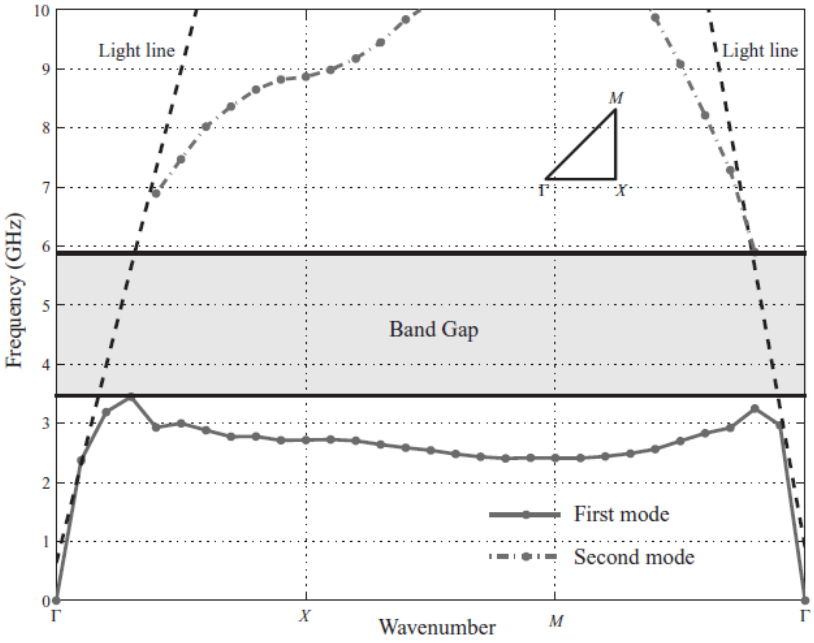

Figure 2.13: FDTD simulated dispersion diagram of the mushroom-like EBG structure [57].

The wave number in EBG structures is usually difficult to express explicitly and has to be obtained by solving the eigenvalue equation [57]. Eigenmode solvers in CST Microwave Studio are used to calculate the eigenfrequencies and corresponding field distributions of the EBG structure. By analyzing the eigenmodes, the dispersion diagram can be constructed to identify the bandgaps and propagation characteristics.

Since EBG structures are periodic, simulating them using traditional FDTD models can be computationally intensive and require extensive memory storage. However, by employing Periodic Boundary Conditions (PBCs), only a single cell of the EBG structure needs to be computed in the FDTD simulations. PBCs are applied on all four sides of the cell to model an infinite periodic replication. This approach offers several benefits: it significantly reduces the computational cost as only one unit cell is simulated; optimizes memory usage and reduce the simulation time [57].
In particular, several information can be extracted from the dispersion diagram (see Figure 2.13) for EBG mushroom structure proved in [56, 57]:

- The highlighted electromagnetic band gap (EBG) area, marked in grey, exists at a frequency range situated below the first-order TE (Transverse Electric) surface mode and above the first-order TM (Transverse Magnetic) mode.
- At lower frequencies, the surface impedance exhibits inductive characteristics, leading to the support of a fundamental TM (Transverse Magnetic) mode.
- At higher frequencies, the surface impedance exhibits capacitive characteristics, leading to the support of a fundamental TE (Transverse electric) mode.

2.5 State-of-the-art of wideband and multiband antennas based on artificial material reflectors

2.5.1 AMC reflectors-based wideband antennas

Various approaches have been proposed to enhance the performances of wideband antenna. Some research results on wideband dipoles backed by AMC reflectors have been reported, a simple dipole with EBG reflector is presented in [64]. However, the directional wideband dipole antenna backed by EBG structure shows 37% of a relative bandwidth and a low profile height of only $0.038\lambda_0$. A printed bowtie antenna backed by fractal wideband AMC reflector is investigated in [65], for gain enhancement. As shown in Figure 2.14. The AMC is consisted of 6×9 fractal shaped unit cells made of multiple big and small circles with $\pm$ 90° reflection phase band of 1.1–3.03 GHz. The radiating configuration shows 16.7% of a relative bandwidth with a gain enhancement of 4 dB and a gain variation of 2 dB.

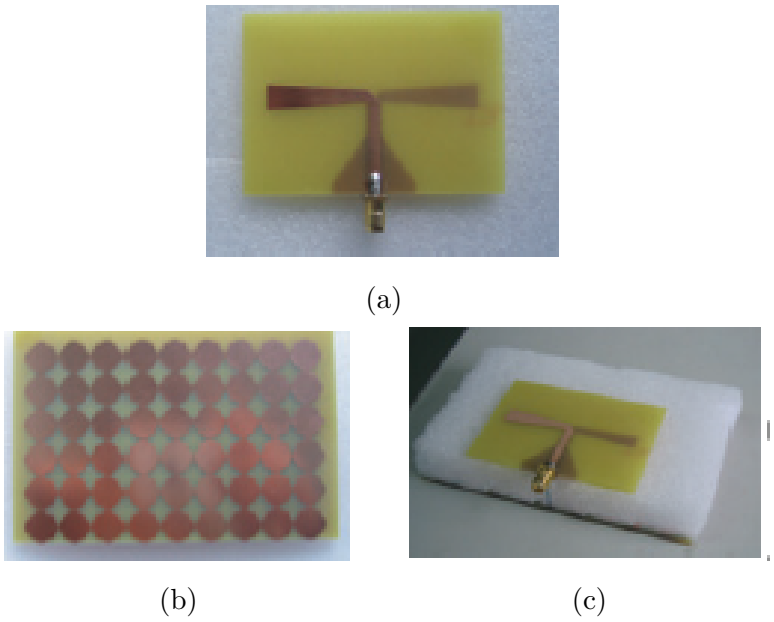

(a)

(b) (c)

Figure 2.14: Bowtie antenna loaded with fractal shaped AMC reflector for gain enhancement [65], (a) Top antenna view, (b) Top AMC view, (c) The overall antenna structure.

Moreover, a wideband dual polarized antenna loaded with wideband AMC reflector is described in [66]. It is composed of four printed dipoles used as radiating elements to obtain both vertical and horizontal polarization as seen in Figure 2.15(a). The results indicate that the proposed design can reach 40% of impedance bandwidth with a gain variation of 2 dB and a low profile of 0.085 λ_0. Furthermore, a coplanar waveguide fed antenna with an AMC is investigated in [67] (see Figure.2.15(b)) to achieve directional radiation patterns with a gain variation of 2.85 dB over 36.7% of relative impedance bandwidth. Besides, authors in [68, 69, 70] have reported that size, number and arrangement of unit cells affect the antenna performances and showed that it exists a certain configurations of AMC, for which optimal directive gain is obtained.
In [71], it has been demonstrated that the radiation pattern degradation is mainly caused by the presence of destructive surface waves in the AMC reflector. A hybrid AMC reflector composed of both PEC/AMC was then proposed to eliminate the main lobe-splitting drawback of planar diamond antenna,as presented in Figure 2.16 (a). However, a wide impedance bandwidth of 46% (4.2 - 8.1 GHz) with a stable gain of fluctuation of 3 dB can be obtained by using the hybrid AMC rather than the uniformed AMC reflector.

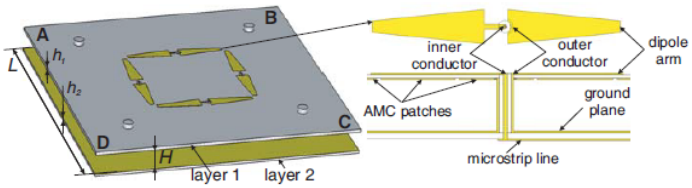

(a)

(b)

Figure 2.15: Wideband antennas over AMC reflectors in: (a) [66], (b) [67].

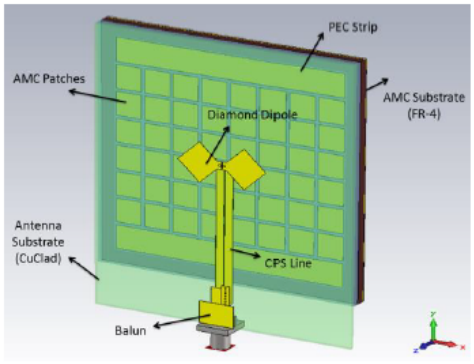

(a)

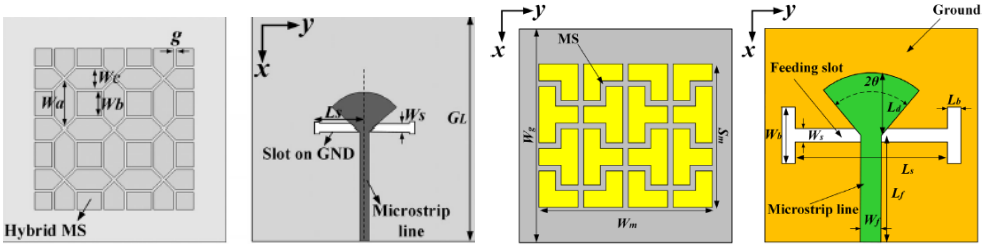

(b) (c)

Figure 2.16: Wideband antennas loaded withh various AMC reflectors in: (a) [71], (b) [72], (c) [73].

Similar approaches has been developed in [72, 73] where a wideband antenna-based hybrid AMC reflector is investigated for gain enhancements. The two AMC arrays are depicted in Figure 2.16(b) and Figure 2.16(c). It is reported that two antenna structures show a wide impedance bandwidth of 39%, 44% with a stable gain of 2 dB gain variation, respectively. In [74], an AMC reflector with six metallic walls are used to stabilize the radiation pattern of dipole antenna, as it is illustrated in Figure 2.17. The antenna consists of a pair of crossed-dipoles loaded on a wideband hybrid AMC reflector. The results indicate that the proposed configuration could achieve a stable gain variation of 0.85 dB while maintaining a reduced thickness (reduced from 36 mm to 18 mm) by using the AMC reflector.

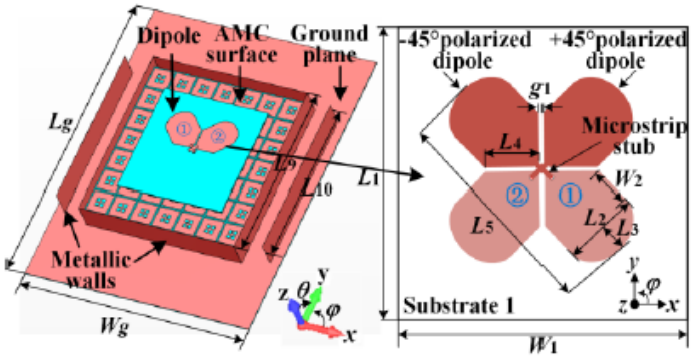

Figure 2.17: Crossed-dipole backed with wideband hybrid AMC reflector [74].

Another approach has been proposed in [75, 76] (see Figure 2.18). A non-periodic AMC reflector is suggested to mitigate the main beam splitting in the broadside direction of a dual dipole antenna. 3 dB gain bandwidth can be achieved for both structure compared to the uniform AMC reflector.

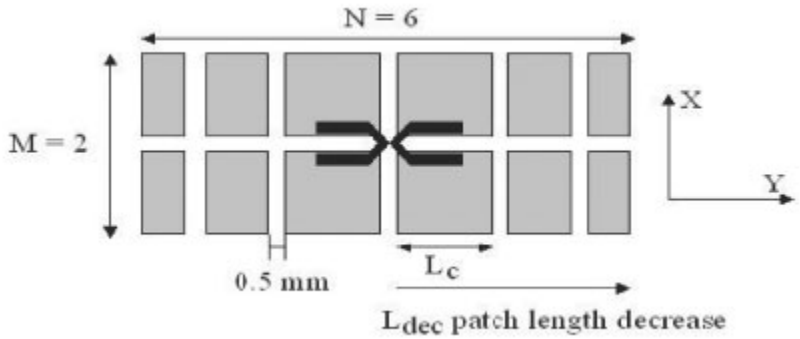

Figure 2.18: Dual dipole antenna over the non-periodic AMC reflector [76].

In [77], a wideband low profile CPW fed monopole antenna is investigated using wideband fractal AMC reflector. The AMC reflector of size 30 mm ×30 mm is placed at a distance of 2 mm (see Figure 2.19) to the CPW fed monopole antenna in order to achieve wideband characteristics. It is reported that, by adopting the fractal geometries, the AMC in-phase bandwidth is extended to 5.1–7.4 GHz (36.5%). After the inclusion of the AMC reflector a wide impedance bandwidth could be achieved 4.7-8 GHz (52%) with a unidirectional gain of enhancement of 4 dB compared to the original structure without AMC reflector.

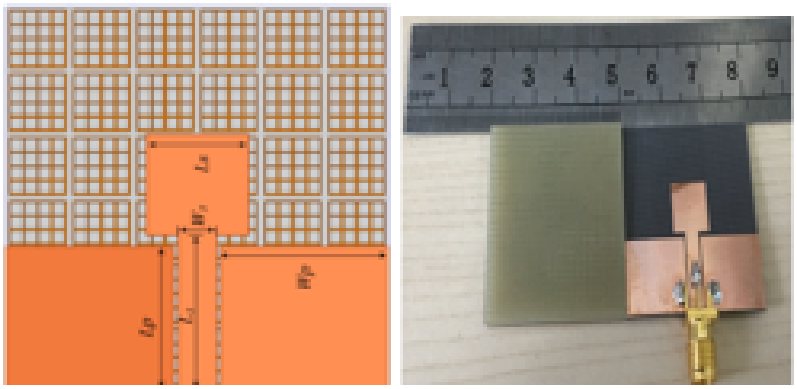

Figure 2.19: CPW fed monopole antenna over the wideband fractal AMC reflector [77].

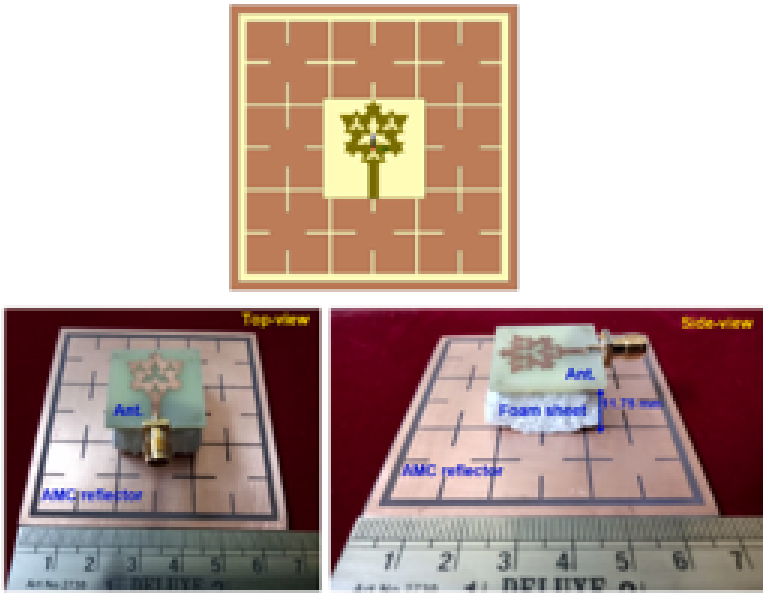

Figure 2.20: Hybrid fractal monopole antenna loaded with wideband AMC reflector [78].

A hybrid fractal monopole antenna loaded with a wideband AMC is investigated in [78] for hybrid wireless cellular networks. The main intuition of this work is to improve the wideband performances with reduced size. A compact AMC reflector of 3×3 AMC unit cells is loaded at 11.75 mm from the antenna structure, as depicted in Figure 2.20. The proposed radiating configuration could exhibit a wide relative impedance bandwidth of 61.68% (3.7–7.0 GHz) with a high gain value between 8 and 13.8 dB. In [79], a broadband low profile circular polarized antenna (cross dipole) baked with AMC reflector is investigated to achieve broadband characteristics (see Figure 2.21(a)). The antenna has a low profile of 0.12 λ_0 at the center frequency of 1.78 GHz. The results indicate that the suggested design show a wide impedance bandwidth ranging from 1.19 to 2.37 GHz which corresponding to a relative bandwidth of (66.3%), with an enhanced gain of 6 dB. As depicted in Figure 2.21(b), a low profile wideband slot antenna loaded with a wideband AMC reflector of size 40 mm ×50 mm, situated at a distance of 5 mm is investigated in [80]. It has a wide impedance bandwidth of 5.06 - 7.92 GHz (44.07%) with a peak gain of almost 8 dB. In [81] an EBG reflector is loaded behind a wideband dual polarized antenna for gain enhancement (see Figure 2.22). The average broadside gain is enhanced to 8.03 dB on a relative impedance bandwidth of 43%.

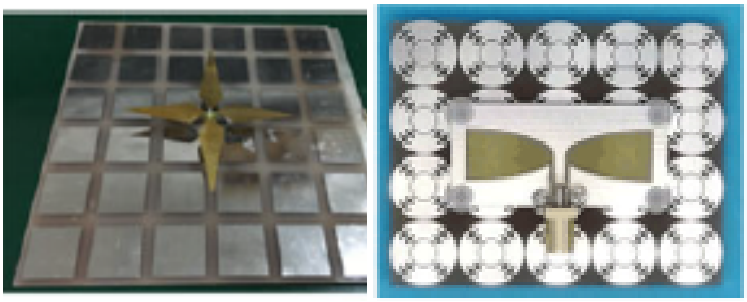

(a) (b)

Figure 2.21: Wideband antennas over AMC reflector designs in: (a) [79], (b) [80].

A low profile printed slot antenna backed by an AMC reflector is proposed in [82] for bandwidth enhancement. Firstly, the antenna is introduced without AMC surfaces then a broadband AMC surfaces is introduced behind the antenna as reflector. The proposed configuration is depicted in Figure 2.25. The printed slot antenna over the AMC reflector exhibits a wide impedance bandwidth of almost 70% ranging from 6.63 to 13.70 GHz then whose without AMC reflector of 20% (9-10 GHz).

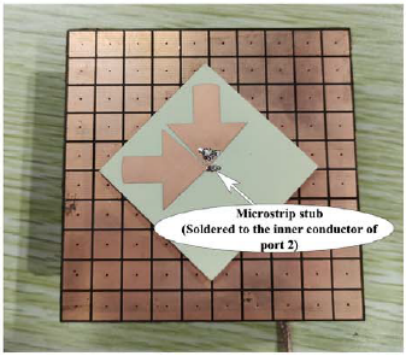

Figure 2.22: Dual polarized antenna based on wideband AMC reflector [81].

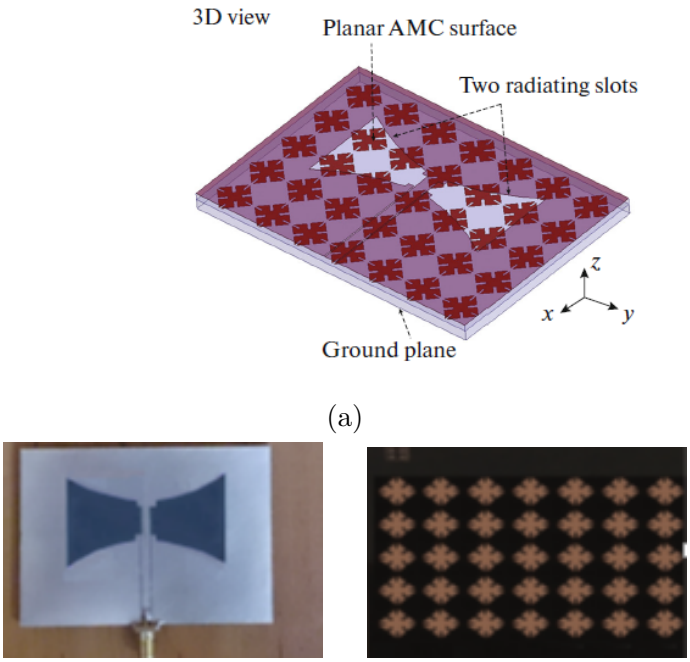

Figure 2.23: Low profile printed slot antenna backed by AMC reflector [82]: (a) The overall structure, (b) Top antenna, (c) Top AMC.

Inserting EBG/AMC cells around the antenna structure can also be explored for gain enhancement. In [83, 84] an metasuface structure is used to boost the gain of a microstrip patch antenna using different configuration: by loading the metasuface structure below and around the microstrip patch antenna (see Figure 2.24). The gain is enhanced to 5.67 and 10.32 dB for the two configurations, respectively, this enhancement resulting from the surface wave suppressing.

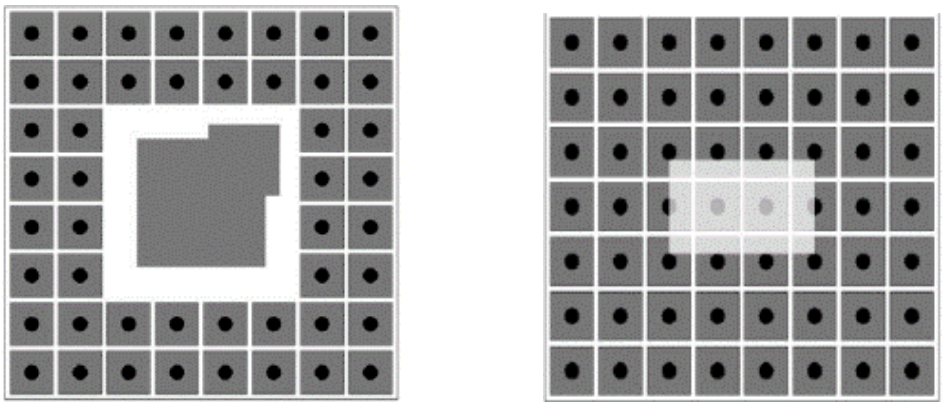

(a) (b)

Figure 2.24: Patch antenna with metasurfces structure: (a) Metasurface around the patch [83], (b) Metasurface below the patch [84].

The main performances of the previous researches works presented in the state of the art are listed in Table 2.1.

Table 2.1: Wideband antennas based on artificial materials

Ref	Overall size dimension(λ_0) (width × length × height)	Frequency band(GHz)	Bandwidth (%)	Max gain(dB)
[64]	0.66 λ_0×0.66 λ_0×0.0386 λ_0	1.7-2.5	38	8
[65]	0.11 λ_0×0.47 λ_0×0.15 λ_0	1.64-1.94	16.7	6.5
[66]	0.1075 λ_0×0.1075 λ_0×0.085 λ_0	1.6-2.4	40	12
[67]	0.86 λ_0 ×0.57 λ_0×0.061 λ_0	5.01–7.35	36.7	6.5
[71]	1.22 λ_0 ×1.22 λ_0×0.11λ_0	4.2–6.7	63	7.9
[72]	1.1 λ_0 × 1.1 λ_0×0.09 λ_0	5.78-8.6	39.2	6
[73]	0.48 λ_0 ×0.48 λ_0×0.10 λ_0	5.93-9.28	44	6
[74]	0.79 λ_0×0.79 λ_0×0.10 λ_0	1.67-2.98	56	8.5
[76]	0.6 λ_0×0.6 λ_0×0.12 λ_0	4.7-8	52	8.5
[77]	0.8 λ_0 ×0.8 λ_0×0.26 λ_0	3.7–7	61.68	8.5
[78]	1.49 λ_0 ×1.49 λ_0×0.12 λ_0	1.19–2.37	66.3	8.5
[80]	0.68 λ_0×1.08 λ_0×0.12 λ_0	5.06-7.92	44	8.5

λ_0 : is the wavelength at the center frequency.

It can be noted that, despite the narrow bandwidth of AMC surfaces, several researchers have successfully achieved wideband performance. However, it can also be observed that, despite the implementation of AMC reflectors, some studies have not succeeded in enhancing antenna bandwidth or achieving a compact size with stable gain across their wide bandwidth. The AMC has still demonstrated its effectiveness not only in wideband antennas but also in multiband antennas, enhancing antenna performance across multiple operating bands simultaneously. This will be briefly discussed next.

2.5.2 AMC reflectors-based multiband antennas

Contrarily to the conventional single wideband band AMC with one zero-phase in the reflection coefficient, multiband AMC can provide two or more zeros-phase, thereby multiple operation bands can be achieved. A metamaterials inspired antenna for airborne application is investigated in [85] (see Figure 2.25). The antenna design is based on the approaches of CRLH-TL (Composite right-left handed material). The antenna geometry provide an LC circuit derived from the rectangular patch, the semicircular patch and the gap inserted between them. By the inclusion on AMC reflector, a unidirectional enhanced gain can be achieved of 6.46 and 7.12 dB centred at 3.27 and 5.11 GHz over an extended bandwidth of 12.23% and 21.96%.

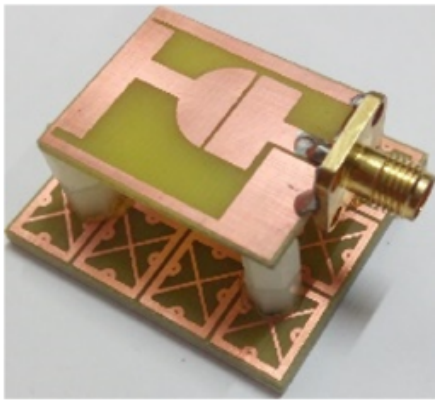

Figure 2.25: Metamaterials inspired antenna loaded with dual band AMC reflector [85].

In [86], a low profile dual band dual polarized antenna array over an AMC reflector is presented for gain enhancement (see Figure 2.26(a)). The proposed combination exhibits a high peak gain values of 10 and 13 dB over an impedance bandwidth of 13.8% (2.44–2.80 GHz) and 6% (4.75–5.03 GHz),covering the sub-6 GHz applications respectively,

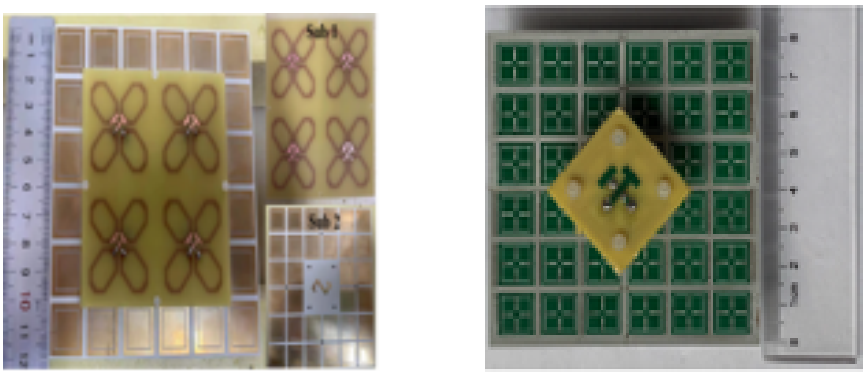

(a) (b)

Figure 2.26: Dual band antennas loaded with the designed AMC reflectors in: (a) [86], (b) [87].

In [87], a dual–wideband antenna circularly polarized antenna loaded AMC reflector is developed as shown in Figure 2.26(b). The proposed antenna exhibits a compact size of 0.64 λ_L × 0.64 λ_L × 0.16 λ_L at 2.4 GHz with two broadband bandwidth of 40% (2–3 GHz) and 49.5% (3.8–6.3 GHz) with an average gain of 6.6,7.4 dB for the lower and upper bands, respectively. Moreover, in [88], a dual band coplanar patch antenna operates at 2.45 and 5.1–5.8 GHz, loaded with metasurface reflector is developed for wearable application. The uni-planar metasurface ground plane ofof 3×3 of slotted square ring patch, as illustrated in Figure 2.27(a). The simulated and measured results show that the gain of the proposed radiating design could enhanced by 3 dB over the two working band of 3%, 25% relative impedance bandwidth centred at 2.45, 5.7 GHz, respectively.

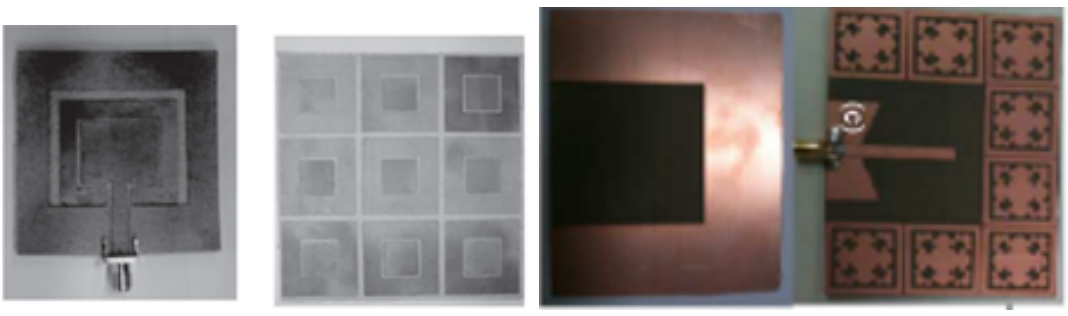

(a) (b)

Figure 2.27: Dual band antennas loaded with the designed AMC reflectors in: (a) [88], (b) [89].

Further, a low profile uni-planar dual band trapezoidal CPW-fed monopole antenna combined with metasurface ground is investigated in [89] for bandwidth enhancement(see Figure 2.27(b)). The radiating structure has low profile of $0.04\lambda_L$ at 2.45 GHz with a peak gain of 2, 5.54 dB over a bandwidth of 391, 578 MHz which corresponding to 9.61% and 17, 67%, respectively. In [90], a dual band microstrip antenna loaded with 6×6 modified SRR (Split Ring Resonator) unit cells is proposed for 2.4 GHz WLAN and 8.2 GHz ITU band applications. The microstrip antenna exhibits two resonances frequency generated by the ground plane and the three U-shaped strips. As shown in Figure 2.28, a modified SRR structure is loaded as AMC reflector to enhance the antenna performances (gain and bandwidth). The two operating bands are upgraded by 16% and 6%, respectively. In addition, the gain is increased by 3.63 dB and 1 dB at 2.36, 8.45 GHz, respectively.

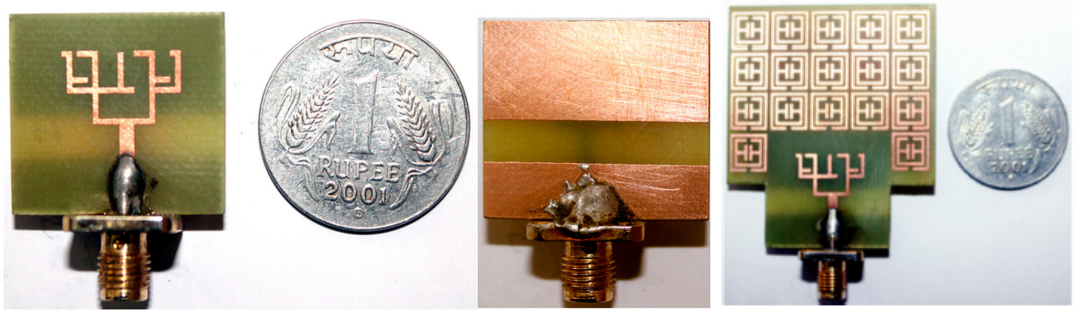

(a) (b)

Figure 2.28: The dual band microstrip antenna over the triple band SRR AMC reflector [90]: (a) Top and bottom view antenna, (b) The overall combined structure (antenna+AMC).

The AMC still proving its efficiency in the gain enhancement, and the backward radiation reduction in diverse applications. Hence, it is a great challenge to enhance the gain across multiple operating bands, simultaneously. As illustrated in Figure 2.29(a), a quad band wearable antennas based on triband AMC reflector with three zeros-in the reflection phase is proposed for gain enhancement and SAR reduction in [91]. The gain can reach more than 5 dB across the four working band (3.5, 5.8, 7.5 and 8.08 GHz), with a reduced SAR of 0.50 after employing the AMC surface. The same approach is utilized in [92], where a triple band wearable antenna loaded with triband AMC reflector is investigated (see Figure 2.29(b)). The antenna has lightweight and low profile of 0.048 λ_L at 2.4 GHz with high gain values of 4.8, 5.1, and 6.2 dB across the triple band

ISM (2.28–2.51)GHz, (5.2–6 GHz) and at WiMAX band (3.5-4GHz),respectively,

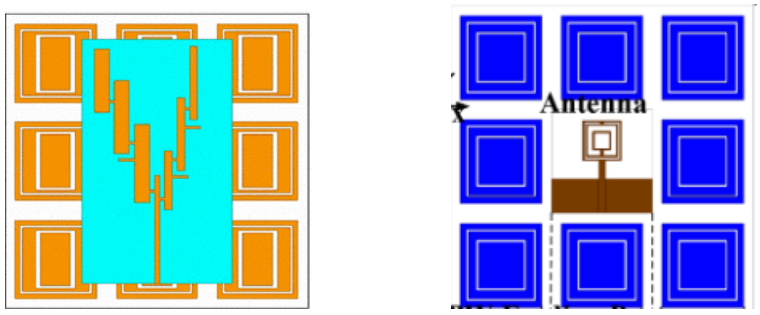

(a) (b)

Figure 2.29: Triple band antennas over triple band AMC reflector designs in : (a) [91], (b) [92].

In [93, 94], a gain enhancement of compact multiband antennas using triband AMC reflectors is proposed for WLAN /WIMAX applications. In [93] , a gain enhancement by amounts of 4.93, 5.92, 5.54 and 4.95 dB is acheived at the frequencies of 2.45, 3.5, 4.6 and 5.8 GHz, respectively. A triple band operation is achieved by using AMC reflectors (see Figure 2.30(a)). In [94], a triband antenna associated with dual band AMC reflector is proposed for Wireless Body Area Networks (WBAN), as shown in Figure 2.30(b). 4×4 AMC unit cell array is used at distances of 0.139 λ_L (2.45 GHz) from the antenna structure to enhance the gain of the triple band antenna and reduce the SAR by 90%. The antenna shows a maximum peak gain values of 4.69, 10.54, 7.45 dB centred at 2.45, 4.1, 6.5 GHz, respectively.

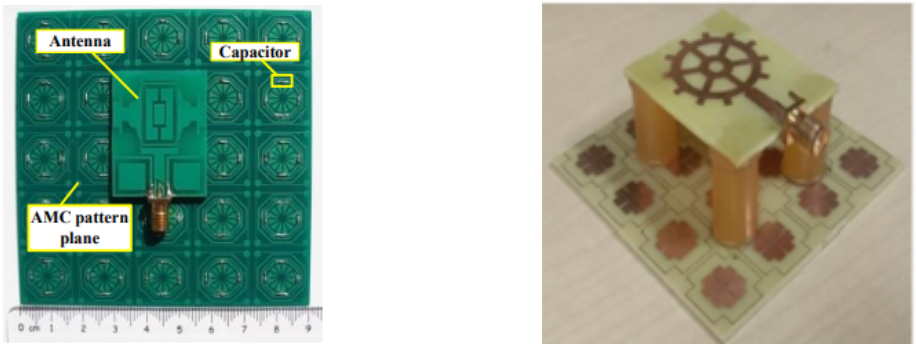

(a) (b)

Figure 2.30: Gain enhancement of multiband antennas over the triband AMC reflectors for WLAN /WIMAX applications presented in : (a) [93] , (b) [94].

Another CPW fed triband antenna over triband AMC is investigated in [95] for wearable application. An AMC reflector of 4×5 three concentric nested octagonal rings unit cell is used for gain enhancement and SAR reduction as it depicted in Figure 2.31. After incorporating the triple band AMC reflector, the antenna shows a reduced SAR of 99.8% with a gain enhancements of 3.4, 1.8, and 4 dB centred at 1.85 GHz (1.34–1.67 GHz) , 2.45 GHz (2.33–2.47 GHz) and 3.5 GHz,(3.55–3.7 GHz) to cover WLAN/WIMAX application.

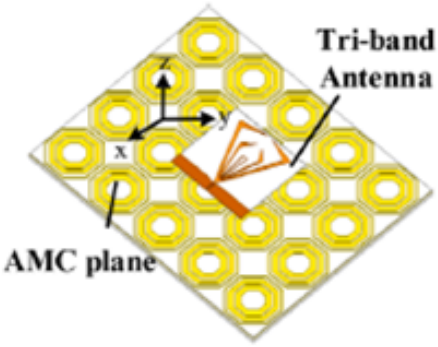

Figure 2.31: CPW fed triband antenna over the triband AMC reflector [95].

In [96], The dual band operation is achieved by engraving a circular ring, circular slots in the CPW fed patch antenna while the third operating band can be generated by embedding to antenna substrate a mushroom type composed of square metal patches with shorting pin (see Figure 2.32). The proposed configuration shows an omnidirectional radiation pattern with appreciable gains over the three operating band in the range of 530 MHz (2.28–2.81 GHz), 470 MHz (3.29–3.76 GHz) and 1250 MHz (4.87–6.12 GHz) which can cover all the 2.4/5.2/5.8 GHz WLAN bands and 2.5/3.5/5.5 GHz WiMAX bands,respectively.

Figure 2.32: CPW fed patch antenna with metasuface structure [96].

Another method to improve the antenna bandwidth and especially the gain by using an AMC reflector made of CSRR (Complementary Split Ring Resonator) shaped unit cells and characterized with three zeros-phase in the reflection coefficient [97]. The antenna is constructed by various ring in order to obtain the multifrequency behavior at 2.4, 4.2, 5.8 GHz as seen in figure 2.33. The suggested radiating configuration shows a three wide impedance bandwidths ranging from 2.2-2.49, 2.94-4.96, and 5.41-6.62 GHz, which cover WLAN/ WMAX frequency with gain enhancements by amount of 4.22 , 4.42, 3.46 dB, at three desired resonant frequencies, respectively.

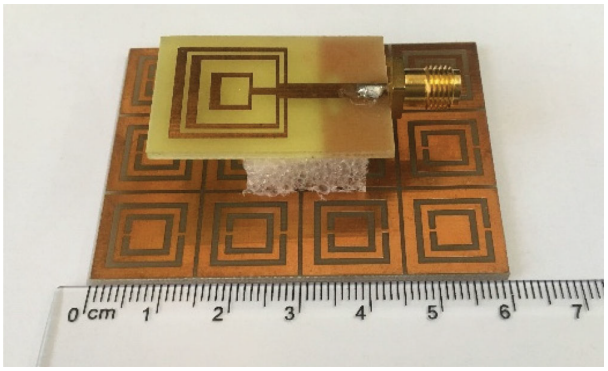

Figure 2.33: Multiband antenna over the CSRR AMC reflector [97].

Further approach has been investigated in [98] by designing a wideband/multiband antenna simultaneously (see Figure 2.34 and Figure 2.35). A wideband bowtie antenna is associated with dual band AMC reflector to generate a triple band behavior with and enhanced performances for the European standards of 4G/5G and Wi-Fi 2.4/5/6E. The proposed configuration(see Figure 2.34) shows enhanced peak gains of 8, 9.1, and 10.5 dB over a triple band in the range of 2.4–2.7 GHz, 3.4–3.8 GHz, and 5.17–6.45 GHz, respectively.

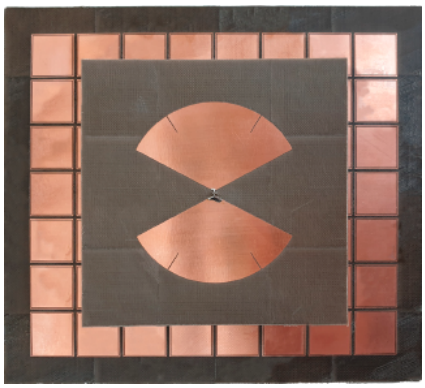

Figure 2.34: Wideband bowtie antenna associated with dual band AMC reflector [98].

In [99], another wideband/multiband planar inverted-F antenna (PIFA) over an metasurface ground plane is proposed for wireless communication applications (see Figure 2.35). The aim of this work is to achieve wideband /multiband characteristics with a reduced size. The combination of the antenna and the metasurface together generates a band stop from 1.8 to 3.2 GHz, therefore, two operating bandwidths could be achieved the first one at 1.3 GHz with narrow bandwidth while the second is extended from 2.8 to 6.5 GHz with a size reduction of 27% .

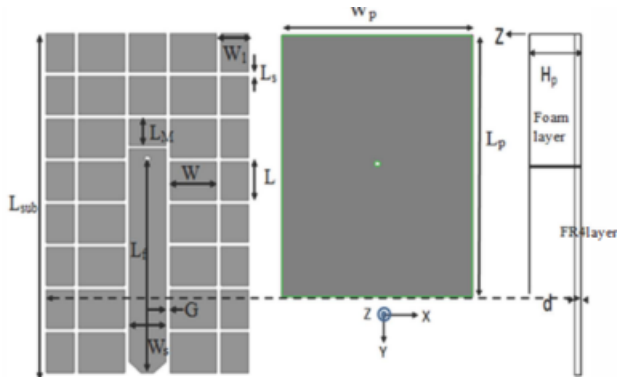

Figure 2.35: Combination of multiband PIFA antenna with EBG structure [99].

The main performances of the previous works presented in the state of the art are listed in Table 2.2.The use of AMC reflectors in multiband antennas has proven effective in enhancing antenna gain across multiple frequency bands, all while preserving a compact design. This improvement makes AMC-reflector-based multiband antennas well-suited for applications that require efficient performance across diverse frequencies within space-constrained environments.

Table 2.2: Multiband antennas based on artificial materials

Ref	Overall size dimension(λ_L) (width × length × height)	Frequency (GHz)	Bandwidth (%)	Max Gain(dB)
[85]	0.23 λ_L× 0.30 λ_L×0.016λ_L	3.27, 5.11	12.23, 21.96	6.46, 7
[86]	1.04 λ_L×1.04λ_L×0.065λ_L	2.62, 4.89	13.8, 6	10, 13.7
[87]	0.64λ_L×0.64λ_L×0.16λ_L	2.05, 5.05	40, 49.5	6.6, 7.4
[88]	0.98λ_L×0.98λ_L×0.04λ_L	2.45, 5.7	3, 25	/
[89]	0.8λ_L×0.64λ_L×0.008λ_L	2.45, 6	17.67, 9.61	2, 5.8
[93]	0.7λ_L× 0.7λ_L×0.01 λ_L	3.5, 5.8, 7.5, 8.08	/	7.53, 9.08, 8.18, 7.65
[94]	0.72λ_L×0.72λ_L×0.048λ_L	2.4, 3.5, 5.8	/	4.8, 5.1, 6.2
[95]	0.73λ_L×0.73λ_L×0.21 λ_L	2.45, 3.5, 5.8	14.8, 38.4, 5.3	5.4, 7, 6.4
[96]	0.34λ_L×0.18λ_L×0.008λ_L	2.54, 3.52, 5.8	5.2, 3.3, 5.6	/
[98]	1.28λ_L×1.14λ_L×0.12 λ_L	2.41, 3.4, 5.8	34, 4.9, 7.7	8, 9, 10.5
[99]	0.19λ_L×0.095 λ_L×0.38 λ_L	1.3, 3	40, 79.5	6.2, 5.6

λ_L : is the wavelength at the lowest resonant frequency.

2.6 Conclusion

In this chapter, the distinctive properties of EBG and AMC surfaces have been explored. EBG structures are characterized by two primary features: their ability to create frequency band gaps that prevent surface wave propagation, and their in-phase reflection capability when functioning as an AMC, allowing zero-degree reflection of incident waves at the resonance frequency. These unique features make EBG and AMC surfaces optimal for enhancing antenna performances. A comprehensive review of wideband and multiband antenna designs based on artificial materials has been conducted, focusing on the specific performance improvements achievable through the incorporation of these artificial materials. In the next chapter, we will propose the design of multiple wideband and multiband antennas utilizing novel AMC reflectors.

Chapter 3

AMC reflectors-based wideband antennas

3.1 Introduction

This chapter proposes two solutions aimed at enhancing the performance of wideband antennas. These solutions leverage AMC reflectors and target two specific applications: enhancing gain stabilization and front-to-back ratio (F/B), as well as reducing the antenna profile height. In pursuit of these objectives, several designs of AMC unit cells will be presented. A comprehensive parametric study will be conducted to justify the selection of these designs. Subsequently, all prototypes will be measured and compared to simulated results to validate their effectiveness. Furthermore, the obtained results will be compared to existing published work to demonstrate the superiority of the proposed solutions.

3.2 Application I: Gain stability improvement of a wideband antenna using AMC reflector

3.2.1 Antenna geometry

The proposed structure is composed of bowtie antenna, as shown in Figure 3.1(a). The bowtie antenna has been slightly modified by bending the edges of both triangles to provide better impedance matching in the operating band, especially at the lower frequencies.

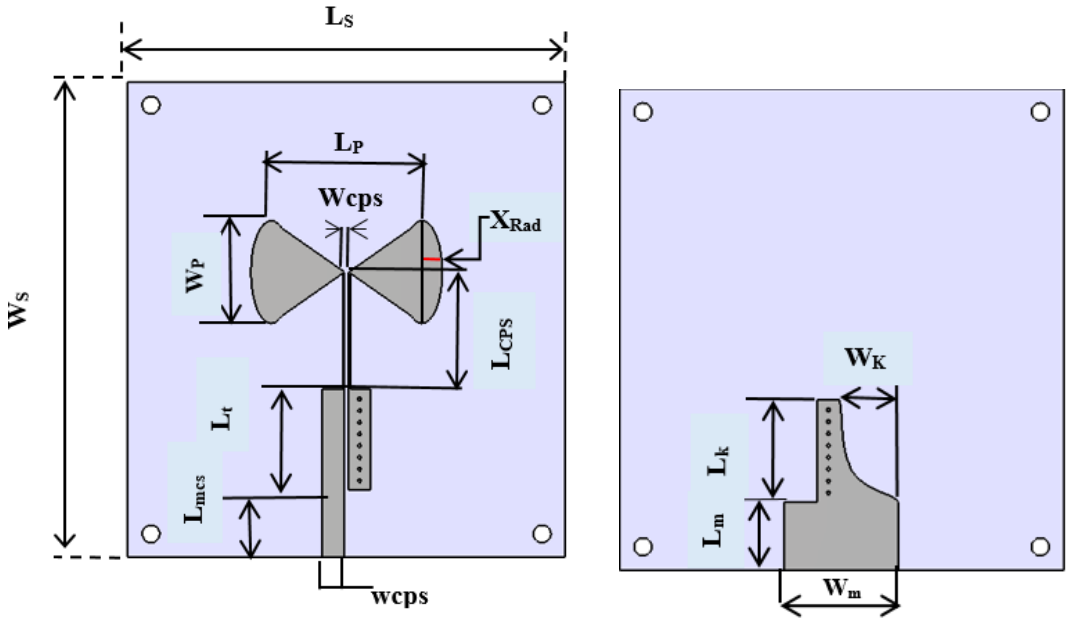

(a) (b)

Figure 3.1: Antenna geometry, (a) Top view , (b) Bottom views .

The impact of these edge modifications will be discussed in detail in the upcoming section. The bowtie antenna is printed on a Roger RT885 dielectric layer in size of (75×81.5) mm^2 with thickness of 1.57 mm, relative permittivity of 2.2 and loss tangent of 0.009. In order to feed the antenna with an asymmetric feed line, a balun is employed. This balun consists of two transmission lines: microstrip line (MCS), coplanar stripline (CPS) printed on the same substrate. The 50 Ω SMA connector (coaxial) is mounted on the edge of the antenna substrate with its central pin connected to microstrip line (MCS). Additionally, 8 vias are incorporated on the right side of the CPS line to establish an electrical connection between the CPS line and the ground plane located on the backside of the dielectric layer. In order to achieve wideband characteristics, a progressive transition is inserted on the bottom of the antenna substrate, as shown in Figure 3.1(b). The dimensions are listed in Table 3.1. This configuration was previously explored in [100], where the antenna exhibited omnidirectional radiation with a maximum realized gain variation of 9 dB across a relative impedance bandwidth of 46% (4.08–6.4 GHz). The objective of the following study is to achieve a directive, stable gain (broadside gain variation less than 1 dB) over the widest possible bandwidth in C band. Initially, by employing a standard square patch AMC reflector.

Table 3.1: Dimensions of the designed bowtie antenna and its feeding system.

Parameter	L_s	W_s	L_p	W_p	X_{Rad}	L_{cps}	W_{cps}
Value (mm)	75	81.50	25.80	17.5	3.5	19.95	0.3
Parameter	L_{mcs}	L_m	W_{mcs}	W_m	L_t	L_k	W_k
Value (mm)	12	12	3.77	19.25	17.29	17.29	9.90

3.2.2 Bowtie antenna loaded with standard square patch (SSP) AMC reflector

The overall antenna structure is consisted of two dielectric substrates, separated by an airgap layer, as depicted in Figure 3.2(a). The upper dielectric layer consists of the bowtie antenna with dimensions of 75× 81.5 mm^2, while the bottom layer compromises 5×8 arrangement of SSP unit cells with total dimensions of 68.9 × 42.8 mm^2, as shown in Figure 3.2(b). In order to maintain the balun's characteristics (prevent the performances degradation), particularly its operating bandwidth, no unit cell has been placed behind it.

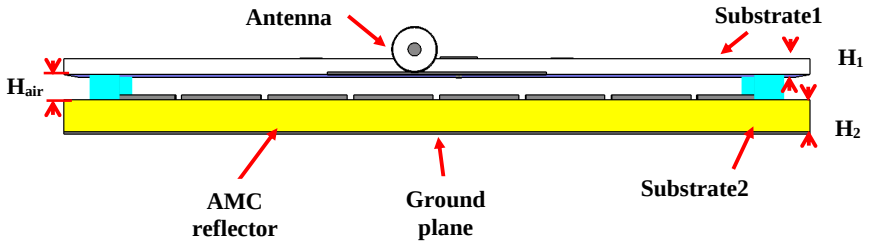

(a)

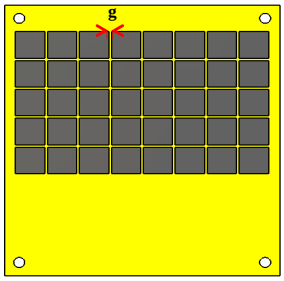

(b)

Figure 3.2: Geometry of the proposed bowtie antenna with 5×8 SSP unit cell AMC reflector, (a) Side view, (b) Top view of the AMC reflector.

The air layer is sustained by four plastic bolts with nuts, resulting in a total thickness of 6.77 mm (0.089 λ_L, where λ_L is the wavelength at the lowest frequency 3.74 GHz). The proposed AMC unit cell is shown in Figure 3.3(a), it consists of simple square patch, printed on a 3.2 mm-thickness FR4 substrate layer with a permittivity of 4.3 and a loss tangent of 0.025. The dimensions of the suggested unit cell are listed in Table 3.2. In order to investigate the unique feature of the AMC surface (in-phase reflection), the proposed unit cell is surrounded by PEC boundary in the direction of the electric field (E-field) and PMC boundary in the direction of the magnetic field (H-field). Additionally, a wave excitation introduced through an upper wave port, as shown in Figure 3.3(b). The AMC unit cell is designed and simulated using CST microwave studio software and its reflection phase characteristics is depicted in Figure 3.3(c). The SSP AMC unit cell operates within in-phase bandwidth (where reflection phases range between - 90° and + 90°), ranging from 4.55 to 8 GHz, corresponding a relative bandwidth of 54%.

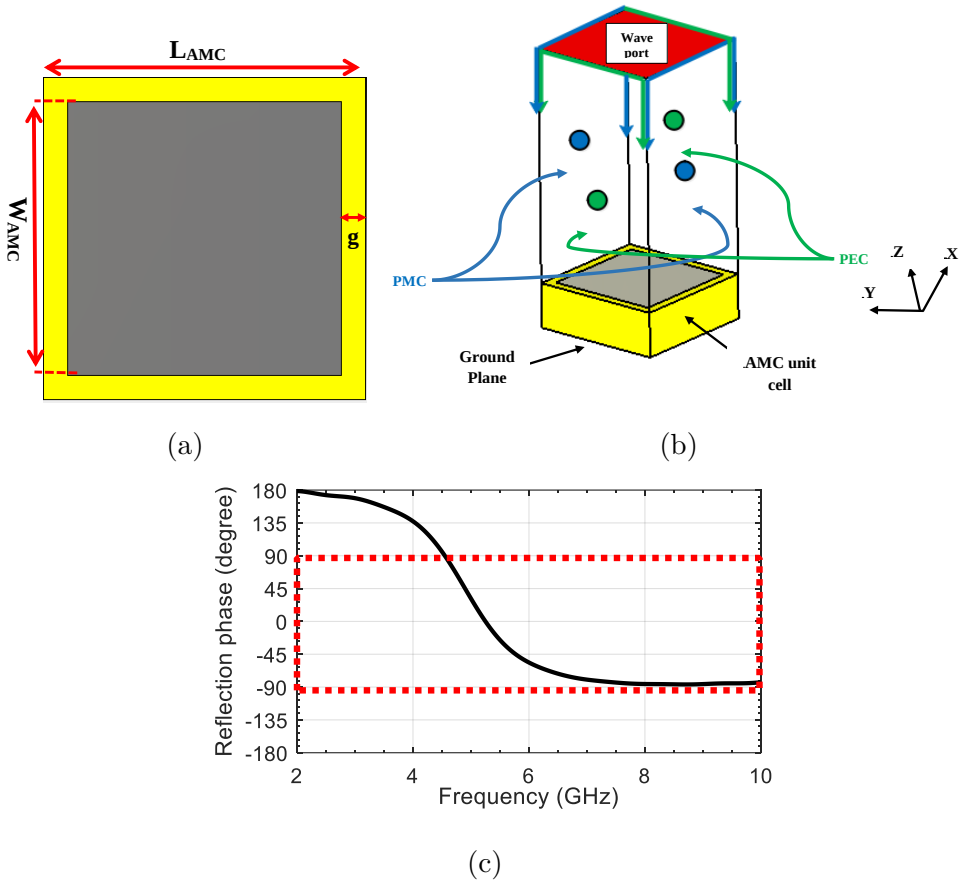

Figure 3.3: SSP unit cell, (a) Its geometry, (b) Its electromagnetic model, (c) Simulated reflection phase response.

Table 3.2: Dimensions of the designed SSP AMC unit cell.

Parameter	L_{AMC}	W_{AMC}	g
Value (mm)	9.4	8	0.7

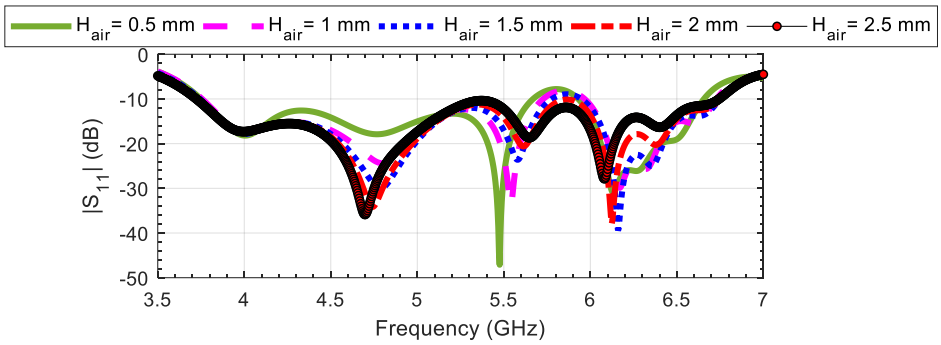

(a)

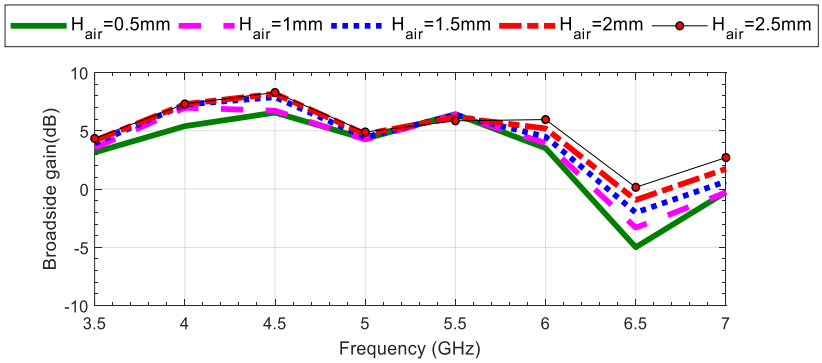

(b)

Figure 3.4: Effect of the air layer thickness on the antenna characteristics, (a) Reflection coefficient, (b) Broadside gain.

A parametric study is conducted in order to investigate the effect of the air layer on the antenna performances, thus, two parameters are investigated the reflection coefficient and the broadside gain (Theta = phi = 0°), as illustrated in Figure 3.4. When adjusting this thickness within the range of 0.5 to 2.5 mm, it becomes evident that the proximity between the AMC reflector and the bowtie antenna has a notable impact on impedance matching and the variation in broadside gain. From Figure 3.4(a), it is clearly noticeable that as the air layer thickness (H_{air}) decreases, there is a mismatch occurring within the frequency range of 5.6–6.0 GHz. This mismatch results in a narrower input impedance bandwidth. Thus, for $H_{air} \leq 1.5$ mm, a relative impedance

bandwidth of 39% is reached, while it expands to 57% for $H_{air} \geq 2$ mm. Furthermore, for all investigated values H_{air}, the broadside gain remains relatively steady within the frequency range of 3.74–6 GHz. However, there is a significant drop from 0 dB to -5 dB at 6.5 GHz when H_{air} is set at 2.5 mm and 0.5 mm, respectively. However, taking into account the large gap (H_{air}) between the two substrates tends produce a bulky antenna structure. As a result, an optimal air layer thickness (H_{air}) of 2 mm is chosen to ensure both impedance matching and stable broadside gain across a broad frequency range.

Figure 3.5 Depicts the Simulated reflection coefficient and broadside gain of the optimized configuration bowtie antenna separated by 2 mm air layer from 5× 8 SSP unit cells AMC reflector. The results reveal that the proposed configuration functions effectively in the frequency range of 3.74 to 6.75 GHz, where the reflection coefficient remains below -10 dB ($\mid S_{11} \mid \leq$ -10 dB) which represents a relative bandwidth of 57.38%. The broadside gain varies between 4 and 8 dB within the operating band of 4–6 GHz, but experiences a significant drop to -0.93 dB at 6.5 GHz. This results in an unstable gain within the operating band of 3.74–6.75 GHz, characterized by an approximate 8 dB variation in gain.

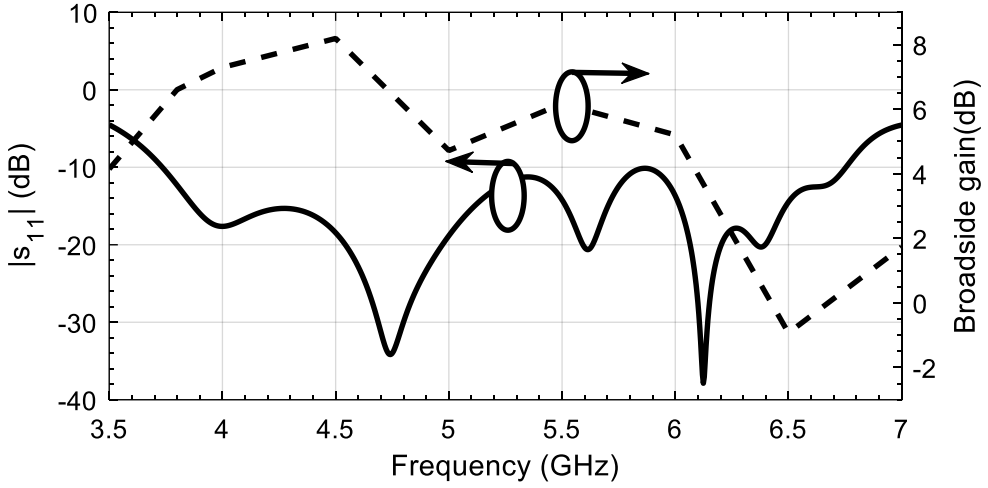

Figure 3.5: Simulated reflection coefficient and broadside gain of the optimized bowtie antenna with 5×8 SSP unit cell AMC reflector.

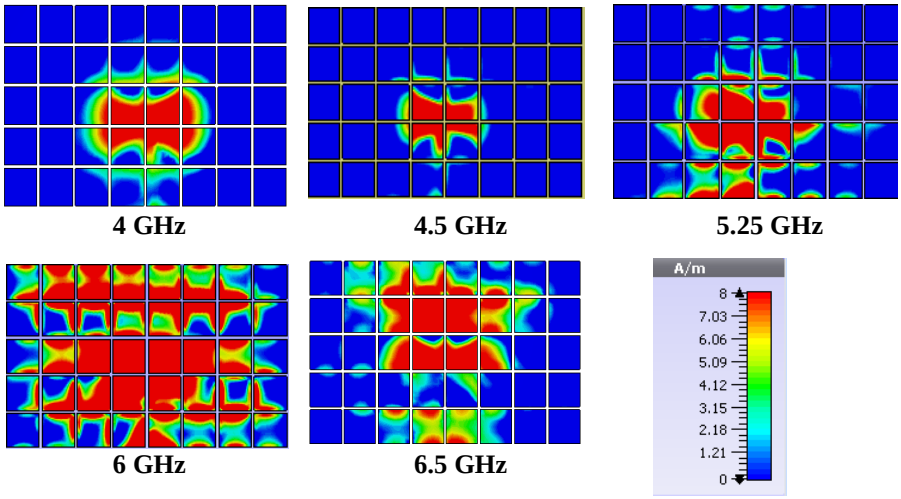

Figure 3.6: Simulated surface current distribution on the SSP AMC reflector at: 4 , 4.5 , 5.25, 6, 6.5 GHz.

To further understand the structure behavior, we examined the surface current distribution on the AMC reflector at five specific frequencies: 4 GHz, 4.5 GHz, 5.25 GHz, 6 GHz, and 6.5 GHz, as it is depicted in Figure 3.6.
At the first three frequencies, the current is primarily concentrated within a limited surface area positioned directly beneath the radiating bowtie antenna. Conversely, at 6 and 6.5 GHz, the current distribution on the AMC reflector extends across a broader surface area. This variation in the current distribution affects the behavior of the AMC, leading to destructive interference. This interference phenomenon can provide an explanation for the decrease in the observed broadside gain at 6.5 GHz. In order to enhance the stability of gain, two AMC unit cells shapes are introduced and investigated in the following section.

3.2.3 Proposed unit cell investigations

To enhance the gain at 6.5 GHz, two unit cell shapes have been developed. These designs involve modifying the standard patch unit cell without disrupting the impedance matching. This is achieved by altering the edges of the proposed unit cell, creating octagonal and cross-shaped configurations, as illustrated in Figure 3.7. Both unit cells are printed on a 3.2 mm-thickness FR4 substrate layer with a permittivity of 4.3 and a loss tangent of 0.025. Their dimensions are summarized in Table 3.3.

The simulated reflection characteristics of both AMC unit cells are depicted in Figure 3.8. It can be seen that both unit cells operate within an in-phase bandwidth, (where reflection phases range between -90° and +90°), ranging from 4.81 to 6.84 GHz for the octagonal unit cell and from 4.41 to 6.17 GHz for the cross-shaped unit cell. This corresponds to a relative bandwidth of 34.8% and 33%, respectively.

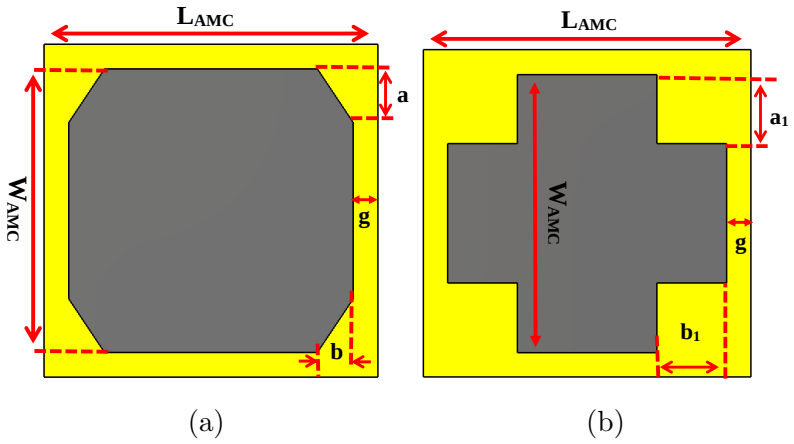

Figure 3.7: The proposed AMC unit cell geometries, (a) Octagonal AMC unit cell, (b) Cross-shaped AMC unit cell.

Table 3.3: Dimensions of the designed octagonal and cross-shaped AMC unit cells.

Parameter	L_{AMC}	W_{AMC}	g	a	b	a_1	b_1
Value (mm)	9.4	8	0.7	1	1.5	2.25	2.25

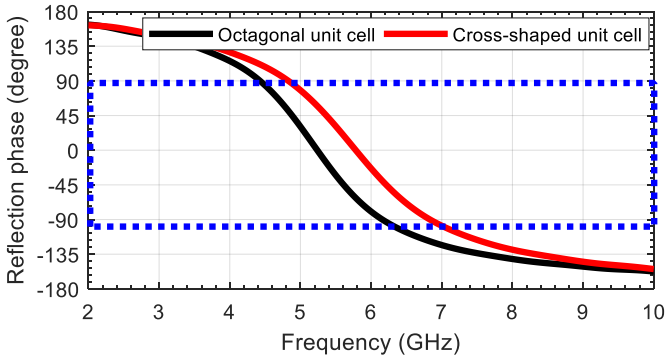

Figure 3.8: Simulated reflection phase responses of both octagonal and cross-shaped AMC unit cells.

a Bowtie antenna loaded with the octagonal AMC reflector

The bowtie antenna is, now, loaded with 5×8 octagonal unit cells AMC reflector, with an air layer of 2 mm, as illustrated in Figure 3.9. The effect of a and b parameters (see Figure 3.7(a)) on the antenna reflection coefficient and the broadside gain is investigated in Figure 3.10 and Figure 3.11, respectively.

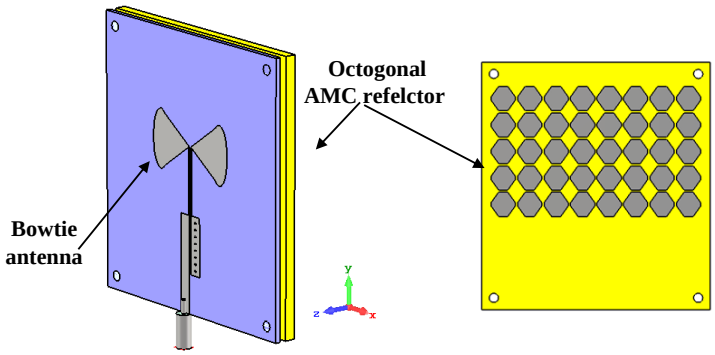

Figure 3.9: Bowtie antenna over the octagonal AMC reflector.

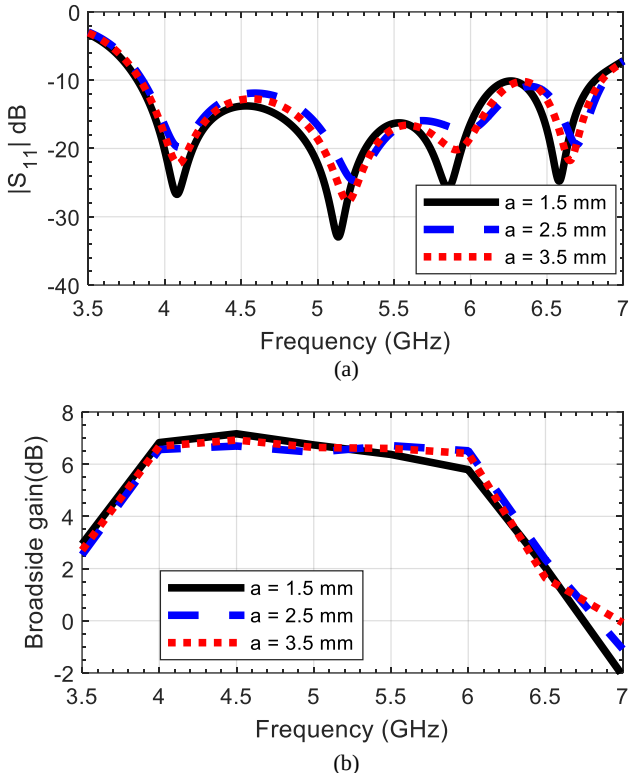

Figure 3.10: Effect of a parameter on the combined bowtie antenna with the AMC reflector performances, (a) Reflection coefficient, (b) Broadside gain.

It can be observed from Figure 3.10, that the effect of a parameter is less significant on the antenna impedance matching, as the values of this parameter increased. Across all investigated cases, as a increases, the gain remains stable over a frequency band ranging from 4 to 6 GHz. However, at 6.5 GHz, a dip in the broadside gain is observed, resulting in high gain variations of 5.13 dB, 5.17 dB, and 4.35 dB for the three cases of a = 1.5 mm, a = 2.5 mm, and a = 3.5 mm, respectively.

In addition, from Figure 3.11, it can obviously seen that for b = 3.5 mm, the impedance matching is deteriorate, especially in the frequency band of 4.55-4.80 GHz, therefore this case will not be considered in gain investigation. Furthermore, setting b to 1.5 and 2.5 mm leads to high gain variations of 5.16 dB and 4.35 dB, respectively, over the targeted bandwidth (4-6.5 GHz).

Finally, the combination of a = 3.5 mm and b = 2.5 mm is chosen as the optimal parameter configuration for gain stability.

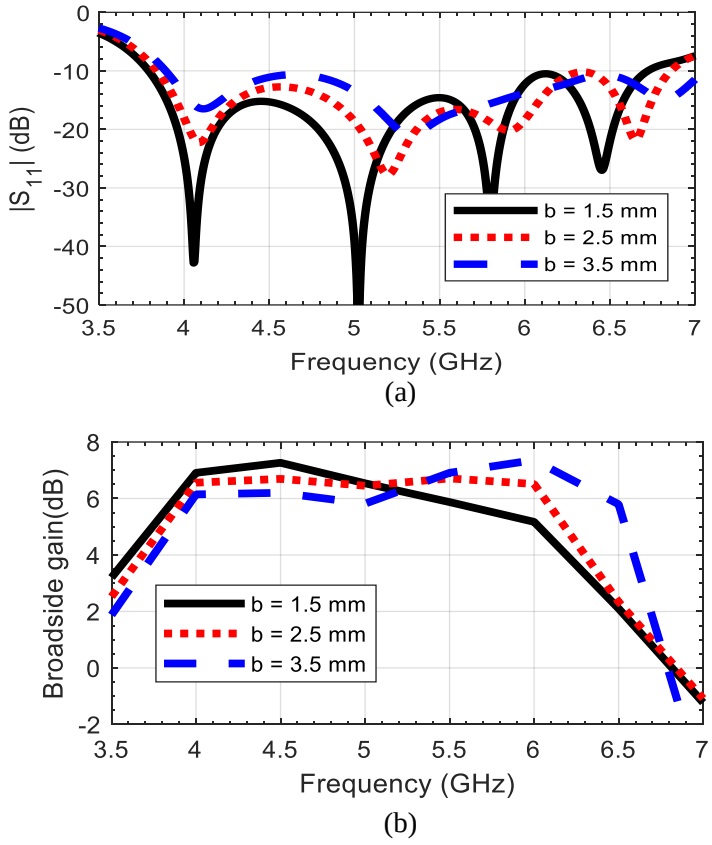

Figure 3.11: Effect of b parameter on the combined bowtie antenna with the AMC reflector performances, (a) Reflection coefficient, (b) Broadside gain.

The simulated performances (reflection coefficient, broadside gain) of the final optimized bowtie antenna over the octagonal AMC reflector is illustrated in Figure 3.12. The proposed combined configuration exhibits a wide impedance bandwidth ranging from 3.86 GHz to 6.5 GHz, which corresponding to 50% relative bandwidth. Despite maintaining stable gain across the frequency band of 3.86-6 GHz, a notable decrease in gain is observed, particularly at 6.5 GHz, resulting in a high gain variation of 4.35 dB. It is worth to underline that this configuration exhibits an improvement in the broadside gain at this frequency compared to the SSP AMC reflector. Specifically, the gain increases from -0.93 dB to 2.34 dB, marking a gain enhancement of 3.27 dB.

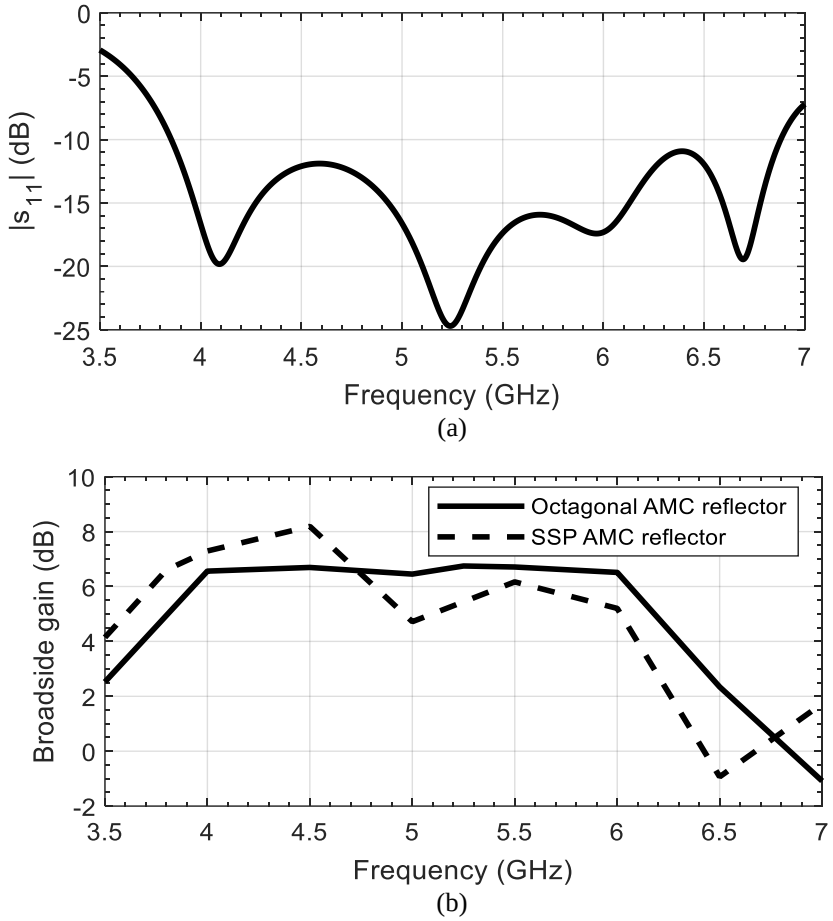

Figure 3.12: Simulated characteristics of the bowtie antenna over the octagonal AMC reflector, (a) Reflection coefficient, (b) Broadside gain (in comparison to the SSP AMC reflector).

In addition, the radiation pattern of the proposed configuration is also depicted in Figure 3.13 for two main cuts (E-plane and H-plane) at 4, 5, 6, 6.5 GHz, respectively. It can obviously seen that the bowtie antenna loaded with the octagonal AMC reflector demonstrates a unidirectional radiation pattern with high gain of 7.26 ,6.78 and 6.61 dB at the three frequencies 4,5 and 6 GHz, respectively . However, at the frequency of 6.5 GHz, the maximum gain is 3 dB. Furthermore, surfaces current distribution on the octagonal-based AMC reflector is given in Figure 3.14, at 4, 4.5, 5.25, 6, and 6.5 GHz. It can be noticed that the surface current has significantly reduced compared to those observed in the case of SSP-based AMC reflector (see Figure 3.6). This current configuration fails to meet our specifications, specifically the requirement for a gain variation of less than 1 dB across the desired frequency band of 4-6.5 GHz. Consequently, we are exploring the use of a cross-shaped AMC reflector.

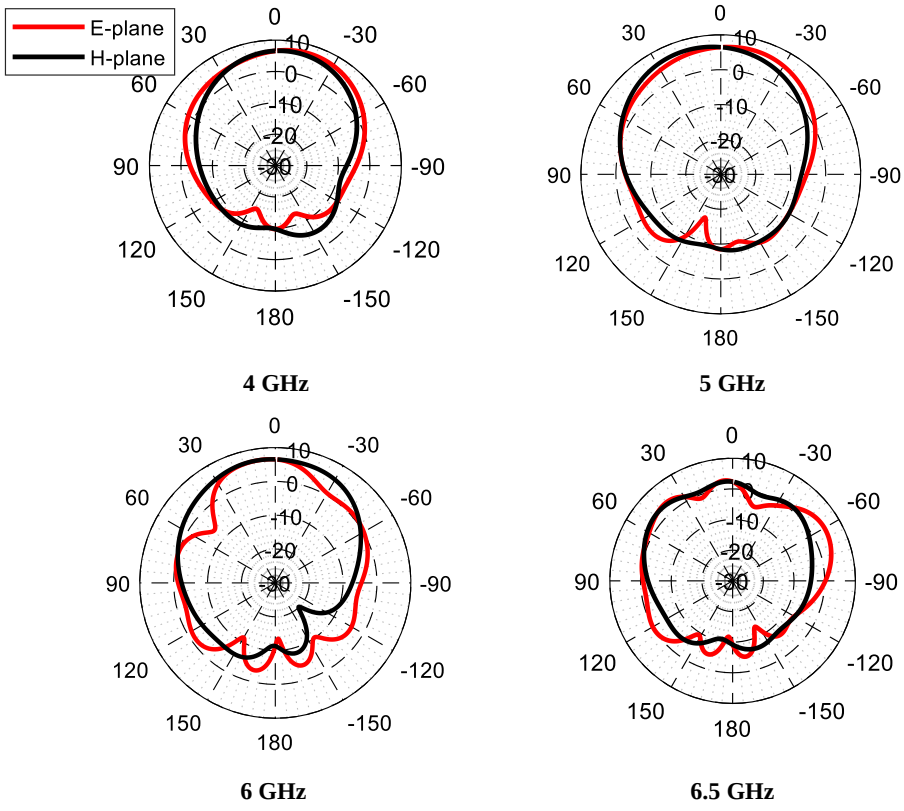

Figure 3.13: Simulated radiation pattern (in gain) of the bowtie antenna over the octagonal AMC reflector.

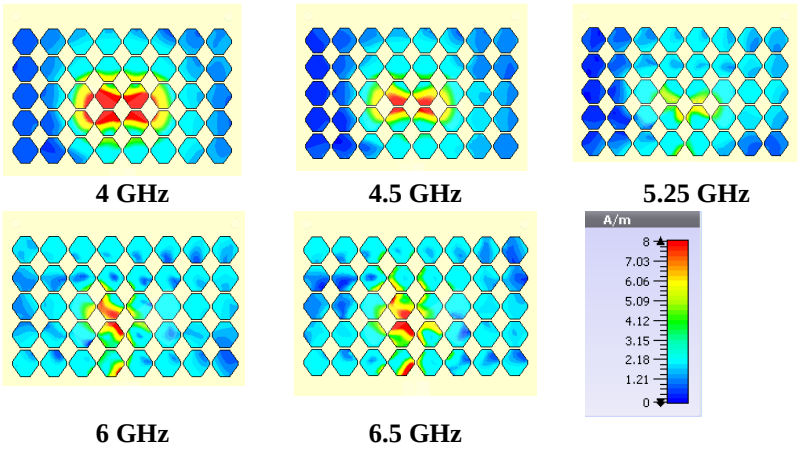

Figure 3.14: Simulated surface current distribution on the octagonal AMC reflector at 4 , 4.5 , 5.25, 6, 6.5 GHz..

b Bowtie antenna loaded with the cross-shaped AMC

The bowtie antenna is loaded with 5×8 cross-shaped unit cells AMC reflector, with an air layer of 2 mm, as illustrated in Figure 3.15. The effect of a_1 nd b_1 parameters (see Figure 3.7(b)) on the antenna reflection coefficient and the broadside gain is investigated in Figure 3.17 and Figure 3.18, respectively. It is observed that as a_1 parameter increases, the impedance matching tends to deteriorate.

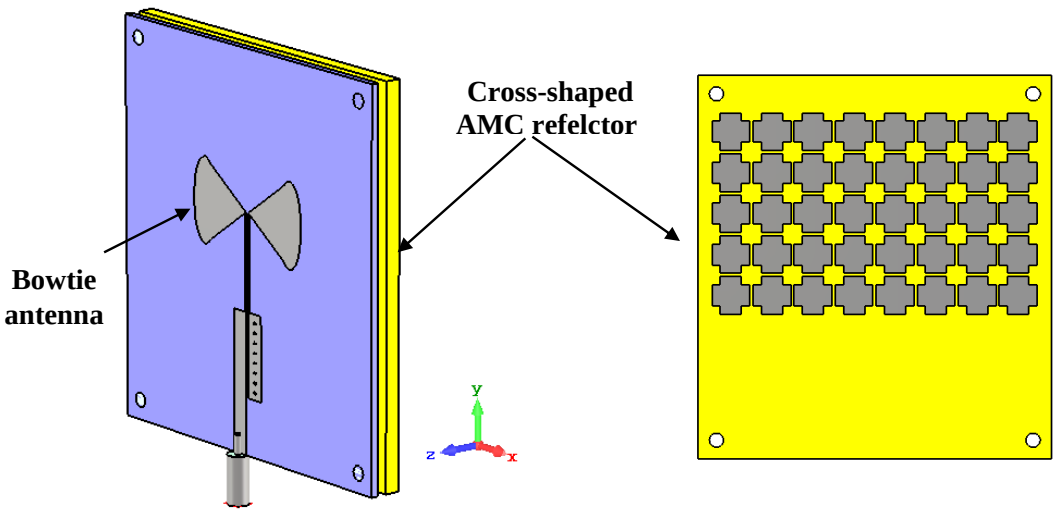

Figure 3.15: Bowtie antenna loaded with the cross-shaped AMC reflector.

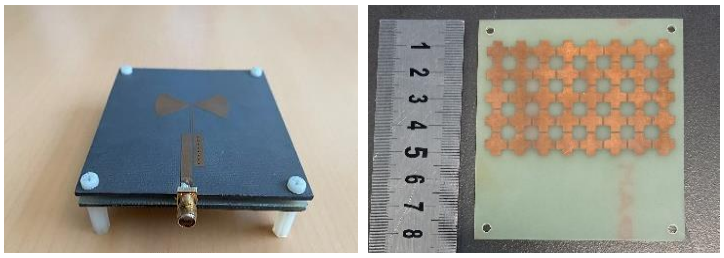

(a) (b)

Figure 3.16: The fabricated antenna prototypes, (a) The assembly, (b) AMC reflector.

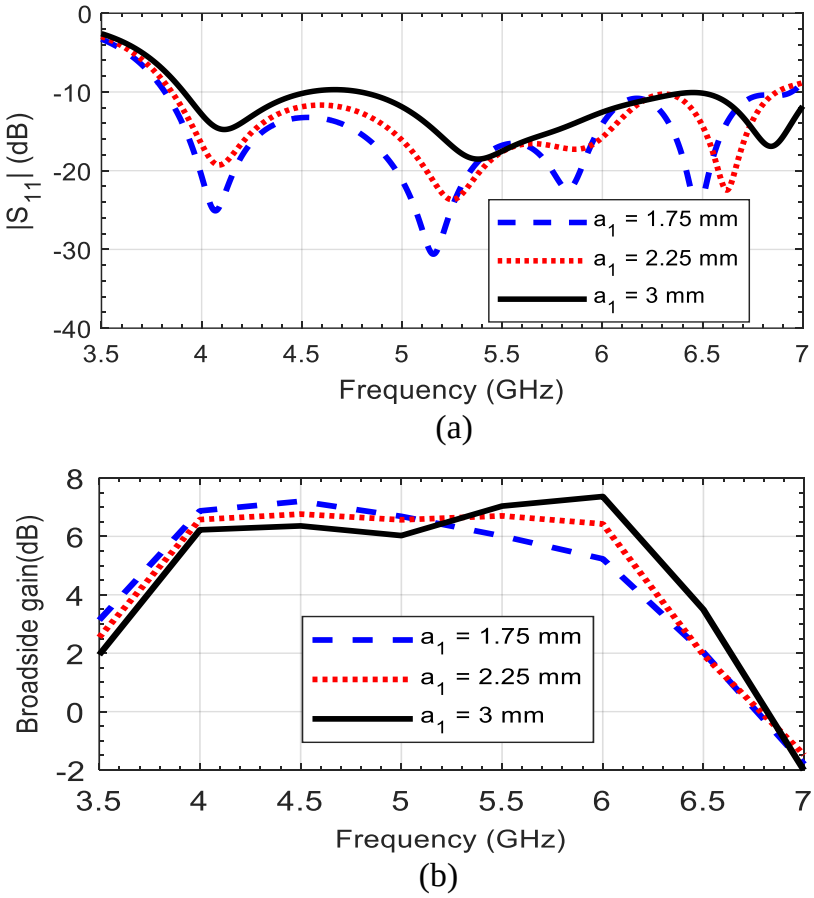

Figure 3.17: Effect of a_1 parameter on the combined bowtie antenna with the cross-shaped AMC reflector characteristics, (a) Reflection coefficient,(b) Broadside gain.

For $a_1 = 3$ mm, the impedance matching tends to deteriorate. Therefore, this particular case is excluded from the gain investigation. For $a_1 = 1.75$ mm and $a_1 = 2.25$ mm, the gain remains stable across the frequency band of 4-6 GHz. However, at 6.5 GHz, it decreases significantly to 1.95 dB and 2.41 dB, resulting in a high gain variation of 4.82

dB and 4.64 dB, respectively, across the band of interest (4-6.5 GHz). Furthermore, as b_1 parameter increase, no significant effect is observed on the antenna reflection coefficient and broadside gain. In conclusion, $a_1 = 2.25$ mm and $b_1 = 2.25$ mm are selected as the optimal parameters for gain stabilization. The bowtie antenna backed by the cross-shaped AMC reflector is fabricated and assembled, as shown in Figure 3.16. Its final optimised dimensions are give in Table 3.4.

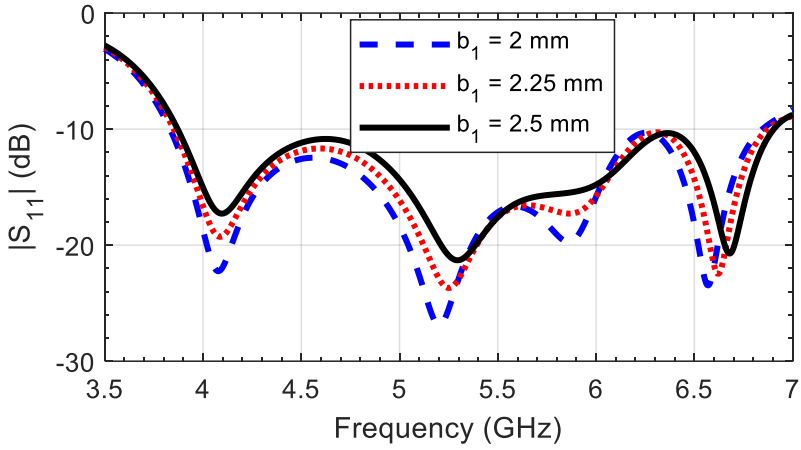

(a)

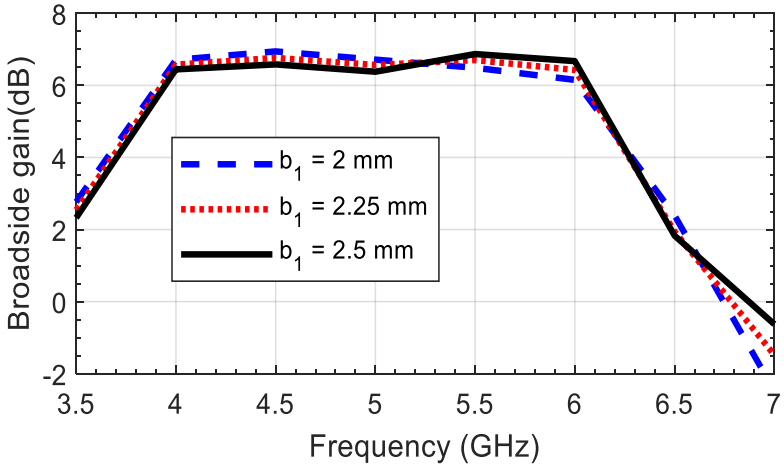

(b)

Figure 3.18: Effect of a_1 parameter on the combined bowtie antenna with the octagonal AMC reflector characteristics, (a) Reflection coefficient, (b) Broadside gain.

Table 3.4: Dimensions of the designed bowtie antenna loaded with the cross-shaped AMC reflector.

Parameter	L_s	W_s	L_p	W_p	X_{Rad}	L_{cps}	W_{cps}	H_{air}	L_{AMC}	W_{AMC}
Value (mm)	75	81.50	25.80	17.5	3.5	19.95	0.3	2	9.4	8
Parameter	L_{mcs}	L_m	W_{mcs}	W_m	L_t	L_k	W_k	a_1	b_1	g
Value (mm)	12	12	3.77	19.25	17.29	17.29	9.90	2.25	2.25	0.7

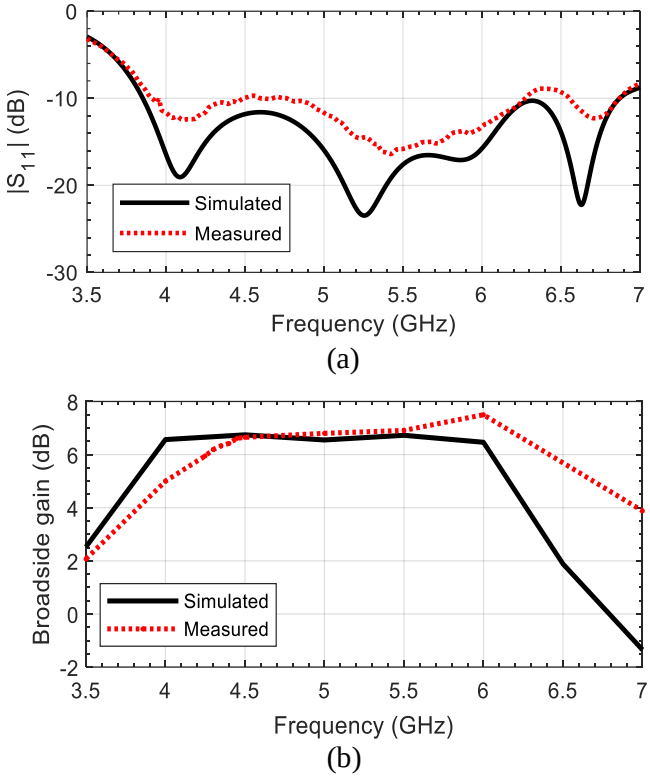

Figure 3.19: Simulated and measured characteristics of the proposed bowtie antenna over the cross-shaped AMC reflector, (a) Reflection coefficient, (b) Broadside gain.

The reflection coefficient is measured using an Agilent N5224 vector network analyzer in CDTA (Centre de Développement des Technologies Avancées, Algeria) and plotted in Figure 3.19 (a). The measured impedance bandwidth for $\mid S_{11} \mid \leq -10$ dB, is ranging from 3.85 to 6.5 GHz, which corresponds to a wide relative impedance bandwidth of 51%. A good agreement between simulation and measurement results is observed except a slight shifts in the frequency band of 6.25-6.5 GHz, which can be explained by the measurement errors. In addition, simulated and measured broadside gain of the fabricated prototype versus frequency is shown in Figure 3.19 (b). It can be observed

that the measured gain agrees well in 4.5-6 GHz band with the simulated one except at 4 GHz , it decrease to 5.16 dB at 4 GHz , which leads to 2.4 dB gain variation. This discrepancy can be explained by the antenna support in the anechoic chamber. The simulated and measured radiation patterns in E and H planes at 4, 5 and 6 GHz, are compared in Figure 3.20. For both planes and all frequencies, a relatively good agreement is obtained between simulation and measurement results. The fabricated structure exhibits unidirectional radiation patterns with measured maximum realized gains of 5.16, 6.8 and 7.5 dB at 4, 5, and 6 GHz, respectively.

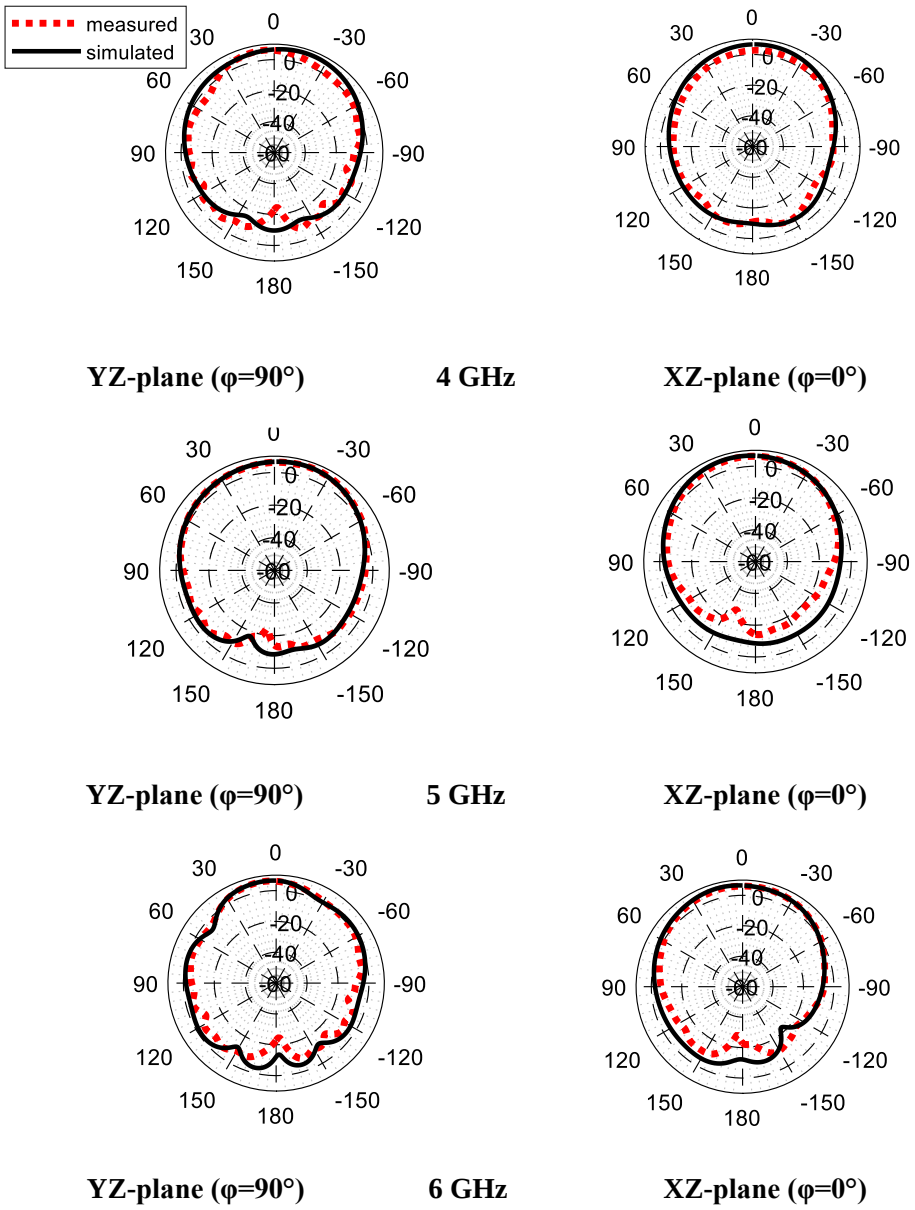

Figure 3.20: Simulated and measured radiation pattern (in gain) of the bowtie antenna over the cross-shaped AMC reflector.

3.2.4 Parametric study on bowtie antenna loaded with the Modified Cross Shape AMC reflector

a Modified Cross Shaped Unit cell

To enhance the gain stabilization, the main idea is to reduce the surface current circulation on the AMC reflector by reducing the AMC unit cell surface area. Conse-

quently, the couple (a_1, b_1) have been increased significantly to reduce the cross-shaped unit cell surface. As observed in Figure 3.21, simultaneously increasing a_1 and b_1 causes the operating band to shift towards higher frequencies. Specifically, when (a_1, b_1) are increased from (2.25, 2.25) mm to (3.55 , 3.65) mm, the in-phase reflection is shifted from 5.9 to 7.16 GHz with operating frequency band ranging from 4.9 to 7 GHz and from 6 to 8.28 GHz, respectively.

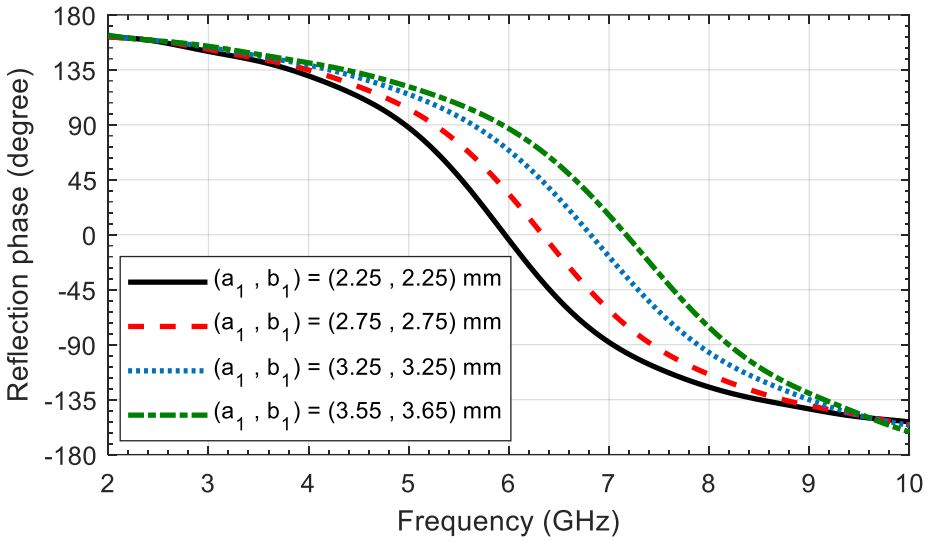

Figure 3.21: Impact of the cross-shaped AMC unit cell parameters on the reflection phase response.

To restore the operating band towards the target frequency band (3 to 7 GHz), two conducting T strips are added to the structure, as shown in Figure 3.22. This novel unit cell is printed on a 3.2 mm-thickness FR4 substrate layer with a permittivity of 4.3 and a loss tangent of 0.025 and its dimensions are summarized in Table 3.4. A comparison between the reflection phase of the cross-shaped unit cell and Modified Cross shaped (MCS) unit cell is depicted in Figure 3.23. The MCS unit cell exhibits an in-phase reflection at 5.25 GHz with an operating frequency band ranging from 4.95 to 6 GHz. It corresponds to a relative bandwidth of 19%.

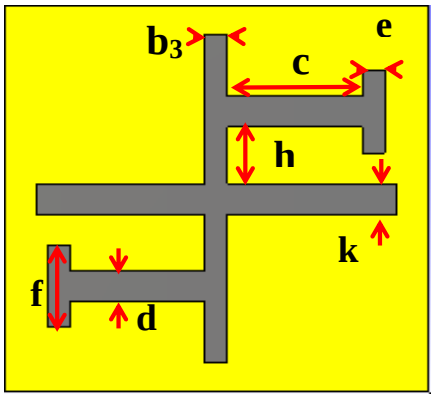

Figure 3.22: Modified Cross Shaped unit cell geometry.

Table 3.5: Dimensions of the proposed MCS unit cell.

Parameter	W_{AMC}	g	c	d	e	f	h	k	b_3
Value (mm)	8	0.7	3	0.75	0.53	2	1.5	0.7	0.9

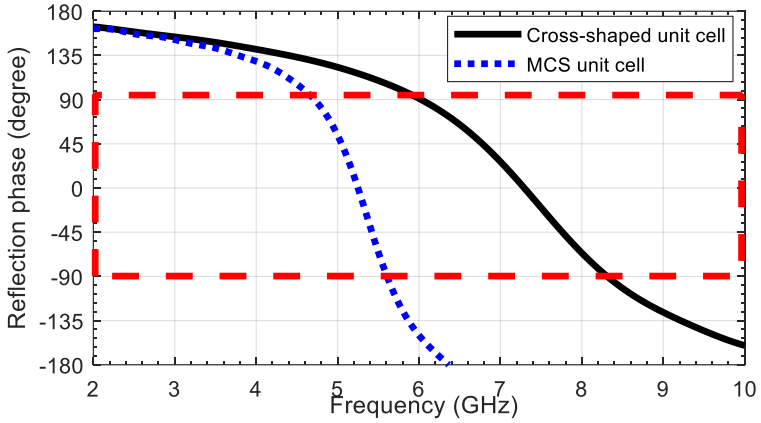

Figure 3.23: Simulated reflection phase response of the developed MCS unit cell.

b Bowtie antenna loaded with the Modified Cross Shape AMC reflector

The proposed MCS AMC reflector is illustrated in Figure 3.24. Figure 3.25 and Figure 3.26 illustrate the simulated reflection coefficient and the broadside gain for different dimensions of the MCS unit cell, specifically denoted as c, e, f and h. It is important to highlight that the antenna impedance matching is not affected by the variation of these parameters. In addition the parameters selected for investigation have been chosen due to their significant impact on the antenna gain.

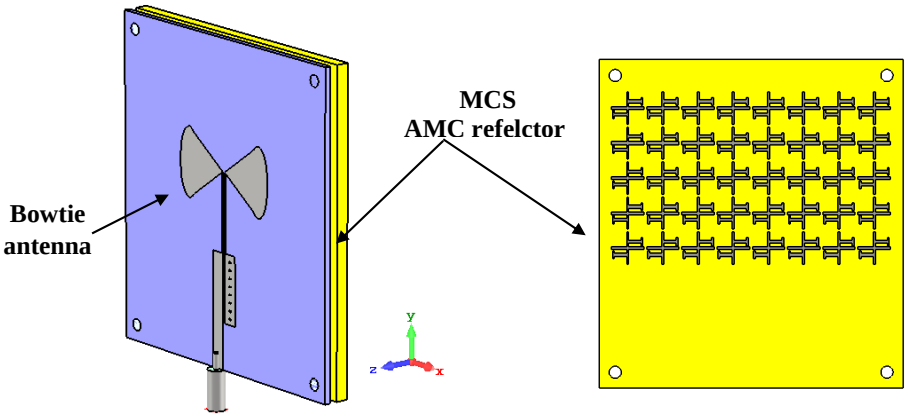

Figure 3.24: Bowtie antenna over the MCS AMC reflector.

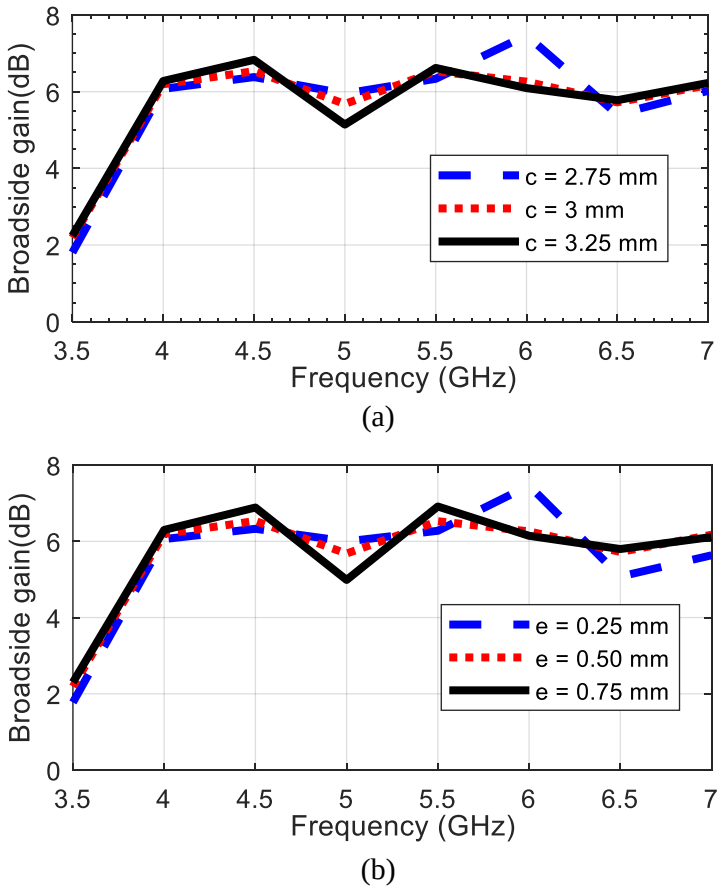

Figure 3.25: Simulated broadside gain of the bowtie antenna over the proposed AMC reflector for different modified cross shape (MCS) unit cell dimension variations, (a) c parameter ,(b) e parameter.

From Figure 3.25(a), it's evident that when the parameter c is set to 2.75 mm and 3.25 mm, the antenna exhibits unstable gain behavior over the target frequency band, with gain variations of 2.07 dB and 1.68 dB, respectively.
However, when c is set to 3 mm, the antenna achieves a relatively stable gain with a low gain variation of 0.85 dB. From Figure 3.25(b), the parameter e is varied from 0.25 mm to 0.75 mm in increments of 0.25 mm. When e is set to either 0.25 mm or 0.75 mm, the broadside gain becomes unstable with gain variations of 2.39 dB and 1.93 dB, respectively. Conversely, when e is equal to 0.5 mm, a stable gain is achieved with a minimal gain variation of 0.85 dB.

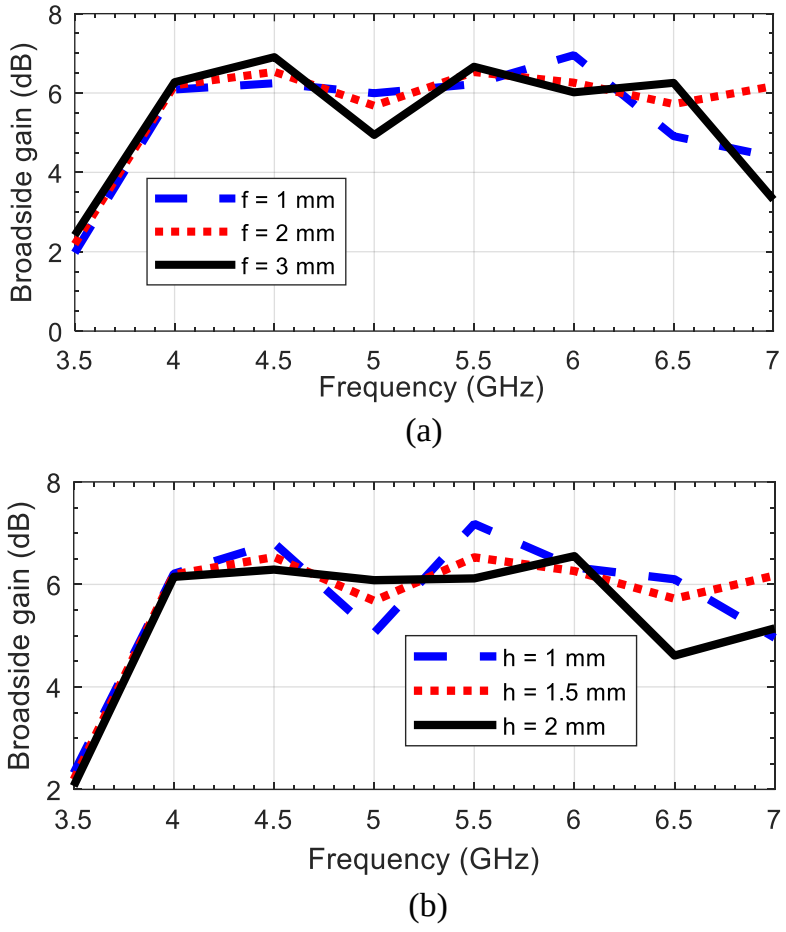

Figure 3.26: Simulated broadside gain of the bowtie antenna over the proposed AMC reflector for different modified cross shape (MCS) unit cell dimension variations, (a) f parameter, (b) h parameter.

The impact of f parameter is examined in Figure 3.26(a). When f is set to 1 mm and 3 mm, a gain variations of 2 dB and 1.96 dB are achieved, respectively. However, when f is set to 2 mm, the gain becomes more stable, exhibiting a variation of only 0.85 dB. Figure 3.26(b) shows the influence of parameter h, which represents the location of the conducting T strip, on the antenna's broadside gain. This parameter is varied from 1 mm to 2 mm with a step size of 0.5 mm. The most stable gain across a wide frequency range is achieved when h is set to 1.5 mm.
The final optimized dimensions of the proposed bowtie antenna loaded with MCS AMC reflector are listed in Table 3.6.

Table 3.6: Dimensions of the designed bowtie antenna loaded with the MCS AMC reflector.

Parameter	L_s	W_s	L_p	W_p	X_{Rad}	L_{cps}	W_{cps}	L_{mcs}
Value (mm)	75	81.50	25.80	17.5	3.5	19.95	0.3	12
Parameter	L_m	W_{mcs}	W_m	L_t	L_k	W_k	H_{air}	L_{AMC}
Value (mm)	12	3.77	19.25	17.29	9.90	17.29	2	9.4
Parameter	W_{AMC}	b_3	c	d	e	f	h	k
Value (mm)	8	0.5	0.3	0.75	0.5	2	1.5	0.7

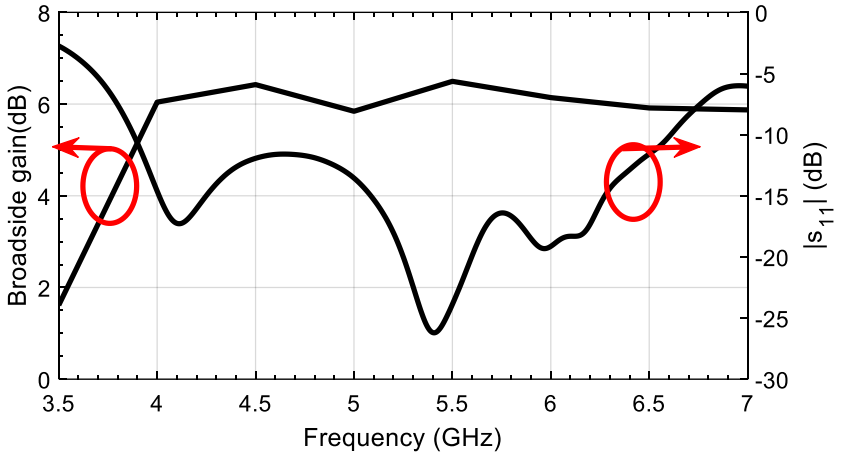

Figure 3.27: Simulated reflection coefficient and broadside gain of the proposed bowtie antenna over the MCS AMC reflector.

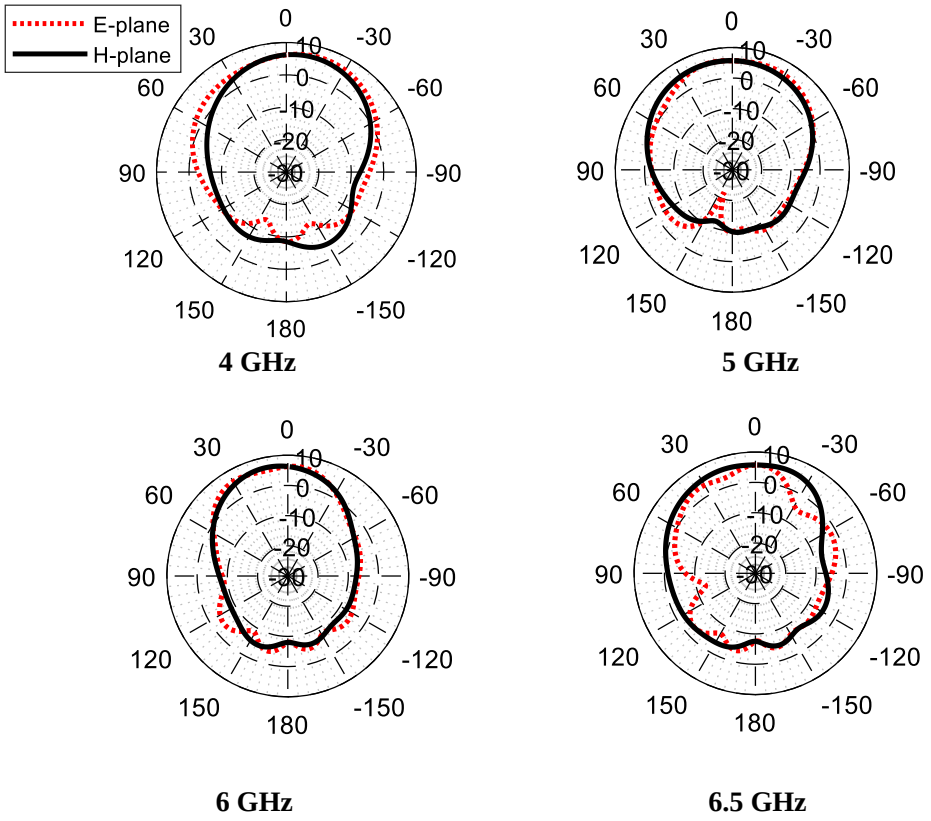

Figure 3.28: Simulated radiation pattern (in gain) of the proposed bowtie antenna over the MCS AMC reflector.

The final characteristics (reflection coefficient, realized gain and radiation pattern) of the optimized bowtie antenna over the MCS AMC reflector, are illustrated in Figure 3.27 and Figure 3.28. The proposed combined structure demonstrates a wide impedance bandwidth ranging from 3.9 GHz to 6.5 GHz, corresponding to a relative bandwidth of 50% with a stable gain of 0.85 dB gain variation. Moreover, this configuration exhibits an improvement in the broadside gain at 6.5 GHz compared to the SSP AMC reflector. The gain increases from -0.93 dB to 5.72 dB, Marking a notable gain enhancement of approximately 6.65 dB. In addition, the radiation pattern of the proposed bowtie antenna backed by the MCS AMC reflector is illustrated in Figure 3.28 for the E-plane and H-plane at 4, 5, 6, and 6.5 GHz, respectively. It can obviously observed that the final proposed structure demonstrates a unidirectional radiation pattern with high gain of 6.84, 6 and 6.38 dB and 5.74 dB at 4, 5, 6, and 6.5 GHz, respectively.

Table 3.7: Comparison of optimized bowtie antenna over the three selected AMC reflectors

The bowtie antenna over the proposed AMC reflector	Relative bandwidth (%)	Gain variation (dB)
Octagonal AMC	(3.86-6.5) 51%	4.35
Cross-shaped AMC	(3.85-6.5) 51.2%	4.64
MCS AMC	(3.9-6.5) 50%	0.85

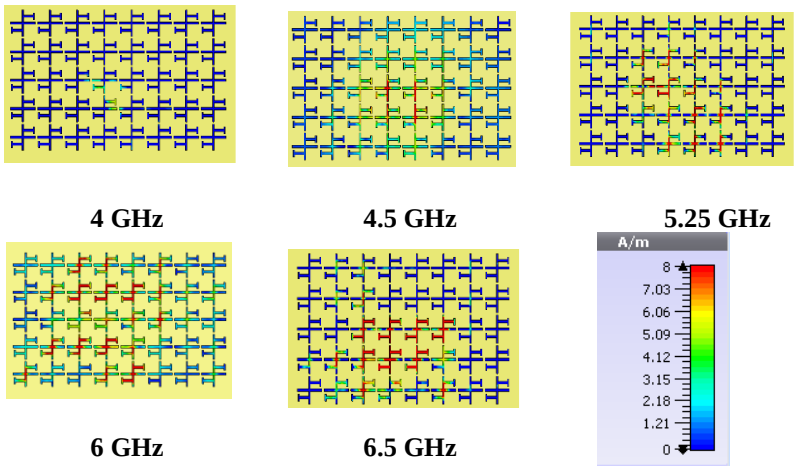

Figure 3.29: Simulated surface current distribution on the MCS AMC reflector at 4 , 4.5 , 5.25, 6, 6.5 GHz.

The surface current distributions on the MCS AMC reflector is depicted in Figure 3.29, at frequencies of 4 GHz, 4.5 GHz, 5.25 GHz, 6 GHz, and 6.5 GHz. It can obviously seen that the currents have been decreased. This reduction can be explained by the smaller surface area of the AMC reflector achieved by MCS cells, primarily strip structures. As a result, the circulation of surface currents is reduced, leading to a notable improvement in gain, particularly at 6.5 GHz (by almost 6.65 dB). The MCS AMC reflector demonstrates the desired performance characteristics, stable gain over a broad frequency band when compared to other AMC reflectors, fulfilling our specifications as shown in Table 3.7. In the next section a parametric study will be carried out to investigate the impact of different dimension on the antenna performances like: air thickness layer, number of the AMC unit cells, and the shape of the bowtie antenna edges.

3.2.5 Key design parameter investigations

a Air layer thickness

The influence of the air layer thickness (H_{air}) on the reflection coefficient and the broadside gain stability of the proposed configuration is displayed in Figure 3.30. The study focuses on varying the air layer thickness within the range of 1 to 3 mm.

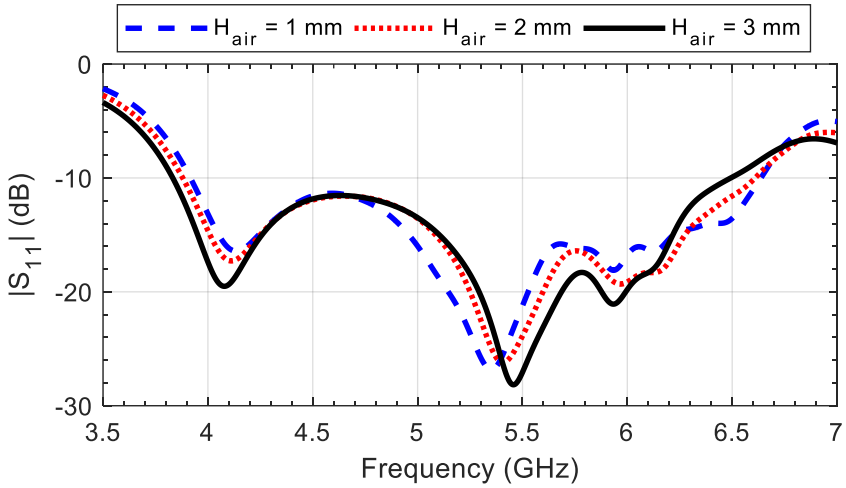

(a)

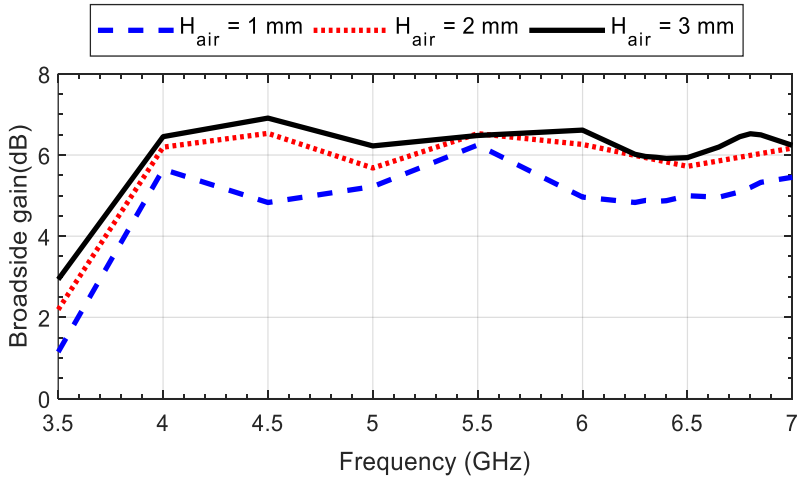

(b)

Figure 3.30: Effect of the air layer thickness on the performances of the bowtie antenna loaded with the selected MCS AMC reflector, (a) Reflection coefficient, (b) Broadside gain.

It can be noted from Figure 3.30(a), that the effect of H_{air} on the antenna impedance matching is less significant when compared to its effect on the broadside gain stability. As illustrated in Figure 3.30(b), a high gain variation of more than 1 dB is observed when H_{air} = 1 mm and H_{air} = 3 mm. In contrast ,when H_{air} is set to 2 mm, the gain remains relatively stable, with a variation of only 0.85 dB. This occurs across a wide relative bandwidth of 50% (3.94-6.61 GHz). By selecting H_{air} = 2 mm, the antenna demonstrates consistent and stable performance in terms of broadside gain, with minimal variation, making it an ideal choice for gain stability.

b AMC unit cell numbers

A parametric study is carried out in order to investigate the effect of the number of AMC unit cells on the reflection coefficient and the broadside gain, as shown in Figure 3.31.

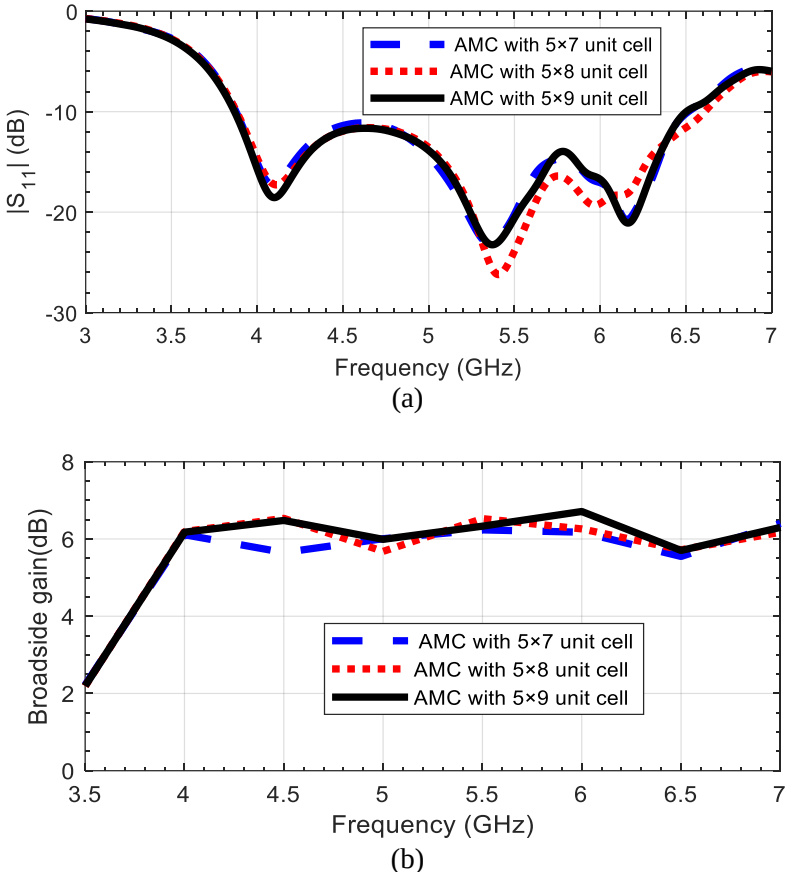

Figure 3.31: Evaluated antenna performances for different AMC unit cell numbers, (a) Reflection coefficient, (b) Broadside gain.

It is worth pointing out that no unit cell is inserted behind the balun to avoid deteriorating the wideband performance. Therefore, 5×7, 5×8, and 5×9 AMC unit cell arrangements are used instead of the 8×8 AMC unit cell arrangement. It can be observed that the impedance matching of the antenna is less sensitive to changes when the number of unit cells increases along the x-axis, whereas variations in gain stability are more significantly impacted. In particular, for the 5×7 and 5×9 AMC unit cell arrangements, the antenna's gain remains relatively stable with a gain variation of 1 dB. Conversely, the 5×8 AMC unit cell arrangement demonstrates superior stability with only a 0.85 dB gain variation, indicating a more consistent performance.
Finally, the 5×8 AMC unit cell arrangement emerges as the optimal tradeoff between input impedance bandwidth (50%) and gain stability, signifying its suitability as the preferred arrangement for the proposed antenna design.

c Bowtie antenna bending edges

When a traditional bowtie antenna (Triangular bowtie antenna) (with $X_{Rad} = 0$ mm) is positioned over an AMC reflector as it is depicted in Figure 3.32(a), it leads to a degradation in overall performance in terms of impedance matching and gain stability. To address this issue, a slight modification is proposed in Figure 3.32(b), by bending the edges of the two triangles of the bowtie antenna, this parameter, known as X_{Rad} .

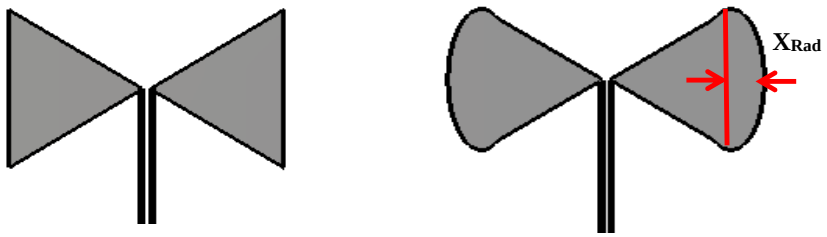

Figure 3.32: Edges forms of the bowtie antenna, (a) Triangular bowtie antenna, (b) Bended-edges bowtie antenna.

A comparison between the conventional bowtie antenna and this modified version is presented in Figure 3.33. It can be observed that, for $X_{Rad} = 3.5$ mm, the impedance bandwidth improves by 5%, and the variation in broadside gain decreases from 1.62 dB to 0.85 dB.

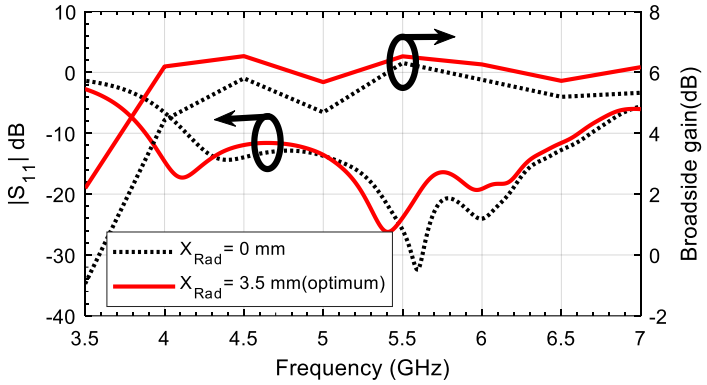

Figure 3.33: Effect of bowtie antenna bending edges on its reflection coefficient and broadside gain.

3.2.6 Measurement results and discussions

The bowtie antenna, with the proposed AMC reflector (see Figure 3.34 and Figure 3.35), has been manufactured and assembled as illustrated in Figure 3.36. The reflection coefficient has been measured using an Agilent N5224 vector network analyzer and presented in Figure 3.38(a). The measured impedance bandwidth ($| S_{11} | \leq -10$ dB), covers a range of frequencies, extending from 3.9 GHz to 6.61 GHz, constituting a relative impedance bandwidth of 50%. The simulated and measured results shows a good agreement. It is worth noting that a minor increase is observed in the higher frequency from 6.25 to 6.5 GHz, This slight discrepancy is attributed to fabrication inaccuracies during the manufacturing process.

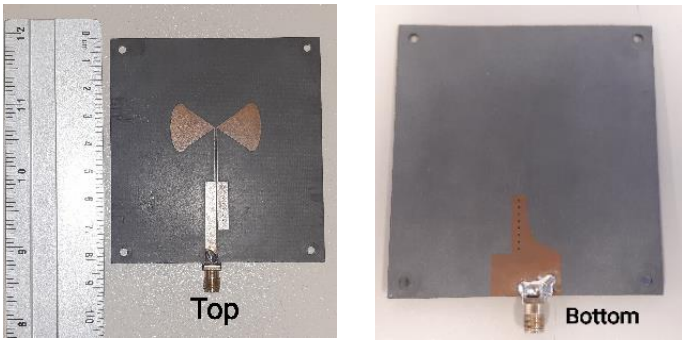

(a) (b)

Figure 3.34: The fabricated bowtie antenna, (a) Top view, (b) Bottom view.

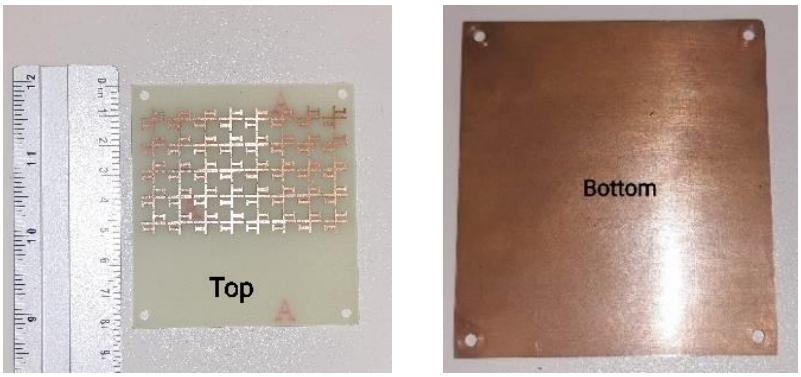

(a) (b)

Figure 3.35: The fabricated MCS AMC reflector, (a) Top view, (b) Bottom view.

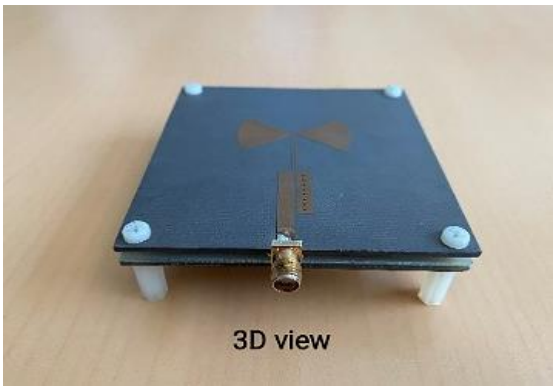

Figure 3.36: The fabricated assembly.

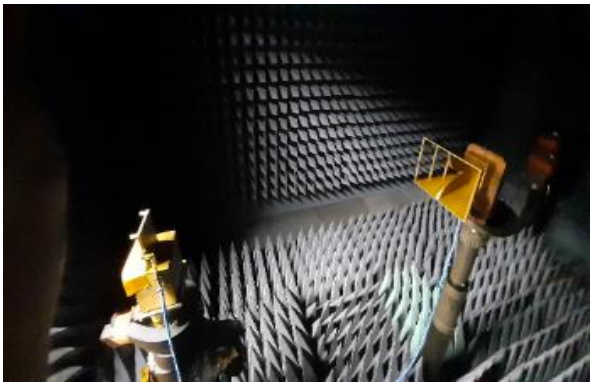

Figure 3.37: The measurement setup in anchoic chamber.

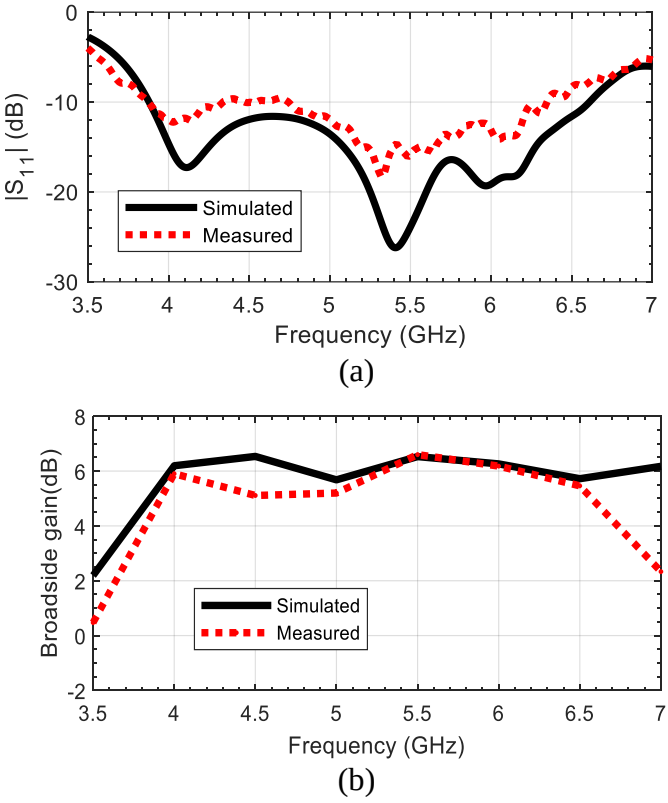

Figure 3.38: Simulated and measured antenna performances, (a) Reflection coefficient, (b) Broadside gain.

The radiation pattern measurements of the fabricated prototype antenna, loaded with MCS AMC reflectors were carried out in a standard anechoic chamber in LCIS laboratory in France, as it is shown in Figure 3.37. The dimensions of the anechoic chamber are $(3 \times 4 \times 2.5)m^3$. Figure 3.38(b), illustrates the simulated and measured broadside gain of the fabricated antenna over the proposed AMC reflector. The measured gain closely matches the simulated results. The gain is quasi stable over a wide impedance bandwidth (3.9–6.5 GHz). The observed gain variation is approximately 1.5 dB, slightly exceeding 0.85 dB gain variations predicted by the simulation. A small difference is noticed at 4.5 GHz, where the measured broadside gain decreases steeply from 6.61 to 5.10 dB (about 1.5 dB) which is probably due to the measurement errors. It's important to highlight that the radiation pattern measurements were conducted using a 10° theta step, consequently, the realized gain could not be correctly measured at this frequency. A comparison between simulated and measured radiation patterns of the fabricated prototypes is illustrated in Figure 3.39.

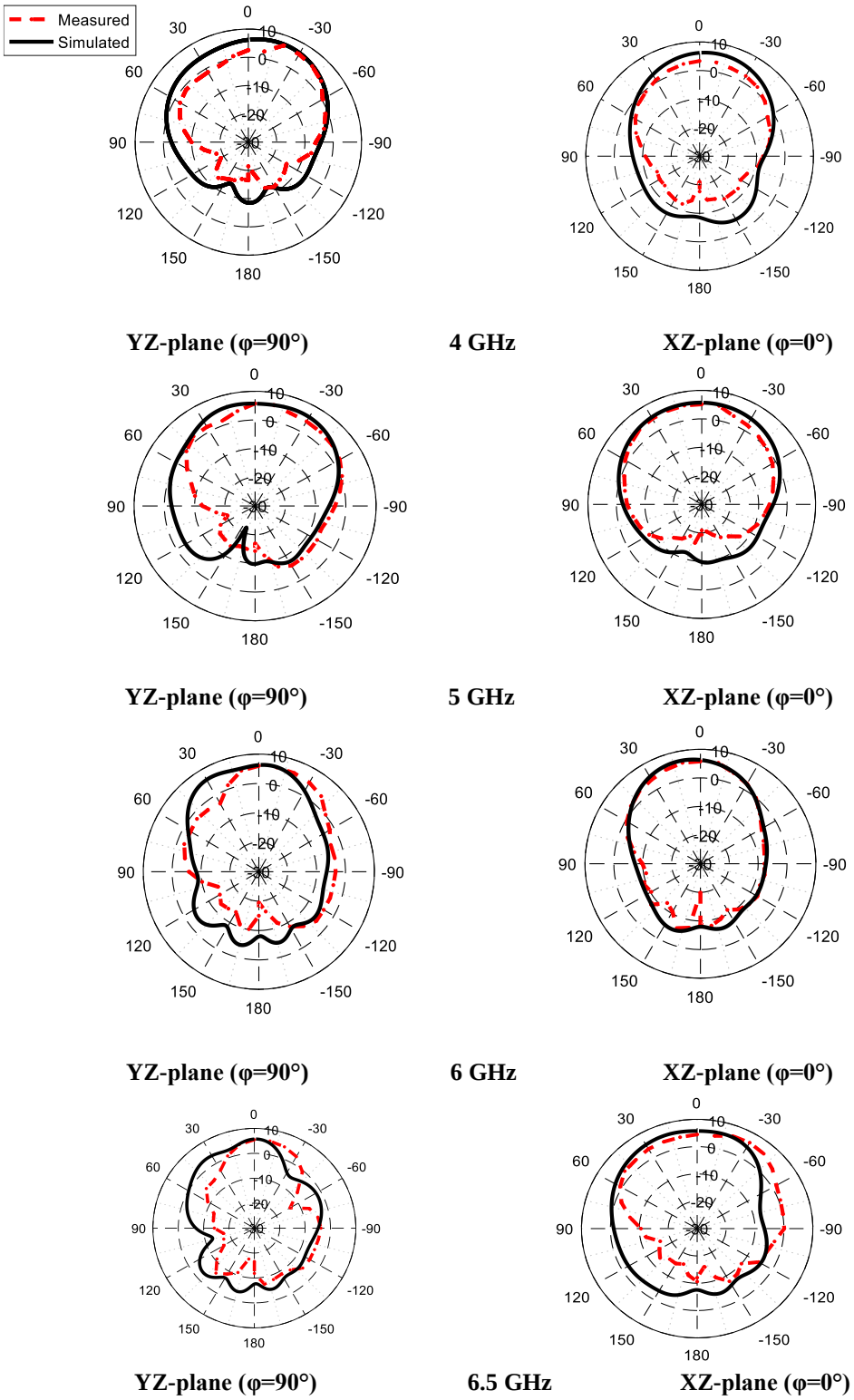

Figure 3.39: Simulated and measured radiation patterns (in gain) of the proposed antenna over the MCS AMC reflector.

The measurements are performed in both the E and H planes at the frequencies of 4, 5, 6, and 6.5 GHz. It is quite visible that, there is a strong agreement between the simulation and the measurement results. The fabricated structure back by the proposed AMC reflector shows unidirectional radiation pattern with a stable gain variation through the whole band of interest. The measured maximum realized gains are 5.9 dB, 5.19 dB, 6.18 dB, and 5.46 dB at 4 GHz, 5 GHz, 6 GHz and 6.5 GHz, respectively. Finally, the compact wideband bowtie antenna designed over the MCS AMC reflector is compared to other recently published antenna structures in the literature (presented in chapter 2). This comparison is summarized in Table 3.8, considers various criteria including structure thickness, relative frequency bandwidth, maximum gain, and gain variation.

Table 3.8: Comparison between the proposed antenna and other similar reported works

Reference	Thickness (λ_L)	Relative bandwidth (%)	Max gain (dB)	Gain variation(dB)
[65]	0.14	16.7	6.35	2
[66]	0.080	40	11	2
[67]	0.050	36.7	6.80	2.58
[71]	0.077	46	7.90	3
[72]	0.070	44	6	2
[73]	0.070	39	6	2
[74]	0.10	54	8.5	0.85
[76]	0.11	30	9	1.5
The proposed antenna over the MCS AMC reflector	0.084	50	6.52	0.85

The proposed antenna backed by the MCS AMC reflector demonstrates highly attractive characteristics. It offers an extensive relative bandwidth of 50% while maintaining an exceptionally low gain variation of only 0.85 dB. Although the structure presented in [74], exhibits relatively similar performance in terms of bandwidth and gain variation, it remains thicker when compared to the proposed antenna configuration. Additionally it becomes evident that the antenna with the MCS AMC reflector exhibits a marginally more stable gain over a wide impedance bandwidth of 50% compared to other proposed work in the literature. Consequently, the presented antenna emerges as a competitive candidate for C-band applications.

3.3 Application II: Low profile UHF-RFID reader antenna with high front-to-back ratio

The probe-fed U-slot patch antenna of size 200 × 200 × 30 mm^3, is shown in Figure 3.40, while its dimensions are given in Table 3.9. The radiating element and the ground plane are printed separately on two FR4 substrates, each with a thickness of 1.6 mm, a relative permittivity of 4.4 and loss tangent of 0.025. A 26.8 mm thick air layer is inserted between the two substrates in order to improve its impedance bandwidth (covering the full UHF-RFID band) while four small plastic supports are used to maintain the required air layer thickness. The U-slot patch antenna is fed by coaxial probe, which is extended from the center of the 200 × 200 mm^2 ground plane to the center of the U-slot patch antenna. The main specifications of this application are given in Table 3.10. The proposed antenna has been manufactured [101], as shown in Figure 3.41(a) and its reflection coefficient measurement is plotted in Figure 3.41(b). The probe-fed U-slot patch antenna exhibits a measured input impedance bandwidth ($|S_{11}| \leq$ -10 dB) of 182 MHz, ranging from 794 to 976 MHz, corresponding to a relative bandwidth of approximately 20.5%. However, the introduction of a 26.8 mm air layer between the antenna and its ground plane, results in a thick structure.

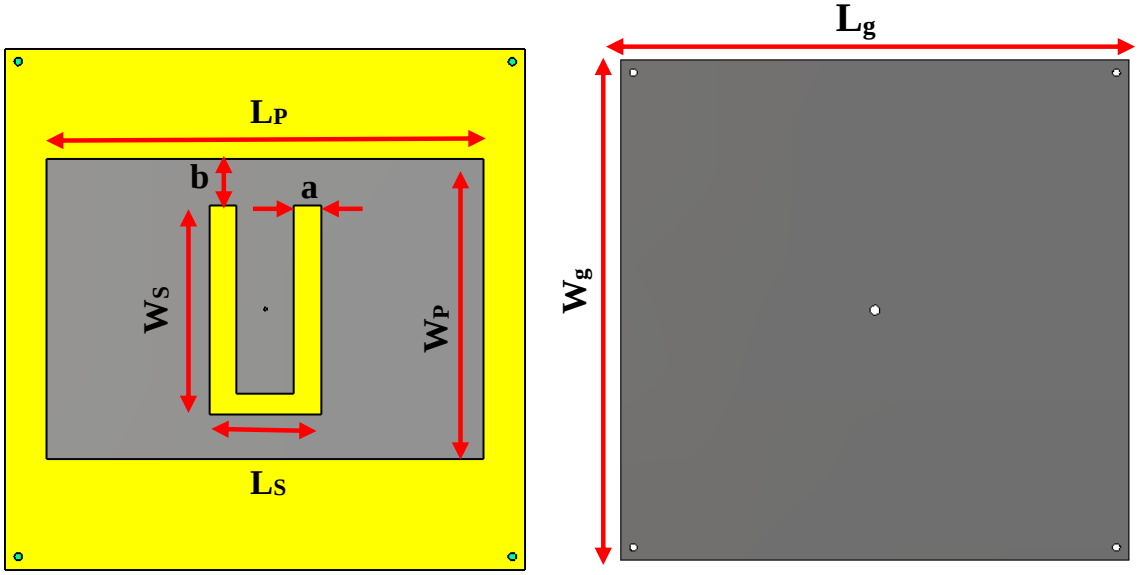

Figure 3.40: Probe fed U-slot patch antenna geometry, (a) Top view, (b) Bottom view.

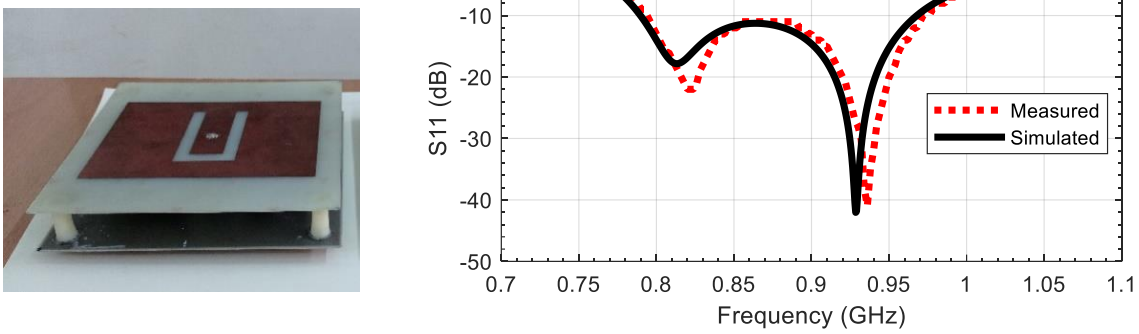

(a) (b)

Figure 3.41: The probe-fed U-slot patch antenna, (a) The fabricated prototype [101], (b) Measured reflection coefficient.

Table 3.9: Dimensions of the probe-fed U-slot patch antenna.

Parameter	L_g	W_g	L_p	W_p	L_S	W_s	a	b
Value (mm)	200	200	120	164	80	45	10	17.9

Table 3.10: Specifications of the proposed work.

Performances	Specifications
Frequencey band	(860-960 MHz) for RFID antenna Reader
Gain	$>$ 5 dB
Radiation pattern	Unidirectional
F/B	$>$ 15 dB

In addition, in this type of application, it is worth achieving a high front-to-back ratio (F/B). To address this drawbacks, a slotted AMC reflector is proposed, aiming to reduce the antenna thickness and improve its F/B ratio ($>$ 20 dB).

3.3.1 The probe-fed U-slot patch antenna over the slotted AMC reflector

The suggested AMC geometry is illustrated in Figure 3.42(a). It is designed based on a full square patch slotted by a square metal pad with four connecting branches [102]. The proposed unit cell is printed FR4 substrate of 3.2 thickness,relative permittivity of 4.3 and a loss tangent of 0.025. The dimensions of the AMC unit cell are provided in Table 3.11. It is worth to note that, the main purpose of slotting the AMC surface is to increase the equivalent inductance. Thus, the resonance frequency reduces.
The simulated reflection phase response depicted in Figure 3.43, reveals that the in-phase reflection bandwidth(±90°) of the proposed slotted AMC unit cell design is ranging from 893 MHz to 920 MHz (highlighted in grey), with a resonance frequency occurring at 910 MHz. In response to the limitations presented in the previous section (thick structure with a moderate F/B ratio), we present an innovative solution incorporating an AMC reflector with the U-slot patch antenna, as it is shown in Figure 3.44. The overall antenna structure is consisted of two dielectric substrates, separated by an airgap layer of 10 mm, as depicted in Figure 3.44(a).

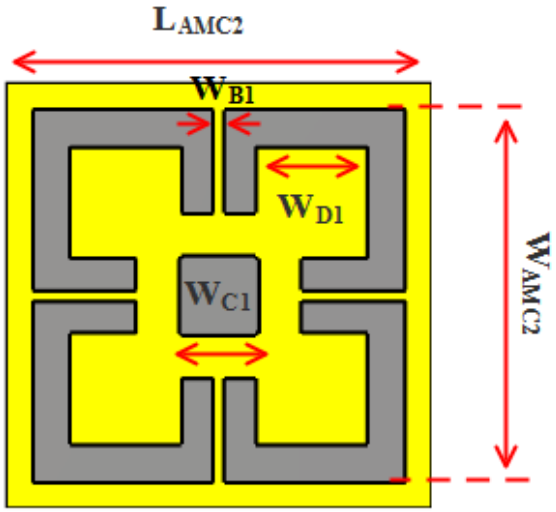

Figure 3.42: Slotted AMC unit cell geometry.

Table 3.11: Dimensions of the slotted AMC unit cell.

Parameter	L_{AMC2}	W_{AMC2}	W_{B1}	W_{C1}	W_{D1}
Value (mm)	60	50	1.327	8.85	12.39

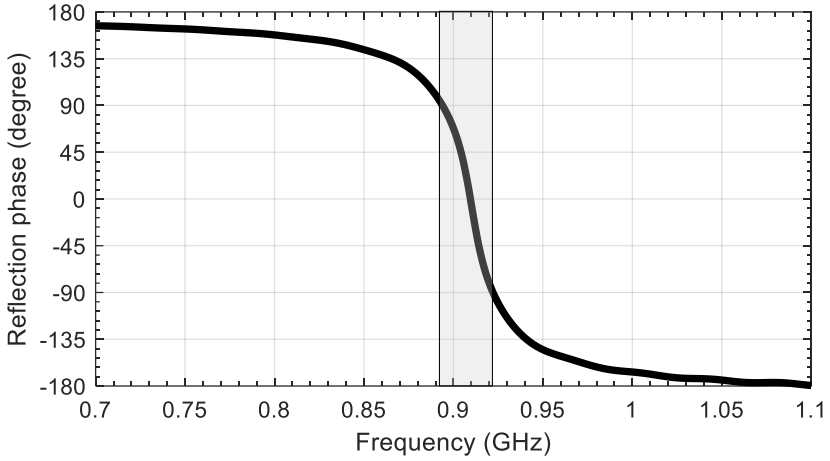

Figure 3.43: Simulated reflection phase response of the proposed AMC unit cell.

The upper dielectric layer consists of the U-slot patch antenna with dimensions of 200×200 mm^2, while the bottom layer compromise of a 2×2 arrangement of slotted AMC unit cells with total dimensions of 200× 200 mm^2, as shown in Figure 3.44(b). The air layer is sustained by four plastic bolts with nuts, resulting in a total thickness of 16.4 mm ($0.049\lambda_0$, where λ_0 is the wavelength at the center frequency 910 MHz). As previously mentioned, the antenna is also fed by coaxial probe, but this time the coaxial probe is extended from the center of AMC ground plane to the center of the U-slot patch antenna. It is crucial to highlight that the close proximity between the AMC surfaces and the radiating antenna engenders a robust coupling between them. Consequently, the AMC surface are integral component of the radiating antenna system. Therefore, the optimization of both elements becomes imperative to attain the most effective performance enhancements. The ultimate optimized parameters for the proposed U-slot antenna over the slotted AMC reflector are listed in Table 3.12.

Table 3.12: Dimensions of the optimised probe-fed U-slot patch antenna over the slotted AMC reflector.

Parameter	L_g	W_g	L_p	W_p	L_S	W_s	b	a
Value (mm)	200	200	115	164.7	80	43	10.6	7.94
Parameter	W_{AMC2}	W_{B1}	W_{C1}	W_{D1}	H_1	H_2	H_{air}	$Gap1$
Value (mm)	70	2.5	15	21	1.6	4.8	10	5

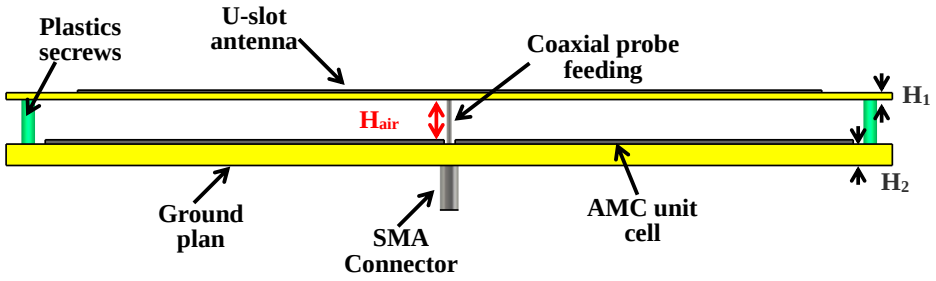

(a)

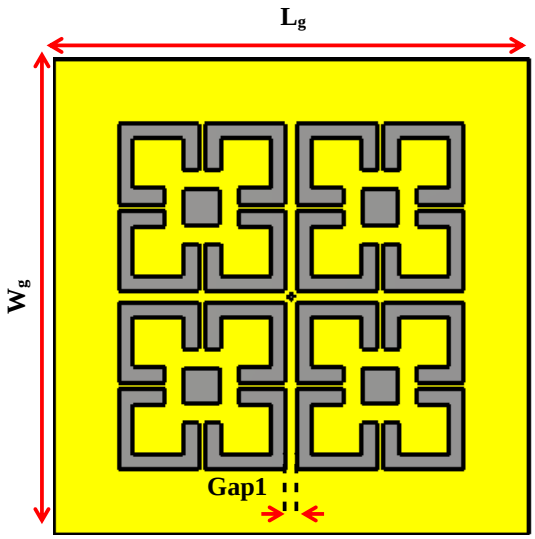

(b)

Figure 3.44: The proposed antenna over the slotted AMC reflector, (a) Side view, (b) AMC reflector top view.

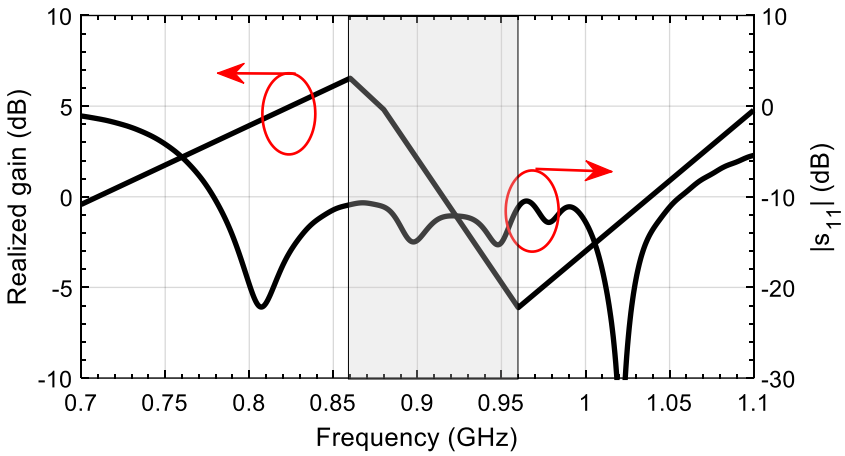

Figure 3.45: Simulated characteristics (reflection coefficient and gain) of the proposed U-slot patch antenna over the slotted AMC reflector.

Figure 3.45 illustrates the simulated performances (reflection coefficient and realized gain) of the U-slot patch antenna over the slotted AMC reflector. It can be observed that, it can cover the full UHF-RFID band, demonstrating a wide impedance bandwidth ranging from 0.779 GHz to 1.05 GHz but with an unstable gain varies between -6.11 and 6.53 dB. In addition, the radiation pattern is also plotted in E and H planes at 860 MHz, 910 MHz and 960 MHz, as it is illustrated in Figure 3.46. The U-slot patch antenna over the slotted AMC reflector exhibits a unidirectional radiation pattern with maximum realized gains of 6.56, 0.147 and - 5 dB at 860, 910 and 960 MHz, respectively.

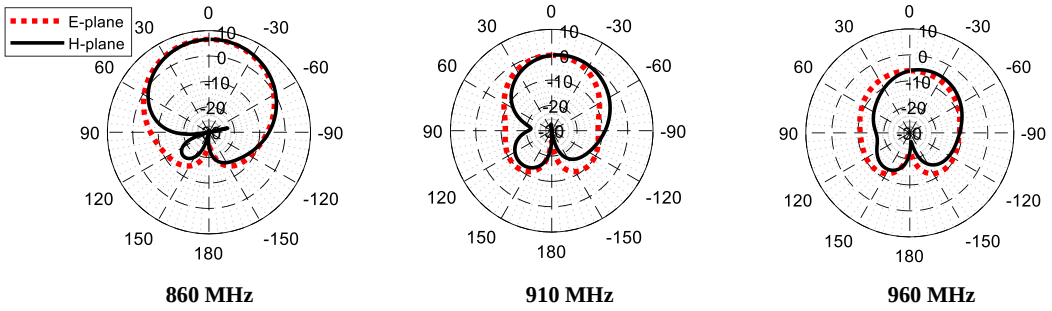

Figure 3.46: Simulated radiation pattern (in gain) of the U-slot patch antenna over the slotted AMC reflector.

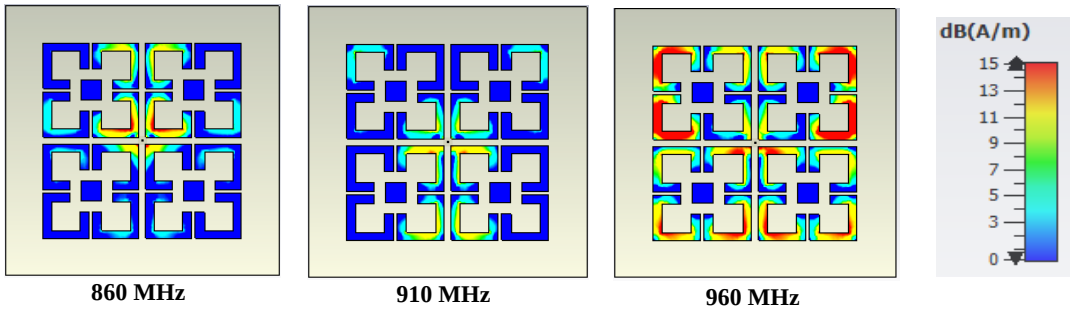

Figure 3.47: Simulated current distribution on the slotted AMC reflector.

In order to explain the gain degradation across the full UHF-RFID band, the surface current distribution is displayed in Figure 3.47 at the three distinct frequencies: 860 MHz, 910 MHz and 960 MHz. It can be observed that there is strong current circulations at 960 MHz, which explains the gain degradation at this frequency. It is worth mentioning that the surface current distribution on the AMC surfaces serves to evaluate performance degradation, including effects on realized gain and radiation pattern.

3.3.2 The probe-fed U-slot patch antenna over the LSP AMC reflector

Based on the above detailed analysis in the previous section, it can be concluded that, while the frequency band specification is met, the gain is not within the desired range. Therefore, another slotted AMC unit cell design is proposed.
The proposed LSP (Ladder Slotted Patch) AMC geometry is illustrated in Figure 3.48. It is designed based on a full square patch slotted by an original distinctive design of ladder shape, consisted of of three parallel longitudinal strips. The right and left longitudinal strips are identical in both length and width, while the middle strip varies in length while preserving the same width. These three longitudinal strips are arranged perpendicularly to three other identical parallel transverse strips, collectively forming a ladder-slot configuration. The LSP AMC unit cell is printed on 3.2 mm-thick FR4 substrate with a relative permittivity of 4.3 and a loss tangent of 0.025. Its dimensions are provided in Table 3.13. The reflection phase of the proposed LSP AMC unit cell is plotted in Figure 3.49. It can be seen that the in-phase reflection bandwidth (±90°) of the designed LSP AMC unit cell is ranging from 890 MHz to 924 MHz (grey-highlighted area) with a resonance frequency of 910 MHz.

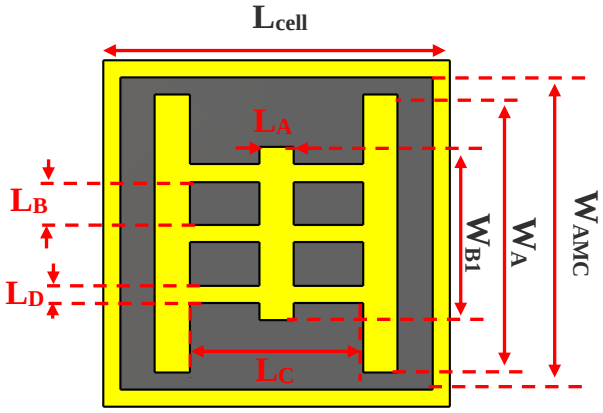

Figure 3.48: LSP AMC geometry.

Table 3.13: Dimensions of the LSP AMC unit cell.

Parameter	L_{cell}	W_{AMC}	W_A	W_{B1}	L_B	L_D	L_A	L_C
Value (mm)	67.5	57.5	49	32	10	2.5	8	35

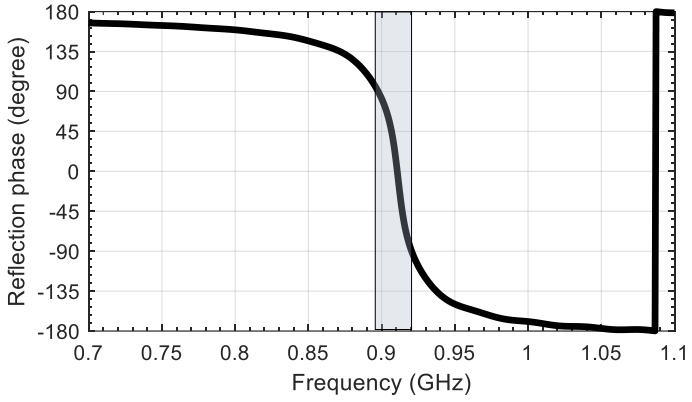

Figure 3.49: Reflection phase response of the LSP AMC unit cell.

Now, the proposed U-slot patch antenna is loaded with the Ladder Slotted Patch (LSP) AMC reflector, as depicted in Figure 3.50(a). The AMC reflector comprises a 2x2 unit cells, as shown in Figure 3.50(b). It is situated at a 10 mm air gap from the U-slot patch antenna structure. As a result, the overall profile thickness is 16.4 mm ($0.049\lambda_0$). The final dimensions of the optimized configuration (antenna + LSP AMC reflector) are summarized in Table 3.14. The reflection coefficient and the realized gain of the proposed U-slot patch antenna over the LSP AMC reflector is depicted in Figure 3.51. The results reveal a notable impedance bandwidth, extending from 846 MHz to 1075 MHz, corresponding to a relative impedance bandwidth of 24%. This range effectively covers the entire UHF-RFID band (860-960 MHz). Additionally, the antenna exhibits a high gain, varying between 6 and 7.67 dB over the UHF-RFID band (860-960 MHz).The gain is enhanced by 6.67 and 12 dB at 910, 960 MHz, respectively, compared to the U-slot patch antenna loaded with the previous slotted AMC reflector.

Table 3.14: Dimensions of the optimised U-slot patch antenna over the slotted AMC reflector

Parameter	L_g	W_g	L_p	W_p	L_S	W_1	b	a	L_{cell}	W_{AMC}
Value (mm)	200	200	115	164.7	80	43	10.6	7.94	95	90
Parameter	W_A	W_{B1}	L_A	L_C	L_B	L_D	H_1	H_2	H_{air}	Gap
Value (mm)	74	50	10	55	10	1.5	1.6	4.8	10	10

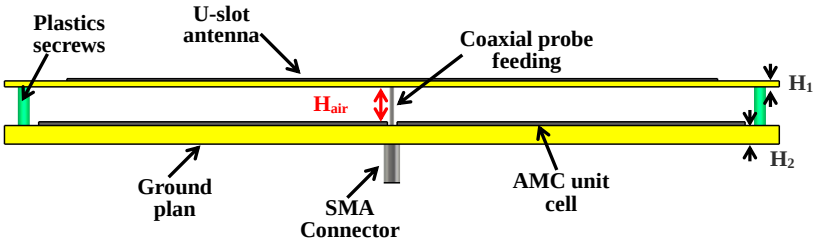

(a)

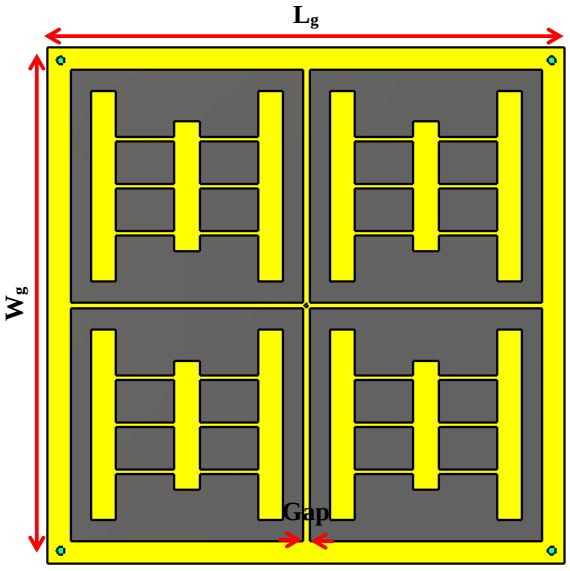

(b)

Figure 3.50: The probe-fed U-slot patch antenna over the LSP AMC reflector, (a) Side view, (b) AMC reflector top view.

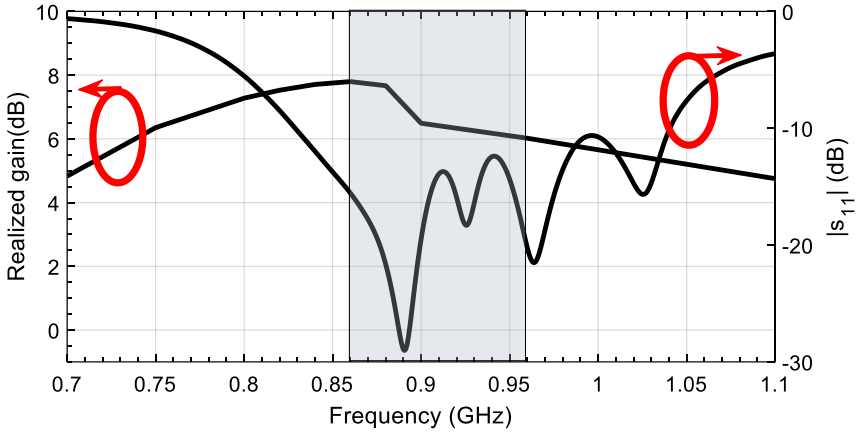

Figure 3.51: Simulated reflection coefficient and gain of the proposed U-slot patch antenna over the LSP AMC reflector.

The radiation pattern of the proposed U-slot patch antenna over the Ladder Slotted Patch (LSP) AMC reflector is plotted in the E and H planes at the three distinct frequencies of 860 MHz, 910 MHz, and 960 MHz, as depicted in Figure 3.52. The proposed radiating configuration exhibits a unidirectional radiation pattern, with maximum realized gains of 7.73 dB, 6.37 dB, and 6 dB at 860 MHz, 910 MHz, and 960 MHz, respectively.

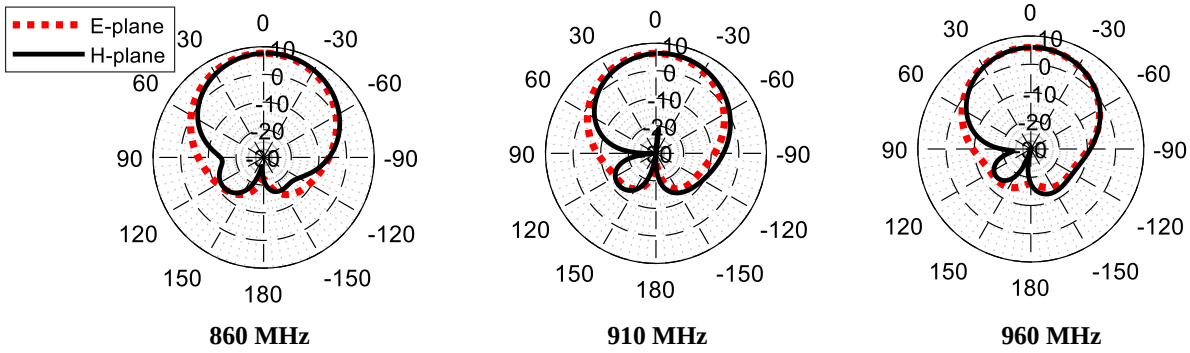

Figure 3.52: Simulated radiation pattern (in gain) of the proposed U-slot patch antenna over the LSP AMC reflector.

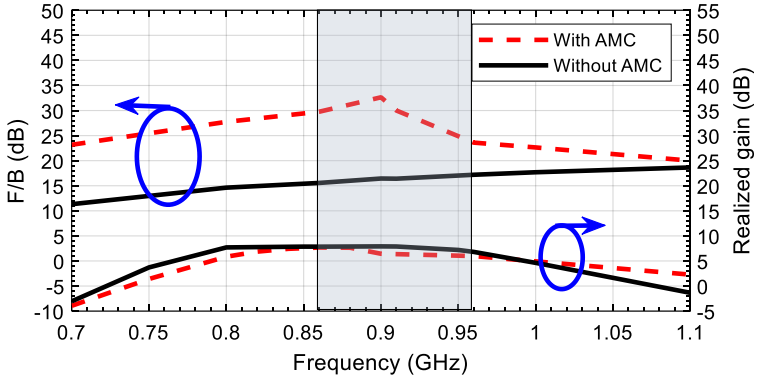

Figure 3.53: Comparison between the gain and F/B ratio of the proposed U-slot patch antenna with/without AMC reflector.

The variation of the F/B ratio and the realized gain versus frequency of the designed U-slot patch antenna with /without the AMC reflector is depicted in Figure 3.53. It can be noted that the F/B ratio is increased after the incorporation of the AMC reflector, varying between 23.6 and 32 dB across the full UHF-RFID band, whereas it ranges between 15.5 and 18 dB for the probe-fed U-slot patch antenna without the AMC

reflector. Although the gain experiences a slight decrease of 1 dB across the full UHF-RFID band (varying between 6 and 7.67 dB) compared to the design without the AMC reflector, it still meet our specifications (more than 5 dB). Moreover, the antenna demonstrates a significantly reduced air layer thickness of only 10 mm, which is 2 times lower than that observed without the AMC reflector (26.8 mm), all while maintaining a high F/B ratio. This remarkable performances demonstrate the ability of the AMC surface not only in reducing the profile height but also ineffectively suppressing the backward radiation when used as the antenna reflector.

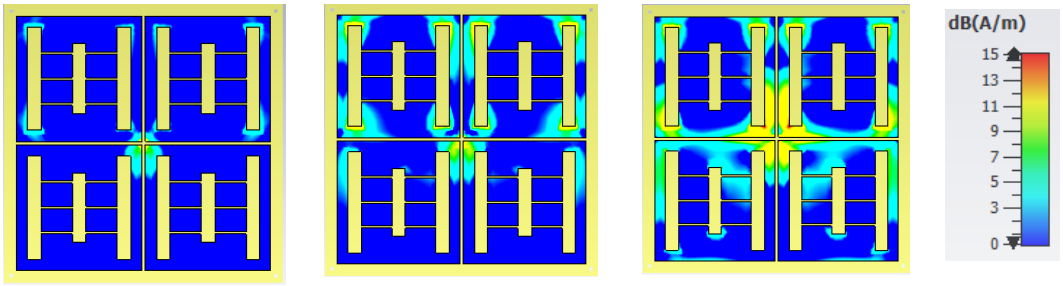

Figure 3.54: Current distribution on the LSP AMC reflector

The surfaces current distributions on the LSP AMC surface at three frequencies: 860 MHz, 910 MHz, and 960 MHz. It can be observed that there is poor current distribution on the proposed AMC reflector compared to that observed in the case of the first slotted AMC reflector. Except, at 960 MHz, there is a slight current distribution. This limited surface current circulation leads to the gain enhancement, especially at 960 MHz. It is worth to note that the limited current circulation on the AMC reflector serves to prevent performance degradation (radiation), thereby explaining its ability to enhance the F/B ratio.

Upon analysis, our specifications are met by using the LSP AMC reflector, which reduces the overall thickness by 45% (from 30 mm to 16.4 mm) compared to the initial design design (without AMC) while maintaining a high gain and enhanced F/B ratio performances of more than 24 dB across the entire UHF-RFID band. Consequently, this configuration is selected as the optimal choice for this study.

In the next section, a parametric study is conducted to explore the impact of key design parameters on the antenna's performances.

3.3.3 Key design parameter investigations

a Air layer thickness

A parametric study is conducted to demonstrate the influence of the air layer thickness (H_{air}) on the antenna's performances. Figure 3.55, depicts the reflection coefficient, realized gain and F/B ratio of the proposed U-slot patch antenna backed by LSP AMC reflector.

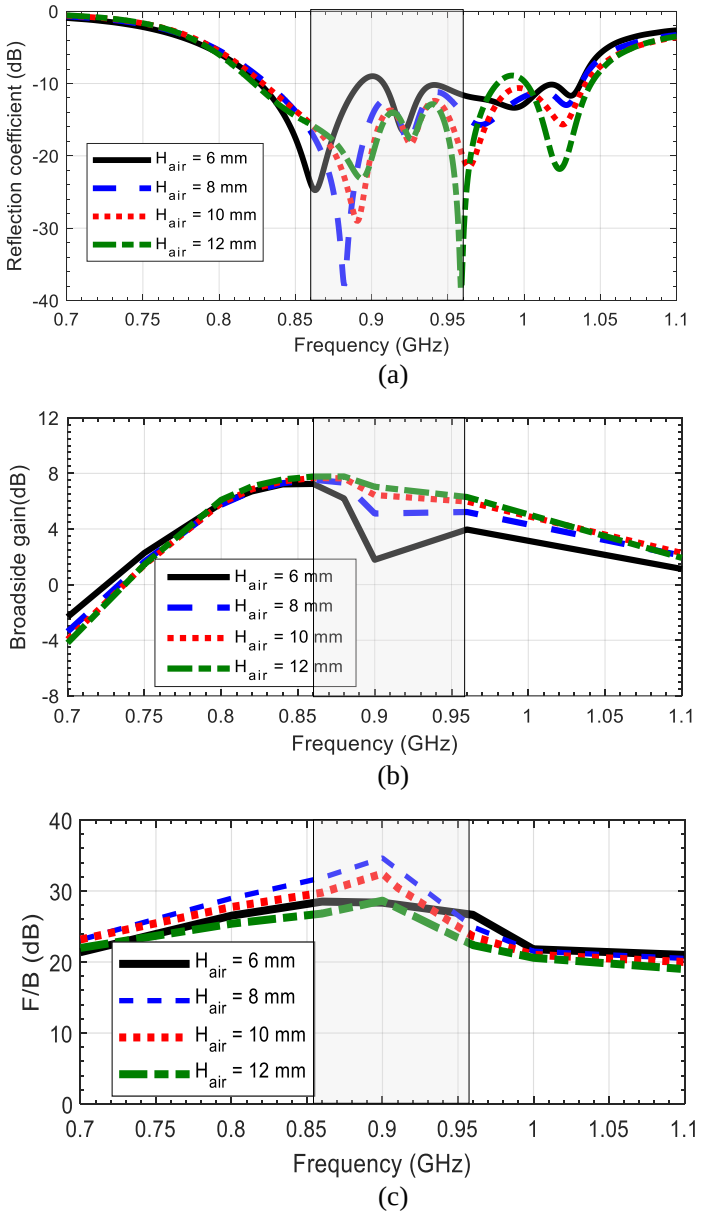

Figure 3.55: The air layer thickness effects on the antenna's performances, (a) Reflection coefficient, (b) Realized gain, (c) F/B ratio.

By varying H_{air} within the range of 8 to 12 mm, a notable degradation in impedance matching, particularly evident at the frequency 900 MHz when $H_{air} = 6$ mm.
This degradation resulted in dips in the realized gain reaching approximately 2 dB with a F/B ratio of 28 dB. However, for other cases, the antenna demonstrates favorable impedance matching within the UHF-RFID frequency band (860-960 MHz), as highlighted in the grey area, accompanied by high gain. Notably,the realized gain varies between 5.11-7.54 dB, 6-7.67 dB, and 6.29-7.76 dB, while the F/B ratio ranges between 24-34 dB, 23.6-32.46 dB, and 22-26.8 dB for $H_{air} = 8$ mm, $H_{air} = 10$ mm and $H_{air} = 12$ mm, respectively. Finally, an H_{air} of 10 mm is selected as an optimal tradeoff between impedance matching, gain, F/B ratio and structure thickness.

b AMC unit cell parameters

Another parametric study was conducted, as depicted in Figure 3.56, to examine the influence of unit cell geometry on antenna reflection coefficient and gain. Three key parameters, namely W_A, L_C, and L_B, were investigated, each exhibiting a significant impact on the antenna characteristics. The investigation focuses on the reflection coefficient and realized gain concerning the W_A parameter. However, for L_C and L_B, only the realized gain is examined, as these parameters do not show significant effect on the antenna impedance matching. Figure 3.56(a), illustrates the impact of the W_A parameter on the antenna characteristics. By varying the W_A parameter from 70 mm to 78 mm. This parameter has a significant influence on both gain and reflection coefficient. The Impedance matching tends to deteriorate for $W_A = 70$ mm and $W_A = 78$ mm. In contrast, good impedance matching is achieved for $W_A = 74$ mm, where the antenna exhibits a high gain exceeding 6 dB across a wide impedance matching range ,extending from 860 MHz to 960 MHz, covering the UHF-RFID band. Consequently, $W_A = 74$ mm is selected as a favorable compromise between the impedance matching and gain.
Additionally, Figure 3.56(b) illustrates the impact of the L_C parameter on the antenna gain. For $L_C = 50$ mm and $L_C = 60$ mm, a dip in the antenna gain of 5 dB and 2.55 dB is observed at 900 MHz and 960 MHz, respectively, within the UHF-RFID band. When $L_C = 55$ mm, a high gain ranging between 7.67 and 6 dB is achieved across the entire UHF-RFID band. Therefore, this parameter is chosen as optimal for achieving the best characteristics within the UHF-RFID band.

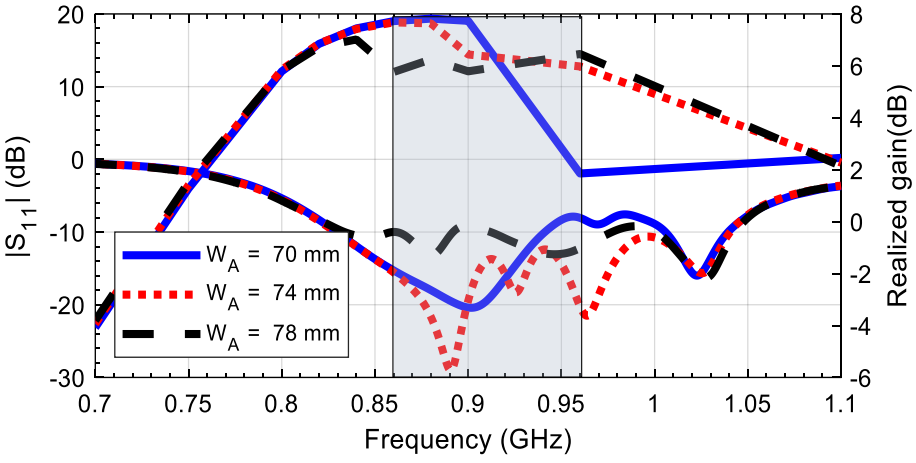

(a)

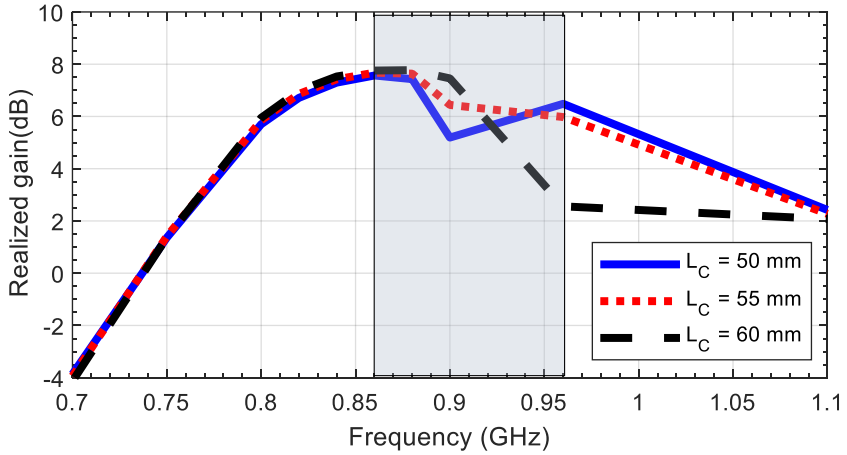

(b)

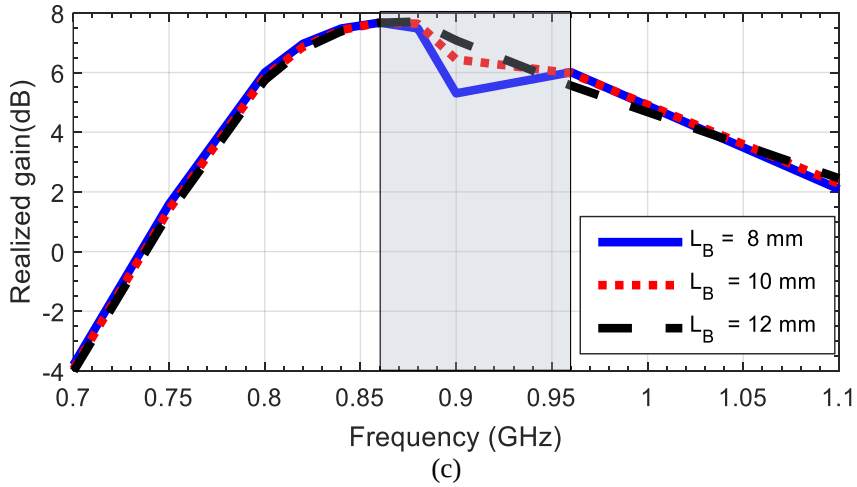

(c)

Figure 3.56: The impact of the AMC unit cell parameters on the antenna performances, (a) W_A parameter, (b) L_C parameter, (c) L_B parameter.

Further, the effect of the L_B parameter on the antenna gain is depicted in Figure 3.56(c). It is quite visible, that when $L_B = 8$ mm, the gain slightly drops to 5.3 dB at 900 MHz compared to the other cases which has 6.43 dB and 7 dB, respectively, at the same frequency. It can be noticed that ,for $L_B = 10$ mm and $L_B = 12$ mm, a high gain over the UHF-RFID band is achieved, However, $L_B = 10$ mm can achieve a notable gain of 6 dB at 960 MHz, in contrast to $L_B = 12$ mm, which exhibits 5.5 dB at the same frequency , therefore $L_B = 10$ mm is selected as an optimum parameter .
In summary, $W_A = 74$ mm, $L_C = 55$ mm, and $L_B = 10$ mm are chosen as the final optimal parameters of the AMC reflectors, to achieve the best characteristics across the full UHF-RFID band.

3.3.4 Prototype of the probe-fed U-slot patch antenna loaded with LSP AMC reflector.

The suggested U-slot patch antenna backed by the LSP AMC reflector has been manufactured, as depicted in Figure 3.57. To establish an air layer of 10 mm, four plastic screws are employed. These screws were strategically drilled into the corners of the two substrates, facilitating the assembly and stacking processes of the antenna prototype, as shown in Figure 3.57(c).

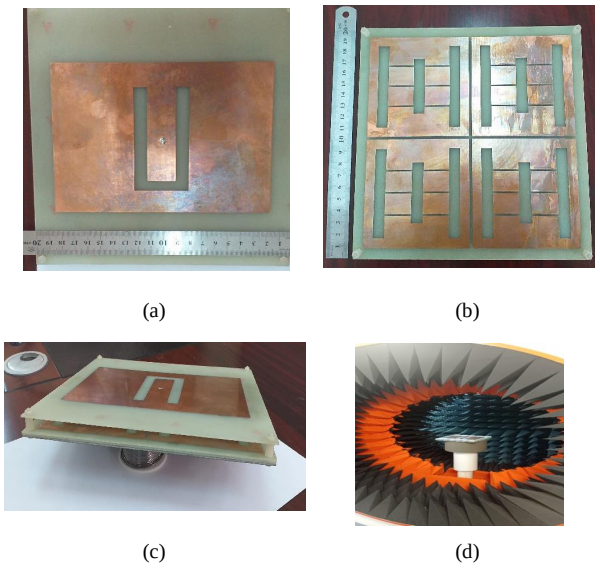

Figure 3.57: Photograph of the fabricated prototype, (a) The U-slot patch antenna, (b) The LSP AMC reflector, (c) Fabricated assembly, (d) Measurement set up in the StarLab anechoic chamber.

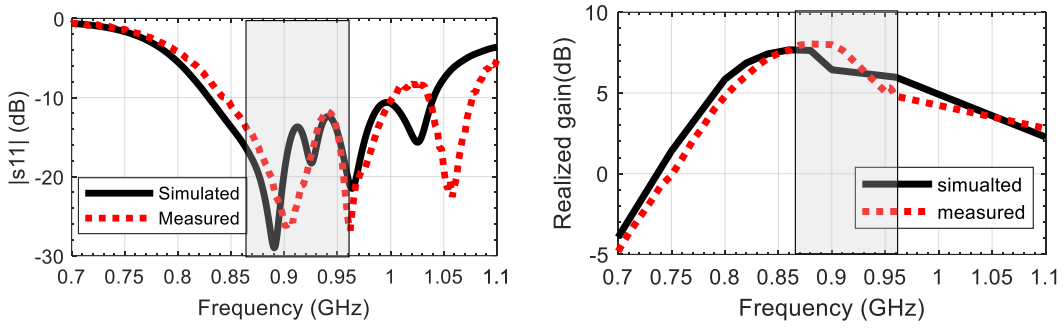

Figure 3.58: Measured antenna characteristics, (a) Reflection coefficient, (b) Realized gain.

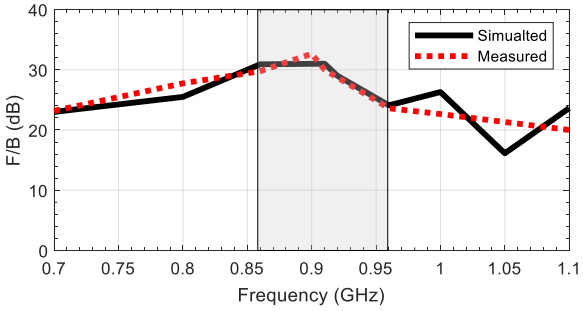

Figure 3.59: Simulated and measured F/B ratio.

The reflection coefficient of the proposed configuration was measured using Keysight Agilent PNA Network Analyzer N5222A. As depicted in Figure 3.58(a), a satisfactory coherence was observed between the simulated and tested data. A measured impedance bandwidth ($| S_{11} | \leq -10$ dB) of 24% was attained in the frequency range of 846 to 1075 MHz. However, a slight frequency shift is achieved between the simulated and measured data, particularly in the band of 1-1.05 GHz. This discrepancy may be attributed to manufacturing and measurement errors.

Figure 3.58(b) illustrates the simulated and measured realized gain of the proposed U-slot patch antenna over the AMC reflector. A notable coherence between the simulated and measured results is observed, with a slight deviation of approximately 1.2 dB observed at 960 MHz. This deviation is attributed to the antenna support, which was not accounted for during the simulation. The simulated and measured F/B ratio are also plotted as shown in Figure 3.59. Regarding backward radiation, the antenna achieves high F/B ratio of 30.9 dB, 31.3 dB, and 24.09 dB at the three considered

frequencies: 860 MHz, 910 MHz, and 960 MHz, respectively, affirming the efficacy of the AMC reflector in enhancing the F/B ratio. The proposed structure exhibits high measured gain and F/B ratio exceeding 5 dB, 24 dB across the entire RFID-UHF band (860-960 MHz). Furthermore, the radiation pattern measurements were conducted in the MVG StarLab system at the LCIS laboratory in France, as depicted in Figure 3.57(d).

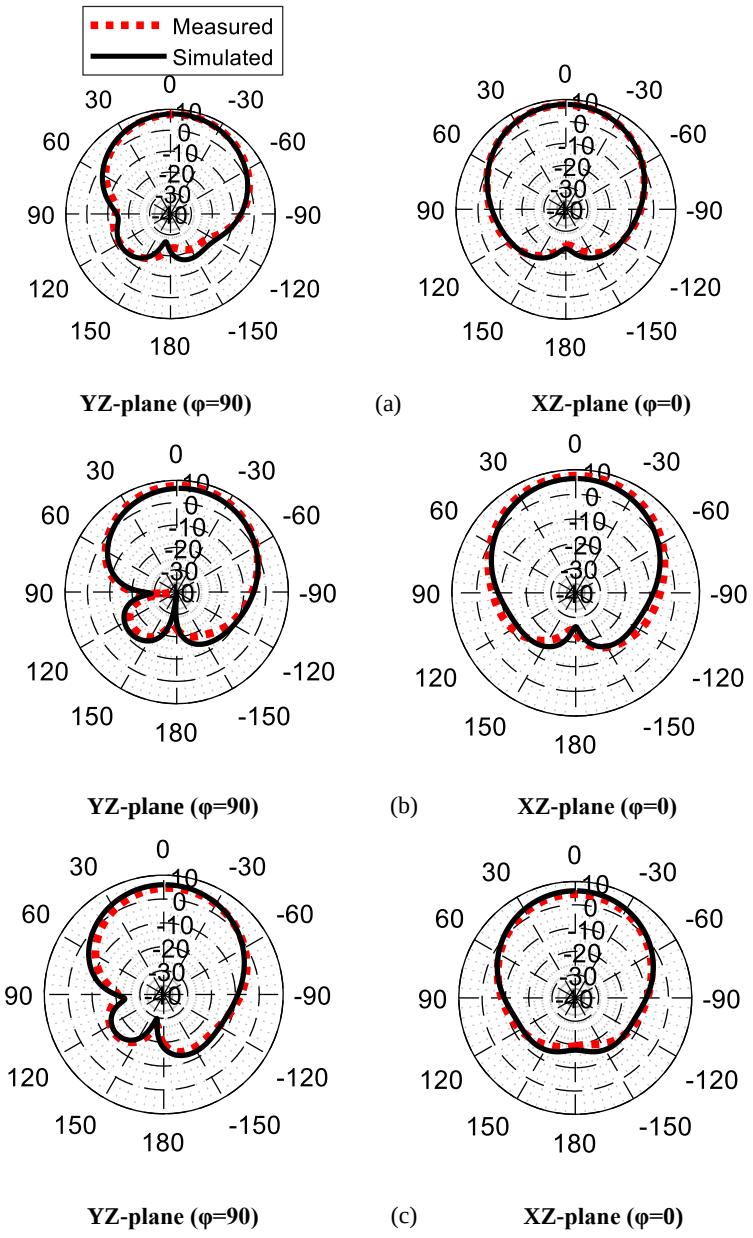

Figure 3.60: Simulated and measured radiation pattern (in gain) of the U-slot patch antenna over the LSP AMC reflector at, (a) 860 MHz, (b) 910 MHz, (c) 960 MHz.

The simulated and measured radiation patterns in the E-plane and H-plane are presented in Figure 3.60. The measured data agree well with the simulated data, with slight shifts in the E-plane observed at 960 MHz, attributed to the same reasons mentioned earlier. With the incorporation of the AMC reflector, the U-slot antenna demonstrates a stable directional radiation pattern, with a high measured gains of 7.65 dB, 7.66 dB, and 4.80 dB at 860 MHz, 910 MHz, and 960 MHz, respectively. Additionally, the antenna achieves minimized back lobe levels, resulting in a high F/B ratio of 30.9 dB, 31.3 dB, and 24.09 dB at the three central frequencies, respectively. Finally, a comparison between U-slot patch antenna with / without AMC is listed in the Table 3.15. As indicated in Figure 3.61, the proposed antenna with the AMC reflector has a reduced profile height of 16.4 mm (45% reduction) compared to that without AMC (30 mm) ,while it maintains high gain and F/B ratio across the full UHF-RFID band.

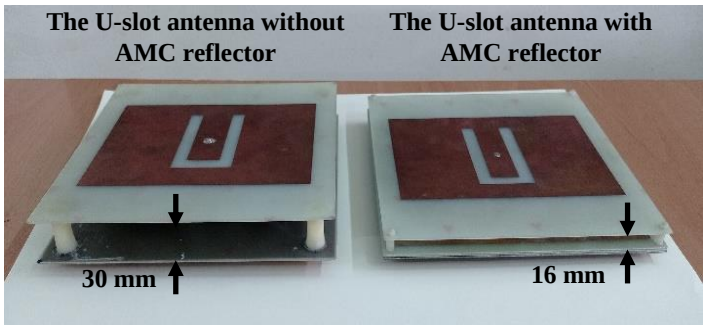

Figure 3.61: Comparison between the U-slot patch antenna without/with AMC reflector

Table 3.15: Comparison between the U-slot patch antenna with / without AMC

Performance	The U-slot patch antenna (Without AMC)	The U-slot patch antenna(With AMC)
Bandwidth ($\mid S_{11} \mid \leq -10$ dB)	[794 - 976] MHz 20.5%	846 - 1075] MHz 24%
Realized gain over [860-960] MHz	[6.80-7.88] dB	[6 -7.67] dB
Overall thickness (mm/ λ_0)	30 mm 0.091 λ_0	16.4 0.049 λ_0
F/B (dB)	15.5 dB $\leq$ F/B $\leq$ 18 dB	23.6 dB $\leq$ F/B $\leq$ 32 dB

The U-slot patch antenna over the proposed AMC reflector exhibits a realized gain between 6 and 7.67 dB with significant F/B ratio values varies between 23.6 and 32 dB across the entire UHF-RFID band, demonstrating the ability of the AMC surfaces to suppress the backward radiation when it use as the antenna reflector.
The proposed design offers the advantages of low profile, high gain and F/B ratio, making it is a competitive candidate for UHF- RFID antenna reader.

3.4 Conclusion

In this chapter, we have thoroughly examined the efficacy of AMC surfaces when employed as reflectors for wideband antennas, with a specific focus on their potential advantages in stabilizing gain, reducing antenna thickness and enhancing the F/B ratio. Our investigation has revealed that, despite the narrow in-phase bandwidth of AMC surface, we have successfully designed a wideband antenna with a wide impedance bandwidth, corresponding to 50% of the relative bandwidth. Moreover, by leveraging the unique properties of AMC, we have achieved stable antenna gain with a minimal variation of 0.85 over this wide bandwidth. This distinctive property can further be explored for reducing the antenna profile height and improving its F/B ratio. Through the strategic integration of AMC as a reflector, we have realized a substantial reduction in antenna thickness, achieving a compact design with a thickness of 16.4 mm. This represents a significant improvement compared to the previous structure without AMC, corresponding to a remarkable 45% reduction all while maintaining a high gain and F/B ratio. These findings underscore the effectiveness of the AMC reflector in not only stabilizing gain but also in achieving a more compact antenna profile and enhancing the F/B ratio.

Chapter 4

AMC reflectors-based multiband antennas

4.1 Introduction

The current chapter is dedicated to design multiband antennas based on multiband artificial magnetic conductors for two primary applications: miniaturization, reduction of backward radiation, and gain enhancement across multiple operating bands. Therefore, the antenna design will be presented, as well as the design of the AMC surfaces. Subsequently, the results of the antenna backed with AMC reflectors will be discussed and compared to other published works to demonstrate the effectiveness of the AMC reflector for the two applications.

4.2 Application I: Miniaturization of a multiband pyramidal Antenna using AMC reflector for satellite applications.

4.2.1 Initial multiband pyramidal Antenna design

The suggested multiband antenna configuration is depicted in Figure 4.1(a). It is composed of four monopoles arranged symmetrically around the vertical axis with angle of 45°. These monopoles are printed on Roger DiClad 880 dielectric substrates with a thickness of 0.760 mm, a relative permittivity of 2.17, and a loss tangent of 0.0009, constitute the side faces of the pyramidal structure. Each monopole in this configuration

is fed through 50 Ω SMA connector, with connections to the excitation point established via 50 Ω planar transmission line that is printed on the same dielectric substrate as the monopole antenna. Furthermore, as shown in Figure 4.1(b), a circular ground plane, featuring a circular perforation with a diameter of 66 mm, is strategically positioned at the base of the pyramidal structure. This perforation is designed to guarantee optimal impedance matching, as suggested in [103].

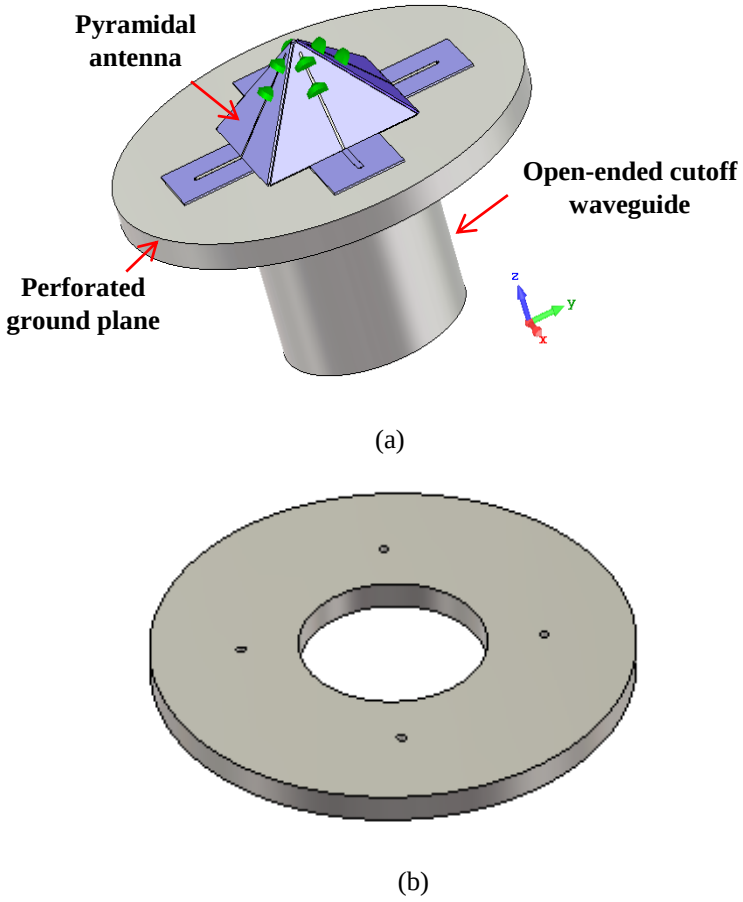

Figure 4.1: The initial antenna design, (a) Pyramidal antenna, (b) Its perforated ground plane.

Two types of polarization can be generated using this configuration: linear polarization, achieved by exciting two opposite monopoles with the same amplitudes and a 180° phase shift, or circular polarization, achieved by exciting all four monopoles with equal amplitudes and a 90° progressive phase shift. The significance of this geometry lies in its ability to provide hemispheric radiation with circular polarization, making it particularly well-suited for satellite communication applications.

In addition, the multiband behavior is achieved by incorporating two trap loads, each consisting of a parallel LC circuit. These trap loads are characterized by a resonance frequency of: $f_c = 1/\sqrt{LC}$.

The positions of the trap loads along the radiating elements are illustrated in Figure 4.2. It is apparent that trap load No_1 and trap load No_2 are strategically placed on the surface of each monopole within the gaps to achieve multiband behavior. Through the adjustments to the length of the monopole antenna and the inclusion of trap load No_1 and trap load No_2, a triple-band frequency can be generated centred at $f_1 = 1.197$ GHz, $f_2 = 1.575$ GHz, and $f_3 = 2.245$ GHz,dedicated for GPS/Galileo/Micro-Sat applications, respectively.

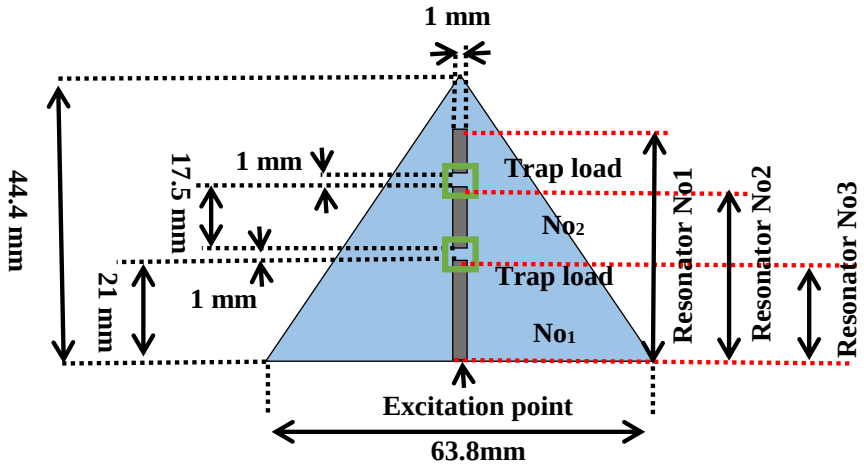

Figure 4.2: Trap loads locations.

The existence of the hole in the ground plane induces unwanted rear electromagnetic radiation. To address this issue, authors in [103], have been introduced a sizable metallic cut-off open-ended waveguide of length of 70 mm, as depicted in Figure 4.1. This design is considered as a versatile and generic solution that provides a wide range of performances benefits. It can offer different radiation patterns forms by controlling the inclination angles. In addition, the resonances frequencies can be adjusted by changing the length of monopoles, providing flexibility in adapting to specific communication or navigation requirements. The versatility extends to polarization options, enabling both linear and circular polarization as needed. This capability is especially valuable in applications like satellite communication or GNSS systems, where different polarization types may be required. However, the use of waveguide introduces a challenge of creating a bulky structure. To overcome this limitation, this work suggests replacing

the open-ended cutoff waveguide with a triband artificial magnetic conductor reflector. The introduction of the triband AMC reflector aims to address the issue of bulkiness associated with the traditional waveguide. It allows for a substantial reduction in the antenna's size and backward radiation. It is worth noting that various modifications have been made to the initial structure in order to meet our objectives including miniaturisation and enhancing the backward radiation.

4.2.2 Triband AMC unit cell design

The geometry of the suggested triband AMC unit cell is illustrated in Figure 4.3. It features a metallic square patch that is slotted with two square rings, providing the desired triple-band behavior. The designed AMC is printed on a Rogers RO3010 dielectric substrate with a thickness of 5 mm, a relative permittivity of 10.2, and a loss tangent of 0.0004.

The step-by-step development of the proposed unit cell is illustrated in Figure 4.4. In the initial design phase (step 1), the AMC unit cell features a metallic square patch with a length of 25 mm, responsible for the lower operating frequency of 1.197 GHz. Subsequently, in step 2 and step 3, two square rings slots are etched into the main metallic square patch, allowing for the achievement of the two higher operating frequencies: 1.575 GHz and 2.245 GHz.

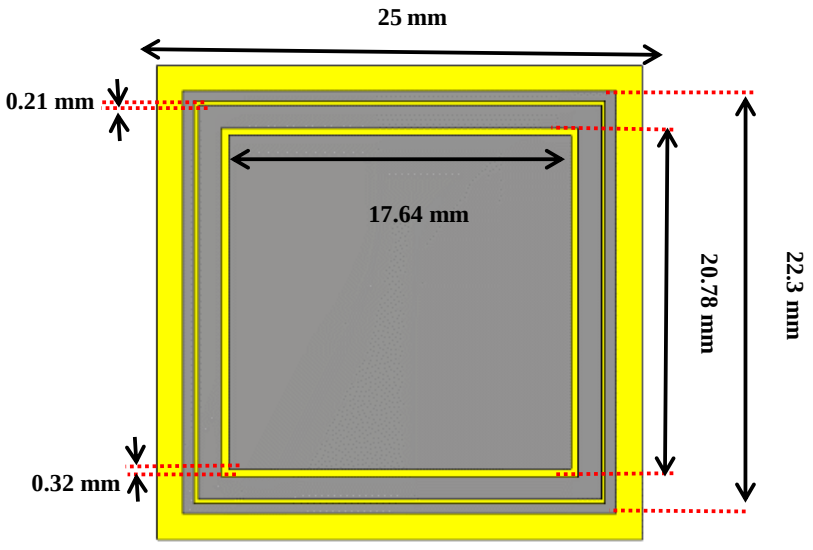

Figure 4.3: Triband unit cell design.

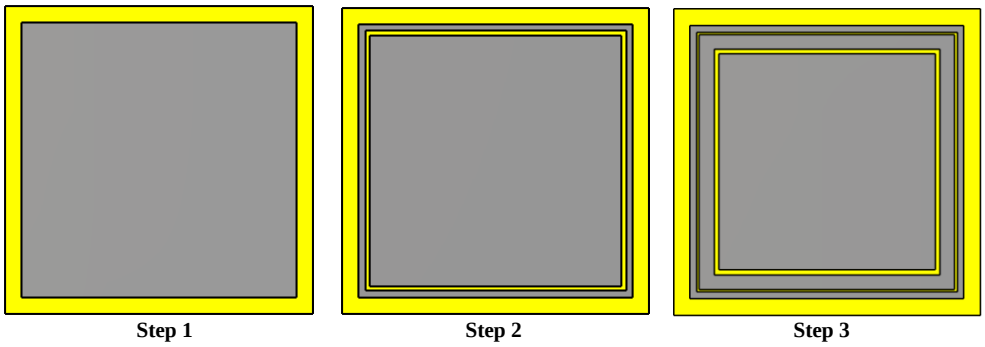

Figure 4.4: The step-by-step progression of the proposed triband AMC unit cell.

Figure 4.5, illustrates the reflection phase response of the proposed triband AMC unit cell. This electromagnetic response is obtained by using, a boundary condition approach around the specified unit cell using CST software. The AMC exhibits three zero-phases in the reflection coefficient at 1.197, 1.575, and 2.245 GHz, along with a triple in-phase bandwidth of 1.16-1.22 GHz, 1.56-1.58 GHz, and 2.15-2.35 GHz, respectively. The novelty of this structure lies in its quasi-independence and its capability to analytically estimate the three operating frequencies [104].

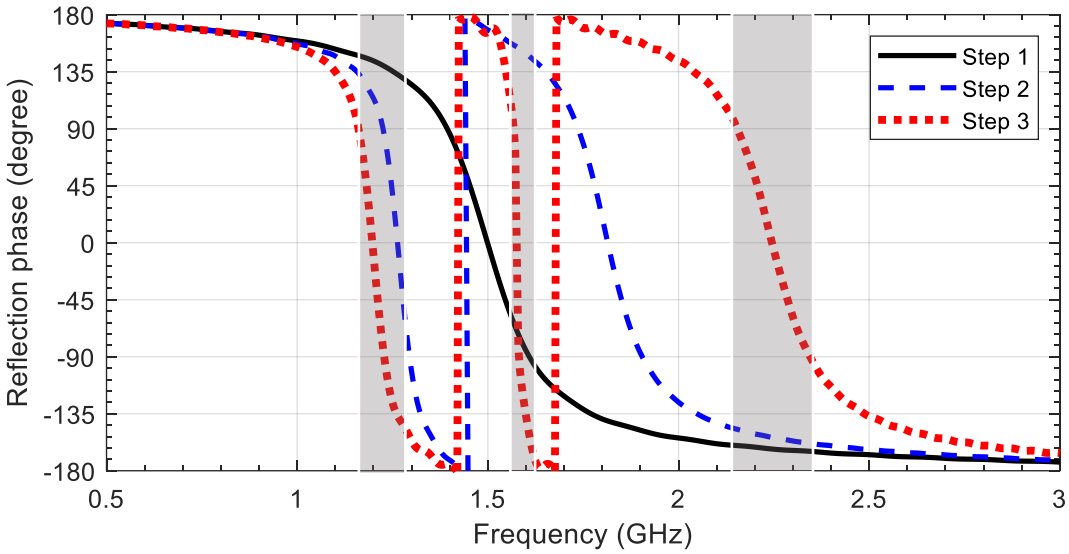

Figure 4.5: Reflection phase response of the proposed triband AMC unit cell.

4.2.3 Trap-loaded pyramidal antenna over the triband AMC reflector

The proposed trap-loaded pyramidal antenna backed by the triband AMC is illustrated in Figure 4.6. An airspace of 3 mm is maintained between the pyramidal antenna and the AMC reflector.

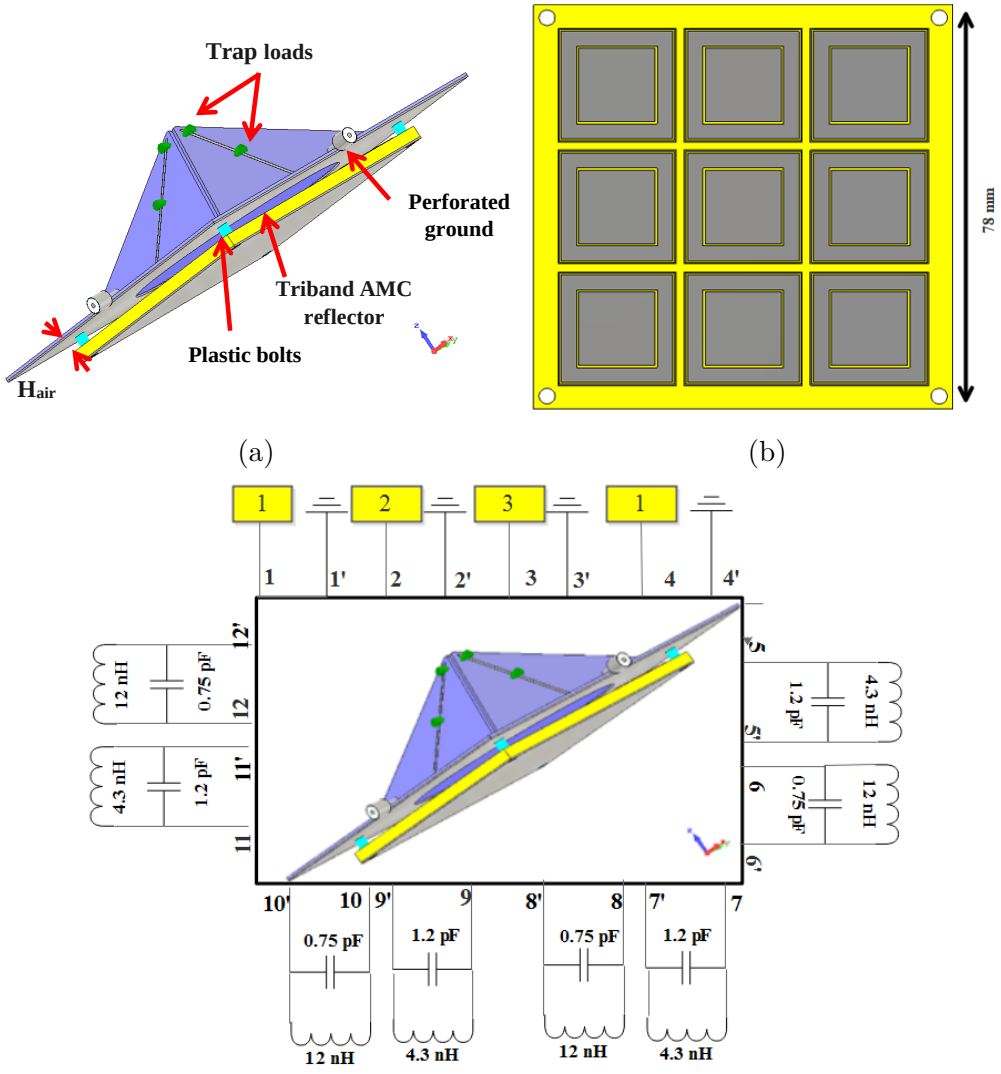

Figure 4.6: Geometry of the proposed combined configuration, (a) The pyramidal antenna, (b) 3×3 triband AMC reflector, (c) Circuit model of the trap loads used for multiband behaviour.

Table 4.1: The selected elements of the trap loads

	Component	Value	Reference number
« Trap load No1 »	Inductor	04.3 nH	LQW18AN4N3C00
	capacitor	01.2 pF	GQM1885C2A1R2CB01
« Trap load No2 »	Inductor	12.0 nH	LQW18AN12NG10
	capacitor	0.75 pF	GQM1885C2AR75CB01

Additionally, the assembly of this configuration are achieved through the use of four plastic bolts with accompanying nuts. The obtained triband behavior resulting from the trap loads is investigated using another simulation tool, schematic CST Design tool, as shown in Figure 4.6(c). Two parallel LC resonant circuits representing Trap load No_1 and Trap load No_1 are placed in the gaps between the monopoles. The values of this trap loads are listed in Table 4.1.

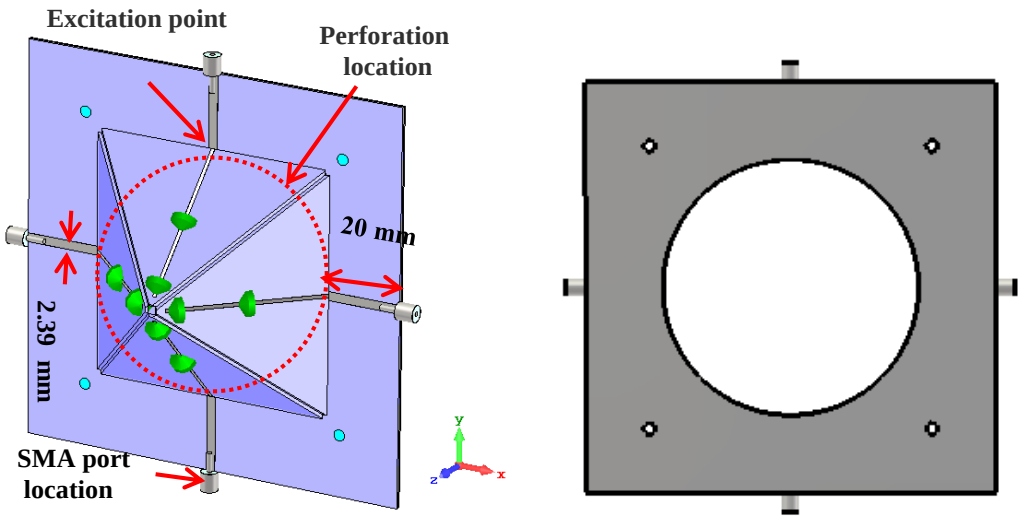

(a) (b)

Figure 4.7: Geometry of the modified pyramidal antenna, (a) The pyramidal antenna, (b) The modified pyramidal antenna design, (c) Antenna perforated ground plane (bottom view).

As illustrated in Figure 4.7, a square ground plane, featuring a circular perforation with a diameter of 66 mm, is strategically positioned at the base of the pyramidal structure to guarantee optimal impedance matching. Its parametric study will be discussed later. Four 50 Ω SMA connectors are used to feed the monopole antennas via four 50 Ω microstrip lines. A circular polarization is obtained by feeding the four monopoles with

90° phase shift (a quadratic phase excitation). As observed in Figure 4.6(b), the triband AMC is composed of 3×3 periodic square ring unit cells. The original design presented in [103], has been modified and several parametric studies has been made in order to meet our objectives, including: ground plane perforation, air layer thickness, surface current distributions.

4.2.4 Key design parameter investigations

a Ground plane perforation

The influence of the ground plane perforation is presented in Figure 4.8. Three cases were investigated, a ground plane without perforation, a ground plane with square perforation, and a ground plane with circular perforation. It is crucial to highlight that the introduction of perforation is intended to achieve optimal impedance matching, as discussed in [103]. Consequently, this investigation only focuses on the reflection coefficient.

In the absence of ground plane perforation, poor impedance matching is observed with values of -9.3 dB and -7.81 dB for the lower and middle frequencies, respectively. However, a significant improvement is noted in in the upper frequency band with an impedance matching of -12.4 dB. Conversely, the ground plane with square perforation demonstrates a good impedance matching of -17.3 dB and -12 dB for the lower and middle frequency bands, but exhibits a poor impedance matching of -6.6 dB in the upper frequency band.

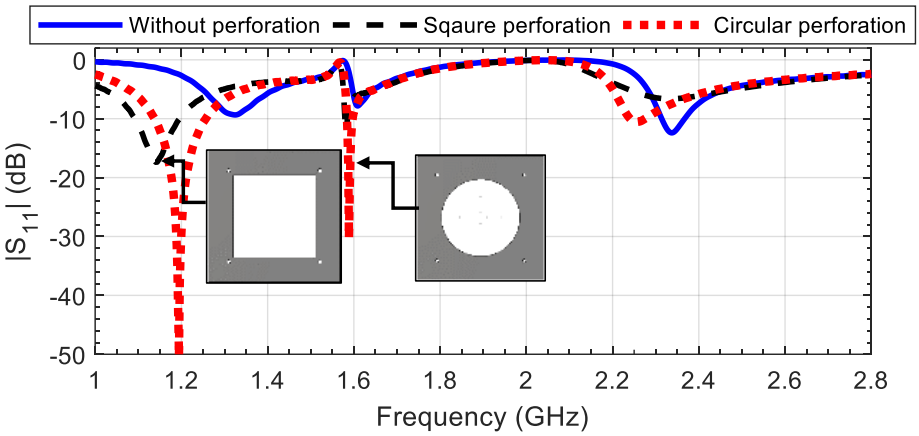

Figure 4.8: Impact of the ground plane perforation on the trap-loaded pyramidal antenna (Without AMC) impedance matching.

The introduction of circular perforation in the ground plane surface results in an optimal impedance matching ($\mid S_{11} \mid \leq -10$ dB) across all three operating frequency bands. In conclusion, it is evident that circular perforation plays a vital role in achieving superior impedance matching within the desired frequency range.

b Air layer thickness

The impact of the air layer thickness (H_{air}) between the antenna and the AMC reflector is introduced in Figure 4.9. This effect in investigated on several antenna performances, including reflection coefficient and backward radiations.

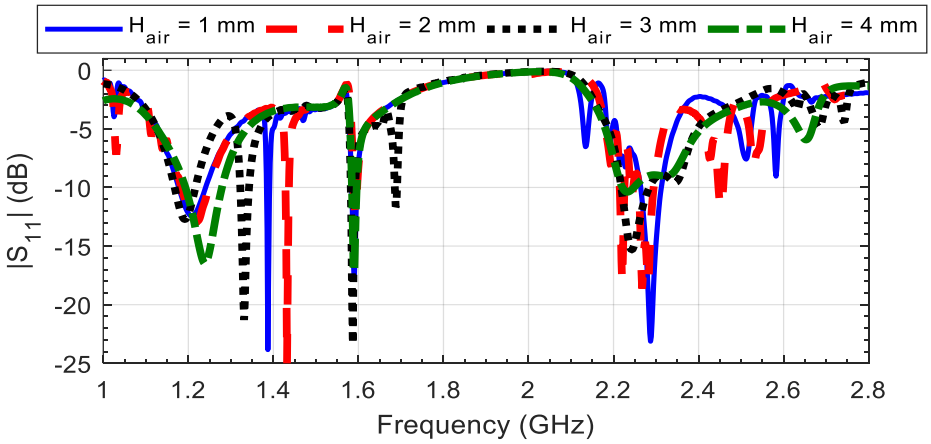

Figure 4.9: Impact of the air layer thickness on the trap-loaded pyramidal antenna (with AMC) reflection coefficient responses.

The variation of H_{air} from 1 to 4 mm induces a frequency shift in the lower frequency band, with a minimal effect observed in the middle band. Additionally, an increase in H_{air} leads to degradation in impedance matching. Furthermore, an observable impact on the antenna's backward radiation is noted with the increase in H_{air}.
Table 4.2, illustrates the influence of H_{air} on the Right-Handed Circular Polarization (RHCP) directivity at $\theta = 0°$ and Left-Handed Circular Polarization (LHCP) directivity at $\theta = 180°$ across the three operating frequencies: f_1, f_2, and f_3. These frequencies correspond to the resonance frequencies associated with each specific H_{air} value.
The primary objective of this study is to analyses the backward radiation, specifically indicated by LHCP directivity at $\theta = 180°$.

Table 4.2: Air layer thickness impact on LHCP and RHCP directivity levels.

Air thickness H_{air} (mm)	RHCP Directivity at θ = 0° (dB) (forward radiation)			LHCP Directivity at θ = 180° (dB) (backward radiation)		
	f_1	f_2	f_3	f_1	f_2	f_3
1	5.30	5.00	5.40	- 6.30	- 6.27	- 7.17
2	5.32	5.04	6.41	- 9.50	- 8.82	- 7.27
3	5.60	5.92	5.50	- 9.55	-10.51	- 16.97

The investigation will specifically focus on cases where H_{air} is strictly less than 4 mm, taking into account the observed poor antenna impedance matching beyond this threshold. At the lower resonant frequency f_1, an increase in H_{air} at the lower resonant frequency causes a minor improvement in RHCP directivity. The maximum values are 5.3 dB, 5.32 dB, and 5.60 dB, accompanied by backward radiation levels of - 6.3 dB, - 9.5 dB, and - 9.55 dB for $H_{air} = 1$ mm, $H_{air} = 2$ mm, and $H_{air} = 3$ mm, respectively.
At the middle resonant frequency f_2, maximum RHCP directivity values range from 5 to 6 dB, accompanied by corresponding backward radiation values of - 6.27 dB, - 8.82 dB, and - 10.51 dB for $H_{air} = 1$ mm, 2 mm, and 3 mm, respectively.
Furthermore, at the upper resonant frequency f_3, a significant enhancement in backward radiation is observed, as H_{air} increases from 1 mm to 3 mm. Based on the above-mentioned discussion, an H_{air} of 3 mm constitutes a good trade-off between impedance matching and backward radiation levels.

c Surface current distribution

The surface current distribution across the entire structure (pyramidal antenna + AMC) is displayed in Figure 4.10, at three distinct resonant frequencies: 1.197 GHz, 1.575 GHz, and 2.245 GHz. At 1.197 GHz, the currents is displayed along the entire length of the monopole antenna. Conversely, at 1.575 GHz , the current concentrates on the two lower portions of the monopole antenna. Finally, at 2.245 GHz, the current localizes predominantly on the lower extremity of the monopole antenna. Moreover, the AMC exhibits negligible surface current distributions, except at the frequency of 2.245 GHz, where surface currents concentrate specifically at the four corners of the AMC reflector. Notably, the limited current circulation on the AMC reflector plays a crucial role in preventing performance degradation, particularly in terms of radiation.

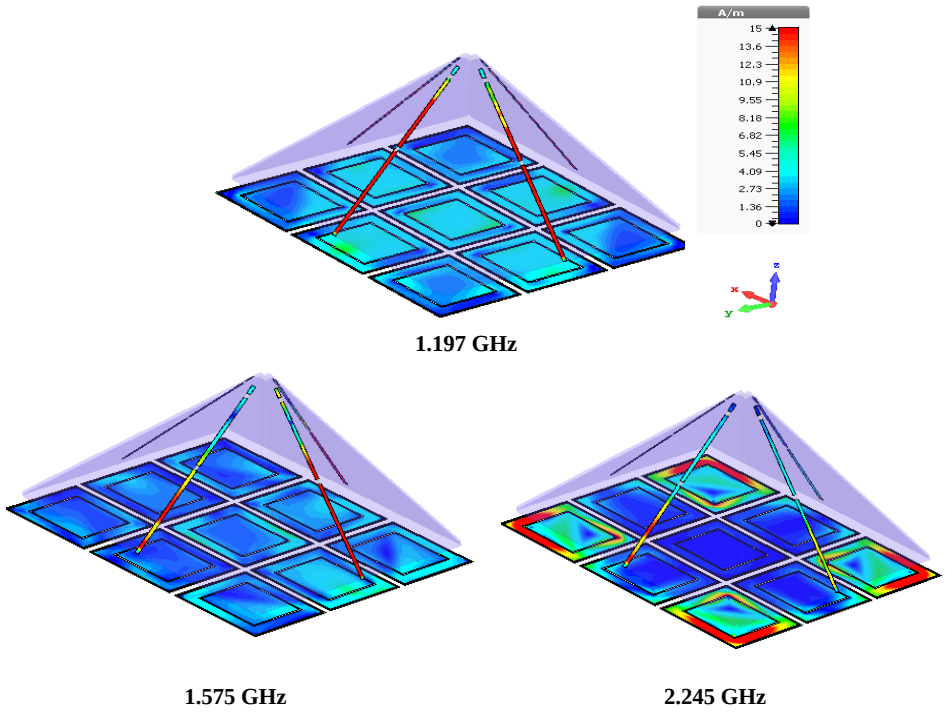

Figure 4.10: Simulated surface current distribution on the whole structure

4.2.5 Results and discussion

The resulting reflection coefficient of the proposed radiating structure is depicted in Figure 4.11. The proposed pyramidal antenna over the triband AMC reflector exhibits triband behaviour, with three operating frequency bands cantered at 1.197 GHz, 1.575 GHz, and 2.245 GHz, respectively.

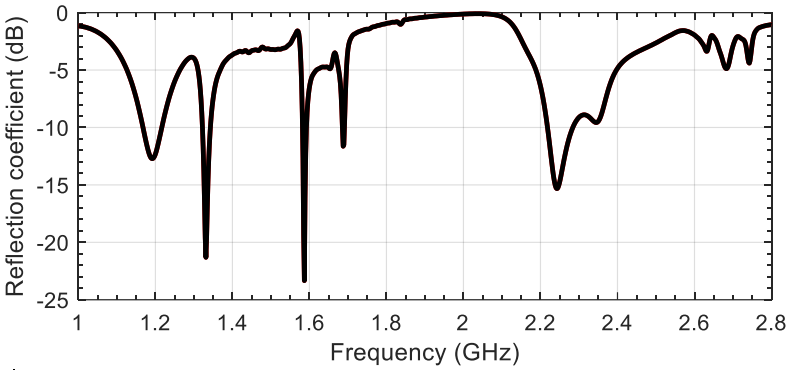

Figure 4.11: Simulated reflection coefficient response of the pyramidal antenna over the triband AMC reflector.

The emergence of additional resonances in the frequency bands of 1.32-1.34 GHz and 1.68-1.69 GHz, results from the interaction between the trap-loaded pyramidal antenna and the triband AMC reflector. Thus, it is important to optimize the entire structure (antenna + AMC) to achieve optimal performances.

Moreover, the directivity pattern of RHCP and LHCP across the three operating frequencies (1.197, 1.575, 2.245 GHz) is depicted in Figure 4.12.

The Circular polarization plotting is achieved through post-processing tools in CST software, involving the equal feeding of the four monopoles with equal amplitudes and a 90° phase shift between two adjacent ports in a circle. This configuration results in left-hand circular polarization (LHCP), while right-hand circular polarization (RHCP) can be attained by changing the phase shift direction. The polarization sense is determined by the sign of the 90° phase shift between successive feeding ports.

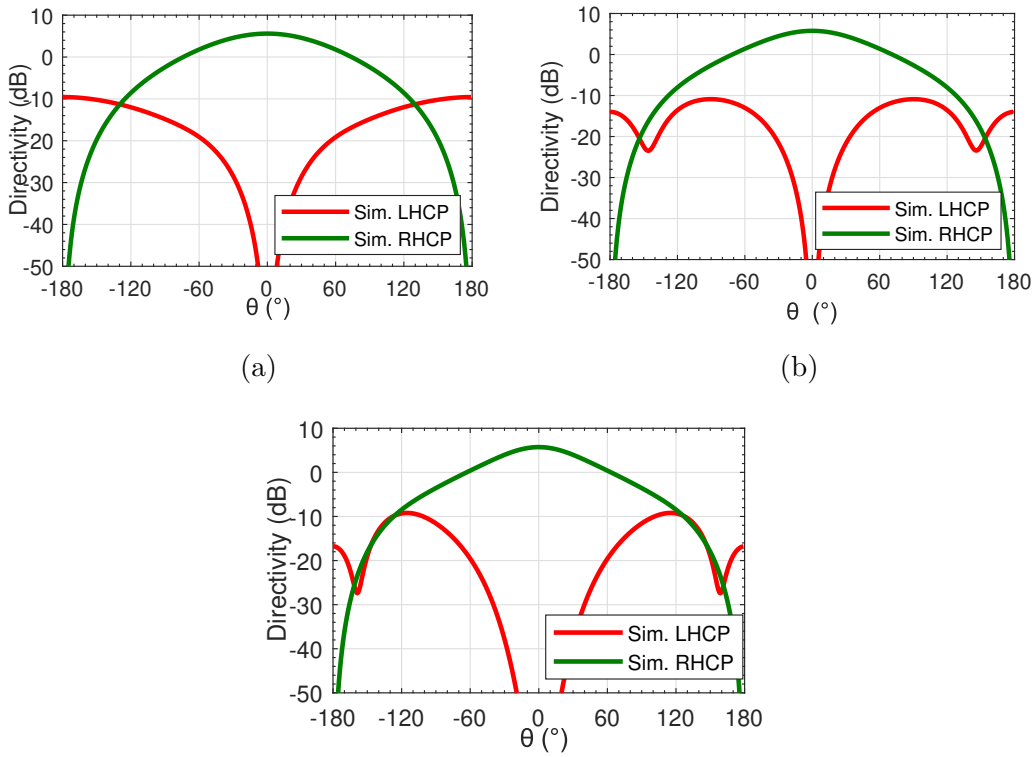

Figure 4.12: Simulated directivity radiation pattern (LHCP and RHCP) at: (a) 1.197 GHz, (b) 1.575 GHz, (c) 2.245 GHz.

It is worth mentioning that our study aims to analyses both forward and backward radiation, indicated by levels of the RHCP and LHCP directivity at $\theta = 0°$ and $\theta = 180°$, respectively. It can be observed that the proposed design exhibits quasi-hemispheric radiation patterns with simulated peak directivity levels (forward radiation) of 5.60 dB, 5.92 dB, and 5.50 dB at the three specified operating frequencies: 1.197 GHz, 1.575 GHz, and 2.245 GHz, respectively. Additionally, there is a significant reduction in simulated backward radiation levels by 9 dB, 7.5 dB, and 8.3 dB compared to the previous design at these frequencies.

4.2.6 Prototype of the trap-loaded pyramidal antenna loaded-with the triband AMC reflector

The pyramidal antenna with the integrated AMC reflector has been manufactured, assembled, and tested, as illustrated in Figure 4.13. A pyramid structure made of polystyrene strategically placed beneath the four faces of the monopoles to offer mechanical reinforcement for the pyramidal antenna. Furthermore, the selected Murata components L and C values are outlined in Table 4.1.

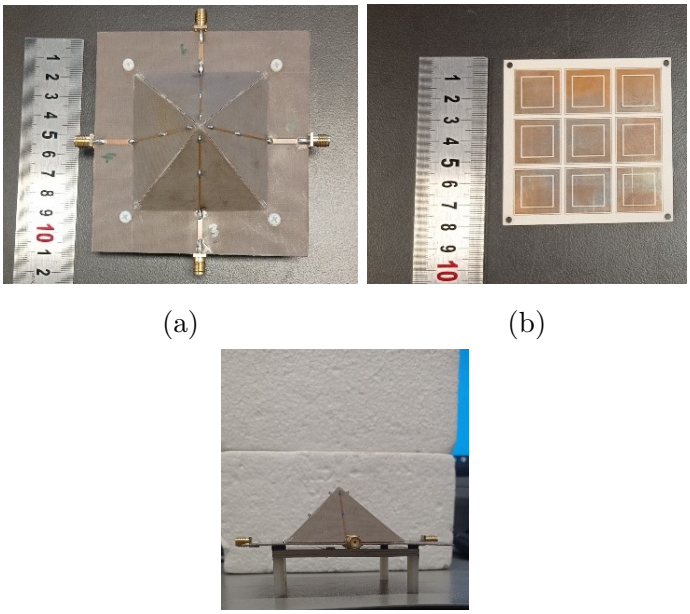

(a) (b)

(c)

Figure 4.13: The fabricated pyramidal antenna over the triband AMC reflector, (a) The fabricated antenna, (b) The fabricated triband AMC reflector, (c) The fabricated assembly.

It's important to highlight that these traps are uniformly positioned on each radiating element, preserving in the antenna structure symmetry. The reflection coefficient is measured using the Keysight Agilent PNA Network Analyzer N5222A. As all antenna ports exhibit symmetry, the S-parameter measurements are conducted only on port number 1, while the remaining three ports are terminated with 50 Ω loads. The measured S-parameter of the fabricated configuration is illustrated in comparison to the simulated one in Figure 4.14. The simulated resonant frequencies are noted as: 1.197 GHz, 1.575 GHz, and 2.245 GHz, while the measured ones are: 1.20 GHz, 1.58 GHz, and 2.29 GHz. A good agreement is observed between the simulated and measured data, with slight frequency shifts of 3 MHz, 5 MHz, and 45 MHz at lower, middle, and higher resonance frequencies, respectively. These discrepancies can be attributed to fabrication inaccuracies.

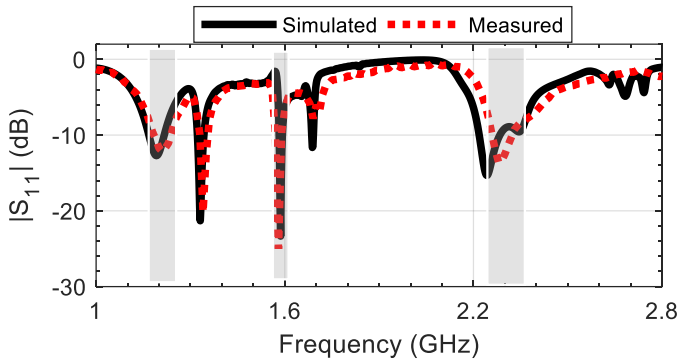

Figure 4.14: Simulated and measured reflection coefficient of the proposed trap-loaded pyramidal antenna over the triband AMC reflector.

The radiation measurements were conducted using the MVG StarLab anechoic chamber (Appendix B) at the LCIS laboratory in France, as depicted in Figure 4.15. The simulated and measured RHCP and LHCP radiation patterns of the antenna at 1.20, 1.58, and 2.29 GHz are illustrated in Figure 4.16. The LHCP and RHCP directivity patterns have been generated and synthesized through post-processing, utilizing the linear measured E-theta and E-phi data from the four ports. The measurements were conducted using only one port, and the data for the remaining ports can be derived through coordinate rotation techniques (Appendix C). The plotted results demonstrate hemispheric radiation patterns for the three operational frequencies, offering a significant advantage for satellite antennas. Furthermore, there is a good agreement between simulated and measured results, revealing maximum measured RHCP directivity levels

of 5.12 dB, 6.6 dB, and 7 dB centred at 1.20 GHz, 1.58 GHz, and 2.29 GHz, respectively. The measured cross-polarization LHCP, representing backward radiation, records values of -8.06 dB, -14 dB, and -12.65 dB across the three measured resonant frequencies. It's observed that the measured LHCP and RHCP levels are slightly different from the simulated values, particularly at the third resonance frequency (around 4 dB). This discrepancy is may attributed to measurement errors linked to the supporting structure in the measurement setup, an aspect not present in the simulation modeling.

Figure 4.15: Measurement setup in the anechoic chamber MVG StarLab system.

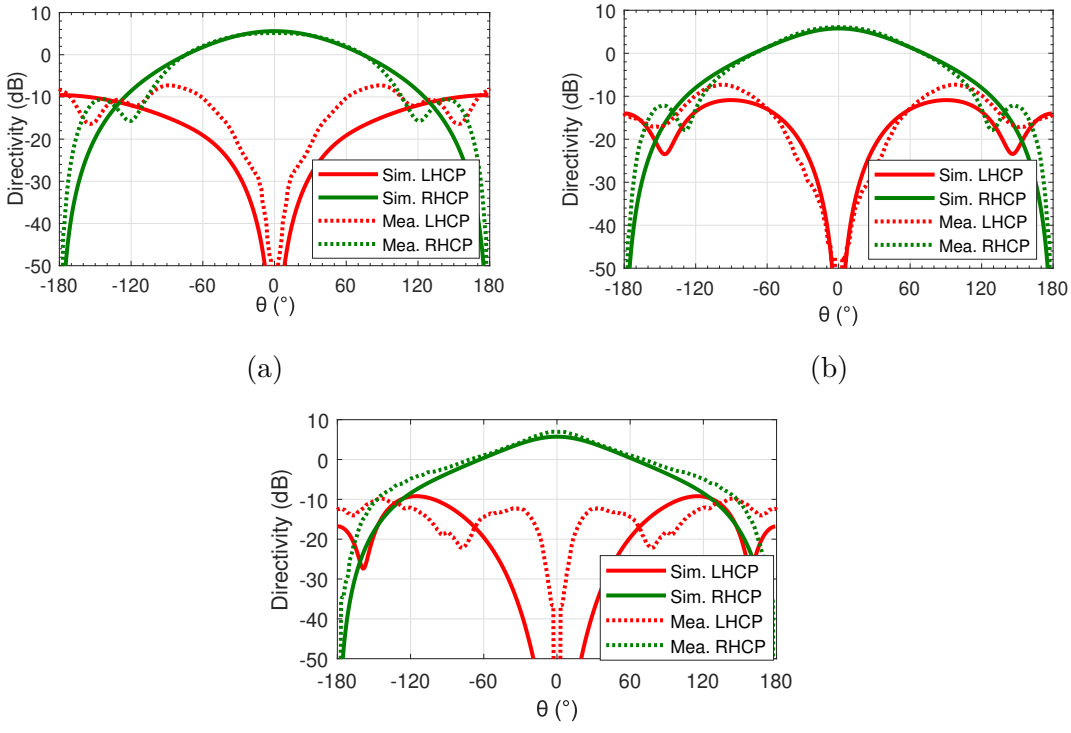

Figure 4.16: Directivity radiation pattern (LHCP and RHCP) at: (b) 1.20GHz, (c) 1.58 GHz, (d) 2.29 GHz.

4.2.7 Proposed structure contribution

Table 4.3, presents a comparative analysis of various versions of the pyramidal antenna, considering both those with and without backward radiation reduction techniques, across three distinct operating frequency bands. It is evident, that the use of either an open-ended waveguide or a triband AMC reflector significantly improves radiation performance, especially in terms of reducing backward radiation levels. However, integrating the triband AMC as a reflector for the pyramidal antenna results in a substantial improvement in simulated backward radiation levels reductions of 12.2 dB, 14.42 dB, and 21.74 dB at the three operating frequencies, respectively, compared to the configuration without the AMC reflector.

Table 4.3: Comparison between various versions of the pyramidal antenna

Design	**Frequency (GHz)**		**RHCP Dir. (dB) θ = 0°**		**LHCP Dir. (dB) θ =180°**	
	Sim.	**Mes.**	**Sim.**	**Mea.**	**Sim.**	**Mea.**
Pyramidal antenna (106×106×30.79) mm^3 (0.42×0.42×0.12) λ_L	1.197	/	4.69	/	2.65	/
	1.575	/	5.22	/	3.87	/
	2.245	/	5.00	/	4.77	/
Pyramidal antenna with waveguide [103] (170×170×110.67) mm^3 (0.68×0.68×0.44) λ_L	1.197	1.22	6.28	7.5	-0.34	- 9.0
	1.575	1.61	6.82	7.0	-2.99	-6.90
	2.245	2.28	6.39	6.1	-8.67	-13.0
Pyramidal antenna with triband AMC (106×106×37.60) mm^3 (0.42×0.42×0.15) λ_L	1.197	1.20	5.6	5.12	-9.55	-8.06
	1.575	1.58	5.92	6.6	-14.0	-14.0
	2.245	2.29	5.50	7.0	-16.9	-12.6

Furthermore, this technique results in a significant reduction in the overall structure size when compared to the use of an open-ended waveguide [103], while maintaining quite similar radiation performances. Specifically, by placing the triband AMC reflector at a distance of 0.01 λ_L (where λ_L is the wavelength at 1.197 GHz) from the pyramidal antenna, the overall structure is reduced by 37% along both the x and y axes (from 0.68 λ_L to 0.42 λ_L) and by 67% along the z-axis (a substantial thickness reduction from 0.44 λ_L to 0.15 λ_L compared to the original structure. The simulated RHCP levels exhibit slight variations compared to those in [103], which can be attributed to the significant modification in the pyramidal antenna's ground plane. In conclusion, it can be affirmed

that the proposed backward reduction technique based on the AMC reflector leads to a more compact structure, ease of integration, and a lighter overall design compared to the previous configuration in [103]. This makes it a promising candidate for satellite applications.

4.3 Application II: Gain enhancement of dual-band monopole antenna using a dual-band AMC reflector for sub 6 GHz and 7 GHz 5G application.

Nowadays, fifth generation technologies become the hottest research topic for many researches and industries due to its significance advantages including: high data rate and capacity and increased connectivity. Based on [105] the are many frequency bands used for 5G new radio such as: n77 (3.3- 4.2) GHz/n78 (3.3-3.8) GHz /n79 (4.4-5) GHz for sub 6 GHz 5G application while for the applications above 5 GHz, n96 (5.9-7) GHz for sub 7 GHz 5G application. We aim to investigate the gain enhancement of a multiband antenna using a multiband Artificial Magnetic Conductor (AMC) reflector for 5G applications.

4.3.1 Dual-band monopole antenna structure

The proposed dual-band monopole antenna structure is shown in Figure 4.17. It is designed on 1.6 mm thick FR4 substrate in size of 50×50 mm^2 with relative permittivity of 4.3, and loss tangent of 0.025. This structure consists of a simple rectangular patch geometry slotted with a Rectangular Split Ring (RSRR) slot in order to achieve the multiband behavior. The proposed dual-band monopole antenna is fed with 50 Ω microstrip line loaded on a partial ground plane as shown in Figure 4.17(b).
The dimensions of the proposed dual-band antenna are given in Table 4.4.
The simulated reflection coefficient and the broadside gain of the proposed antenna are provided in Figure 4.18. It can be observed that the proposed antenna can exhibit a double frequency band of 3.22-3.53 GHz and 5.97-6.24 GHz, centred at 3.06 GHz and 6.16 GHz, respectively.

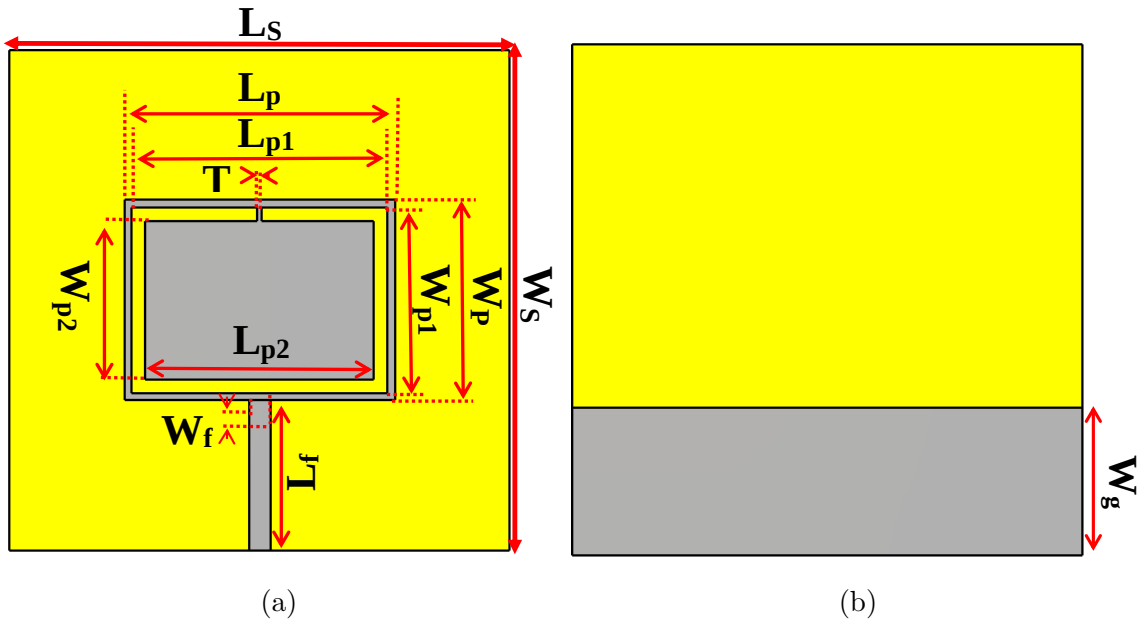

Figure 4.17: Geometry of the dual-band monopole antenna, (a) Top view, (b) Bottom view.

Table 4.4: Dimensions of the dual-band monopole antenna

Parameter	L_s	W_s	L_p	W_p	L_{p1}	L_{p2}
Value (mm)	50	50	27	20	25.6	22.8
Parameter	W_{p1}	W_{p2}	T	W_g	W_f	L_f
Value (mm)	18.6	15.8	0.3	14.5	2.39	15

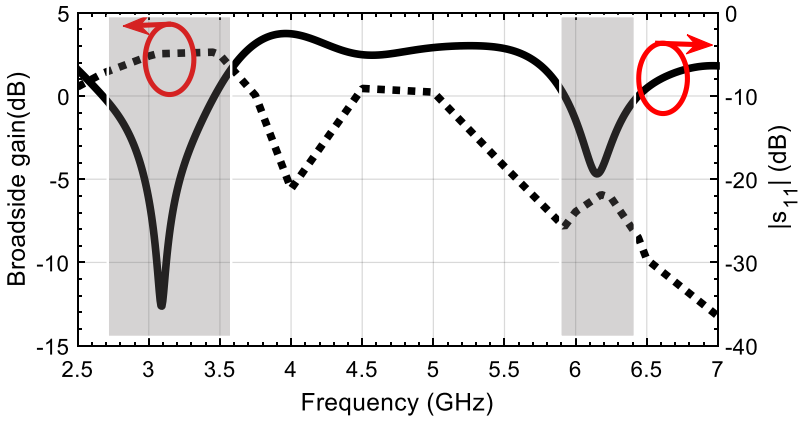

Figure 4.18: Simulated reflection coefficient and broadside gain of the dual-band monopole antenna.

The broadside gain is above 2, -6.12 dB at the lower band (3.22-3.53 GHz) and the upper band (5.97-6.24 GHz), respectively. In order to demonstrate the antenna dual-band behavior, the surface current evolution is also evaluated in Figure 4.19, at the two resonant frequencies 3.06 and 6.16 GHz, respectively. At the first resonant frequency, the current is mainly concentrated on the upper part of the feed line, the boundaries of the inner and outer rectangular rings. At the second resonant frequency, the current is strongly focused on the feed line, the middle of the partial ground plane, the outer, and the inner rectangular rings. The current distributions prove that the resonant frequency depends not only on the antenna dimensions but also on the feed line, the partial ground plane, and the spacing between the rectangular rings.

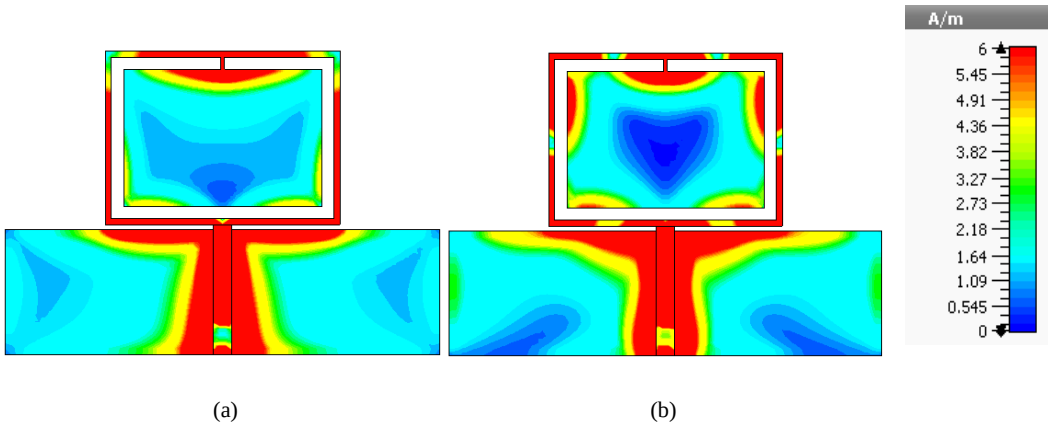

Figure 4.19: Surface current distribution of the dual-band monopole antenna at: (a) 3.06 GHz, (b) 6.16 GHz.

4.3.2 Dual-band monopole antenna over the dual-band AMC reflector

As the triband unit cell presented in Section 4.2.2 (see Figure 4.3), demonstrates the ability to operate in single, dual, or triband operations across independent frequencies, along with its analytical estimation abilities. We effortlessly modify its geometry and dimensions (see Figure 4.20) to achieve a dual-band unit cell, operating within frequency ranges 3.07-3.48 GHz and 5.93-6.16 GHz. The dimensions of the dual-band AMC unit cell are listed in Table 4.5. The reflection phase response of the proposed dual-band unit cell is depicted in Figure 4.21. It can be seen that the proposed dual-band unit cell exhibits two zeros-phases at 3.06 and 6.16 GHz across two AMC operating bands of 2.85-3.16 GHz and 5.64-6.79 GHz, respectively.

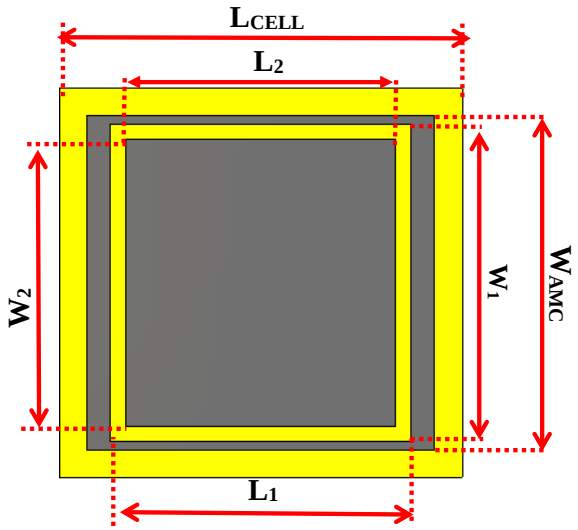

Figure 4.20: Geometry the proposed dual-band AMC unit cell.

Table 4.5: Dimensions of the proposed dual-band AMC unit cell.

Parameter	L_{CELL}	W_{AMC}	L_1	L_2	W_1	W_2
Value (mm)	13	11.5	10	8.9	10.9	9.9

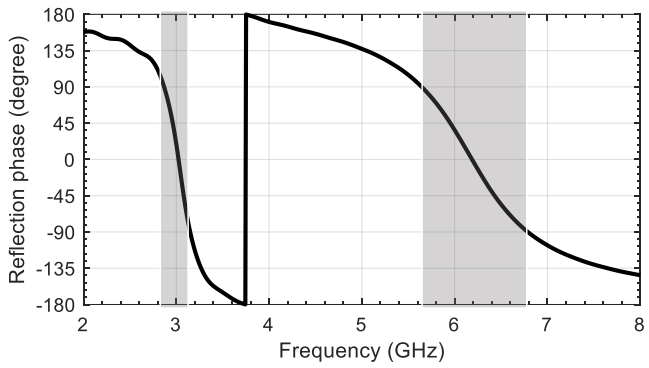

Figure 4.21: Simulated reflection phase of the proposed dual-band AMC unit cell.

As shown in Figure 4.22, the proposed dual-band AMC reflector backed monopole antenna is composed of 3×5 dual-band unit cells with an air layer thickness of 8 mm, which make the overall structure profile thickness 12.8 mm. The simulated reflection coefficient the proposed dual-band monopole antenna with the dual-band AMC reflector is plotted in Figure 4.23.

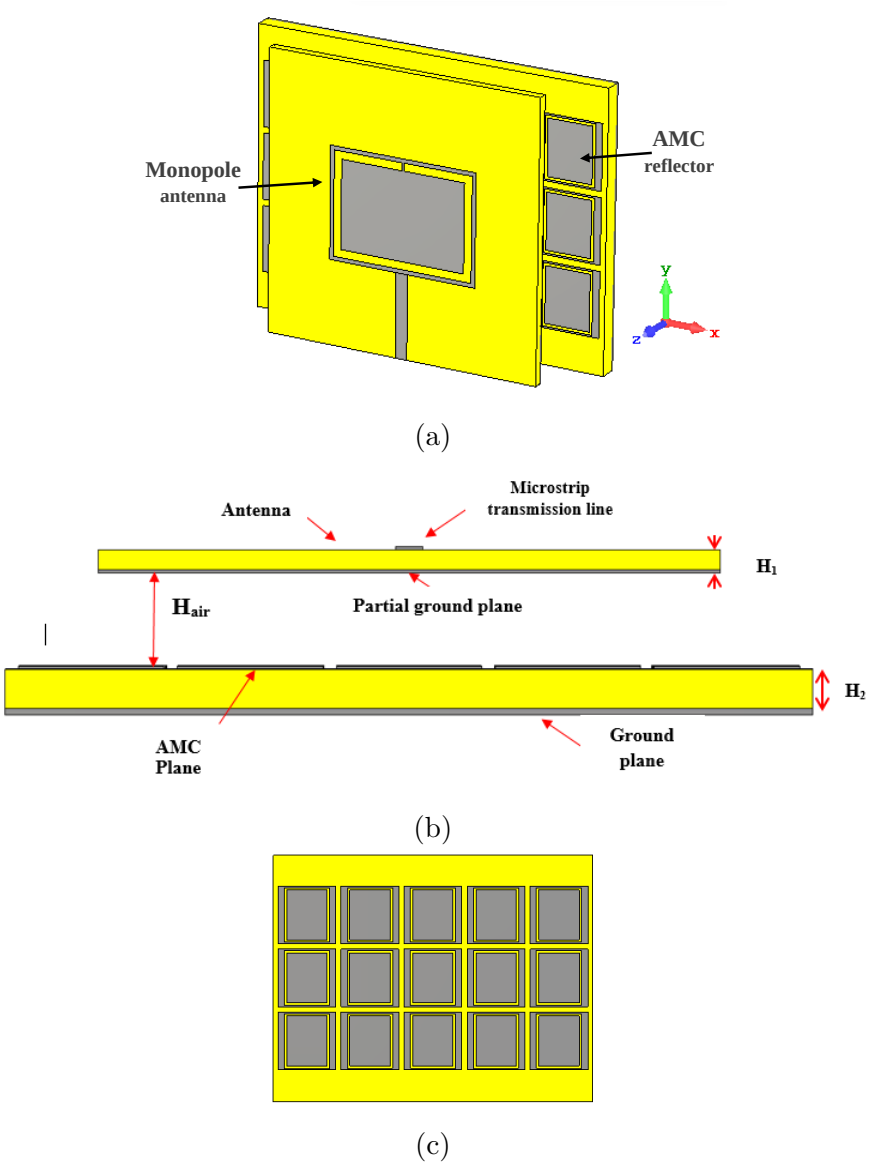

Figure 4.22: The dual-band monopole antenna over the slotted square ring patch AMC reflector, (a) Overall structure, (b) Side view, (c) AMC reflector top view.

The dual-band AMC backed-antenna covers two frequency bands from 3.07-3.48 GHz and 5.93-6.16 GHz, centred at resonant frequencies of 3.30 GHz and 6.10 GHz, respectively. Additionally, a comparison between the simulated broadside with/without AMC reflector is depicted in Figure 4.24. There is a gain enhancement of 4.51 dB at the first resonant frequency (3.30 GHz), but a significant decrease to –6.48 dB at the second resonant frequency compared to antennas without the AMC reflector.

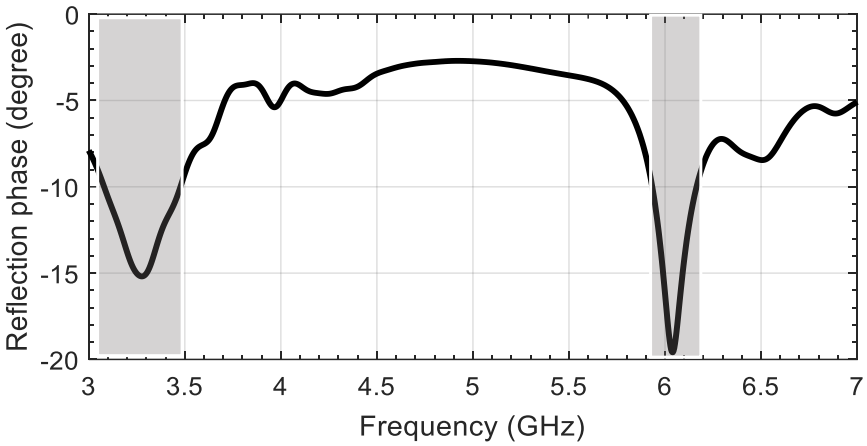

Figure 4.23: Simulated reflection coefficient response of the dual-band AMC backed antenna.

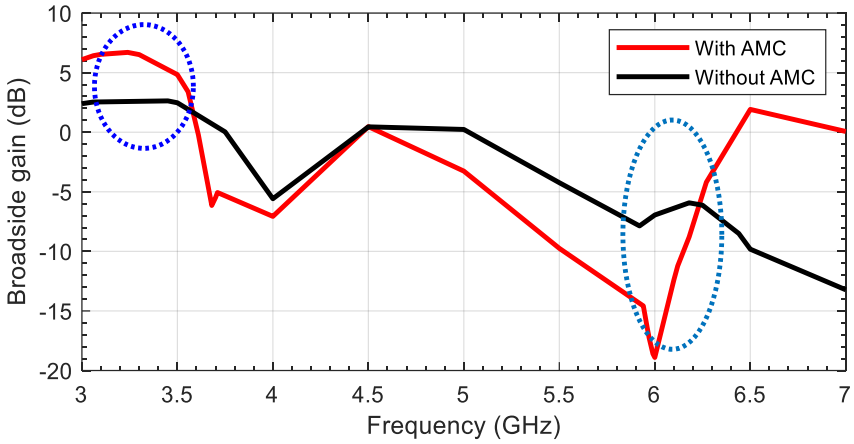

Figure 4.24: Simulated broadside gain of the proposed monopole antenna loaded with the dual-band AMC reflector.

It is noticeable that the proposed dual-band AMC reflector enhances the gain in only one band. Consequently, our objectives are not fully achieved.
To address this limitation, we propose modifying the rectangular slot responsible for the second operating band by closing it on the lower part, as illustrated in Figure 4.25. Further optimization of the proposed AMC unit cell is conducted to adjust the two resonant frequencies, 3.06 GHz and 6.16 GHz. The reflection phase response is depicted in Figure 4.30, and the final optimized dimensions are provided in Table 4.6.

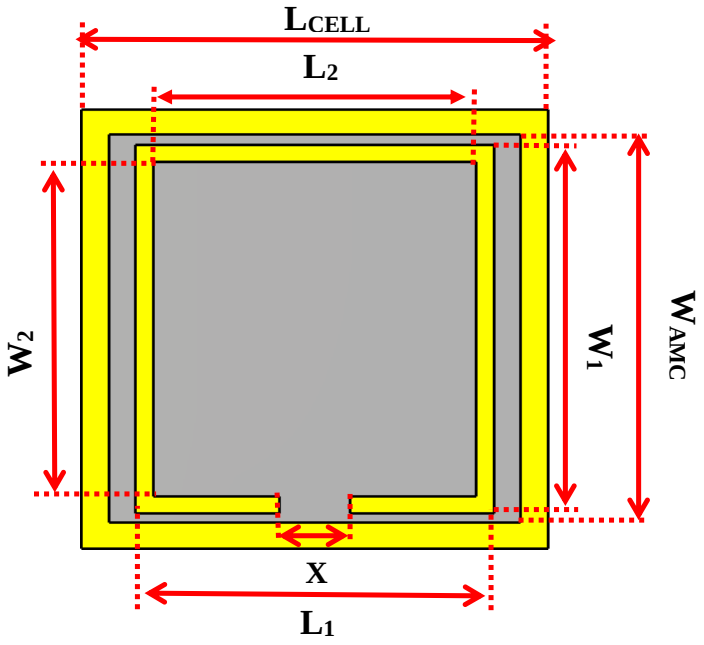

Figure 4.25: Geometry of the proposed modified dual-band AMC unit cell.

Table 4.6: Dimensions of the modified dual-band AMC unit cell.

Parameter	L_{CELL}	W_{AMC}	L_1	L_2	W_1	W_2	X
Value (mm)	13	11.5	10	9	10.9	9.9	2

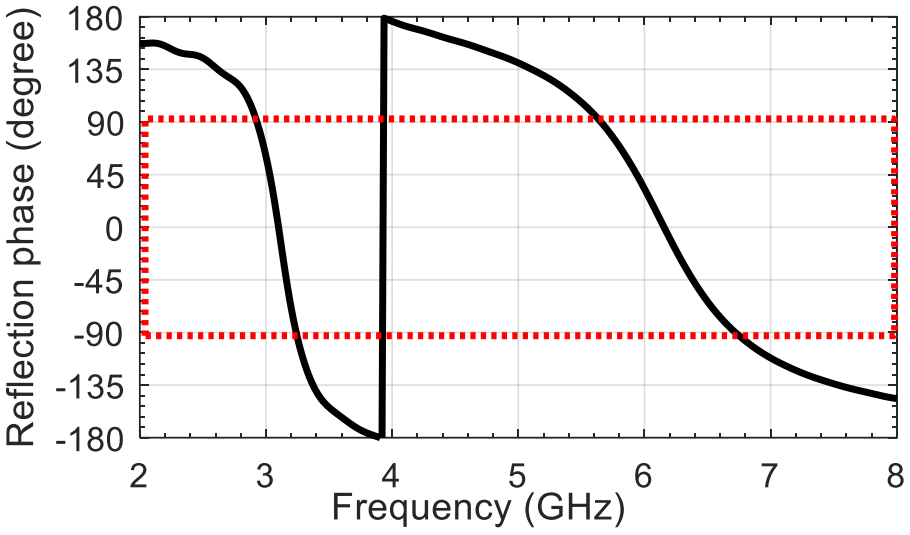

Figure 4.26: Simulated reflection phase response of the proposed modified dual-band AMC unit cell.

The simulated reflection coefficient and the broadside gain of the proposed dual-band monopole antenna over the modified AMC reflector are illustrated in Figure 4.27 and Figure 4.28, respectively. It can be seen that the proposed combined structure cover two-frequency bands in the range of 3.16-3.60 GHz and 5.96-6.23GHz centred at the frequencies of 3.40 GHz and 6.10 GHz, respectively. The gain is enhanced by 4.83 dB and 11.32 dB at the two resonant frequencies, respectively, in comparison to those without AMC reflector. In addition, it is noticeable that the gain is also enhanced compared to the proposed monopole antenna with the proposed dual-band AMC reflector before modification.

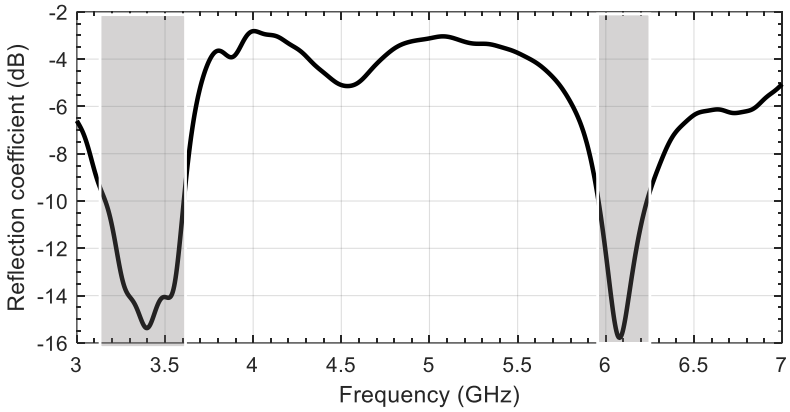

Figure 4.27: Simulated reflection coefficient of the proposed dual-band monopole antenna over the modified dual-band AMC reflector.

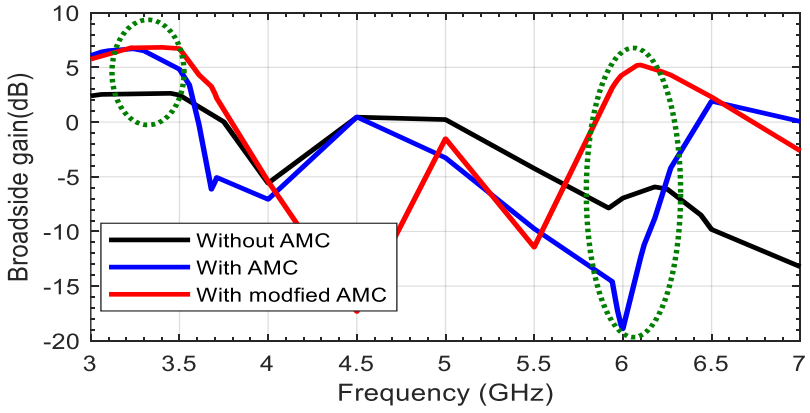

Figure 4.28: Simulated broadside gain of the proposed dual-band maonopole antenna over the modified dual-band AMC reflector.

In order to explain this gain enhancements, especially at the second resonant frequency, the surfaces current distribution on the two AMC reflectors is plotted in Figure 4.29. The surface current concentration is notably reduced on the modified dual-band AMC reflector compared to the first AMC reflector, which exhibits a strong current distribution across the entire AMC reflector surfaces. This difference in current distribution helps to explain the gain enhancement observed at the second frequency band.

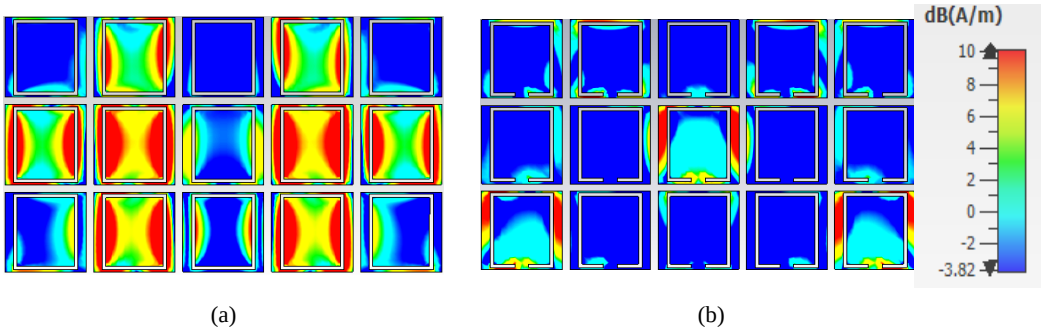

Figure 4.29: Current surface distribution on the AMC surface at 6.10 GHz, (a) Dual-band AMC reflector, (b) Modified dual-band AMC reflector.

The simulated radiation pattern of the dual-band antenna with and without the AMC reflector in E and H plane at 3.4 GHz and 6.10 GHz, are displayed in Figure 4.30. It is clearly seen, that for the antenna without AMC reflector the radiation pattern are bidirectional in both E and H plane with a poor gain values. However, after the incorporation of the AMC reflector it can exhibit a unidirectional radiation pattern enhanced gain of 7.06, 6.35 dB at to two resonant frequencies 3.40 GHz and 6.10 GHz,respectively.

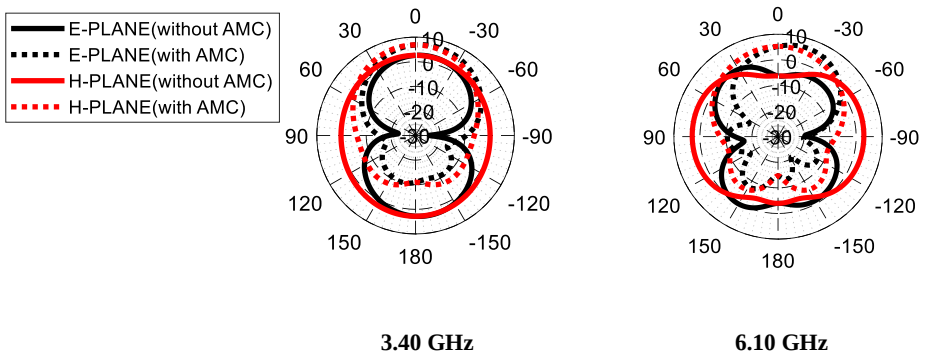

Figure 4.30: Simulated radiation pattern (in gain) of the proposed dual-band monopole antenna over the modified dual-band AMC reflector.

4.3.3 Key design parameter investigations

A parametric study is conducted in order to investigate the different parameters that affect the antenna characteristics. Two studies are carried out: The air layer thickness and the AMC unit cell numbers.

a Air layer thickness

The effect of the air layer thickness (the distance between the antenna and the AMC reflector H_{air}) on the reflection coefficient and the broadside gain is illustrated in Figure 4.31 . An H_{air} of 6 mm, 8 mm and 10 mm is chosen for this study.

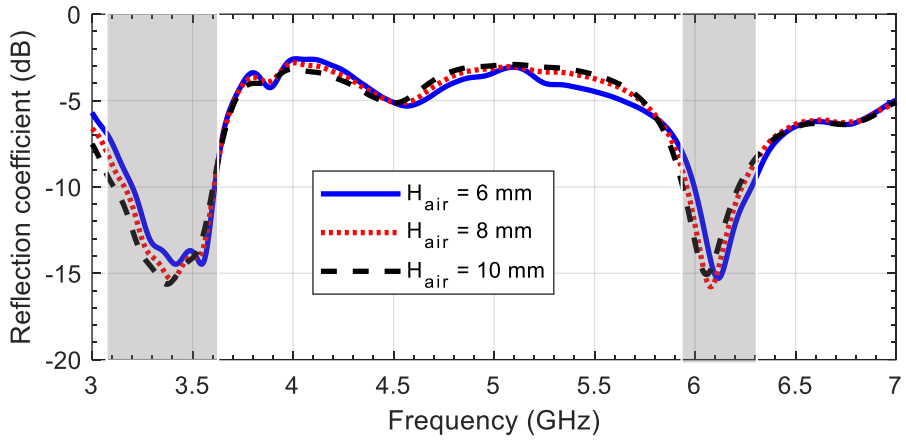

(a)

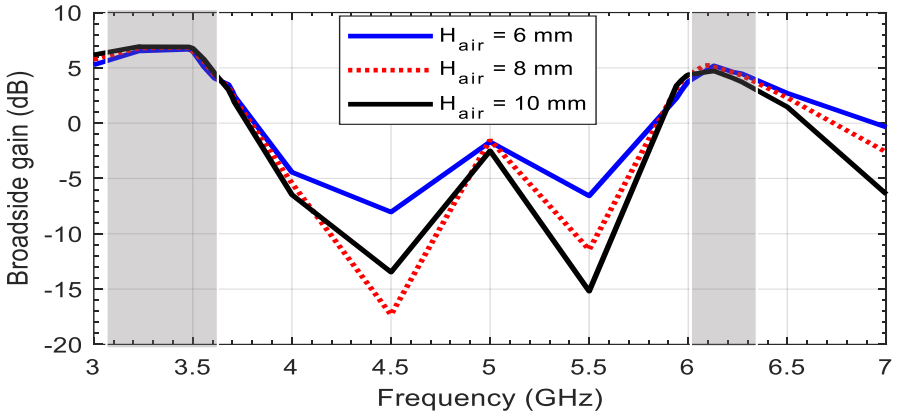

(b)

Figure 4.31: Effect of H_{air} on the antenna performances, (a) Reflection coefficient, (b) Realized gain.

It can be observed as H_{air} increased the impedance bandwidth tend to be wider in the first operating band. It is extended from 400 MHz to 500 MHz when H_{air} varies between 6 mm to 10 mm, respectively.
A steady bandwidth of almost 270 MHz is demonstrated across the second operating frequency with a shifted resonant frequency from 6.05 to 6.12 GHz for $H_{air} = 6$ mm, $H_{air} = 8$ mm and $H_{air} = 10$ mm.
The gain increases at both first and second resonant frequencies. At the first resonant frequency (3.40 GHz), a peak gains of 6.62 dB, 6.83 dB, and 6.90 dB is achieved for $H_{air} = 6$ mm, $H_{air} = 8$ mm, and $H_{air} = 10$ mm, respectively. Similarly, at the second resonant frequency, peak gains of 4.30 dB, 5.20 dB, and 4.69 dB are achieved for the same H_{air} values.
Finally , H_{air} of 8 mm is selected as optimal, demonstrating a balance between gain and overall thickness.

b AMC unit cell numbers

The effect of the AMC unit cell numbers on the antenna reflection coefficient and the broadside gain is illustrated in Figure 4.32. It is worth to point out that number of the unit cell will be fixed in the Y direction to 3 lines and variable in the x direction (column) to simplify the manufacturing process (assembling the antenna and AMC reflector). Therefore, 3×3, 3×5, and 3×7 unit cells configuration are selected in this study. It can be seen from Figure.34(a), that the effect of the unit cell number on the reflection coefficient is less significant with almost the same bandwidth for all cases.
The gain is increased as the number of the unit cell increased in the x direction.
For configuration of 3×3 unit cell, a peaks gain of 5.5 dB can be achieved over the first operating band but it decrease deeply to 2 dB over the second operating band. For configuration of 3×5 unit cell, a peak gains of 6.83 dB and 5.20 dB are achieved at the two resonant frequencies, respectively. For configuration of 3×7 unit cell,a peaks gain of 6.60 dB and 5.50 dB centred at the two resonant frequencies, respectively.
Finally, 3×5 unit cell configuration is chosen as an optimum design parameter for enhancing the antenna gain and size. The final optimised dimensions of the proposed dual-band monopole antenna over the modified dual-band AMC reflector are summarised in Table 4.7.

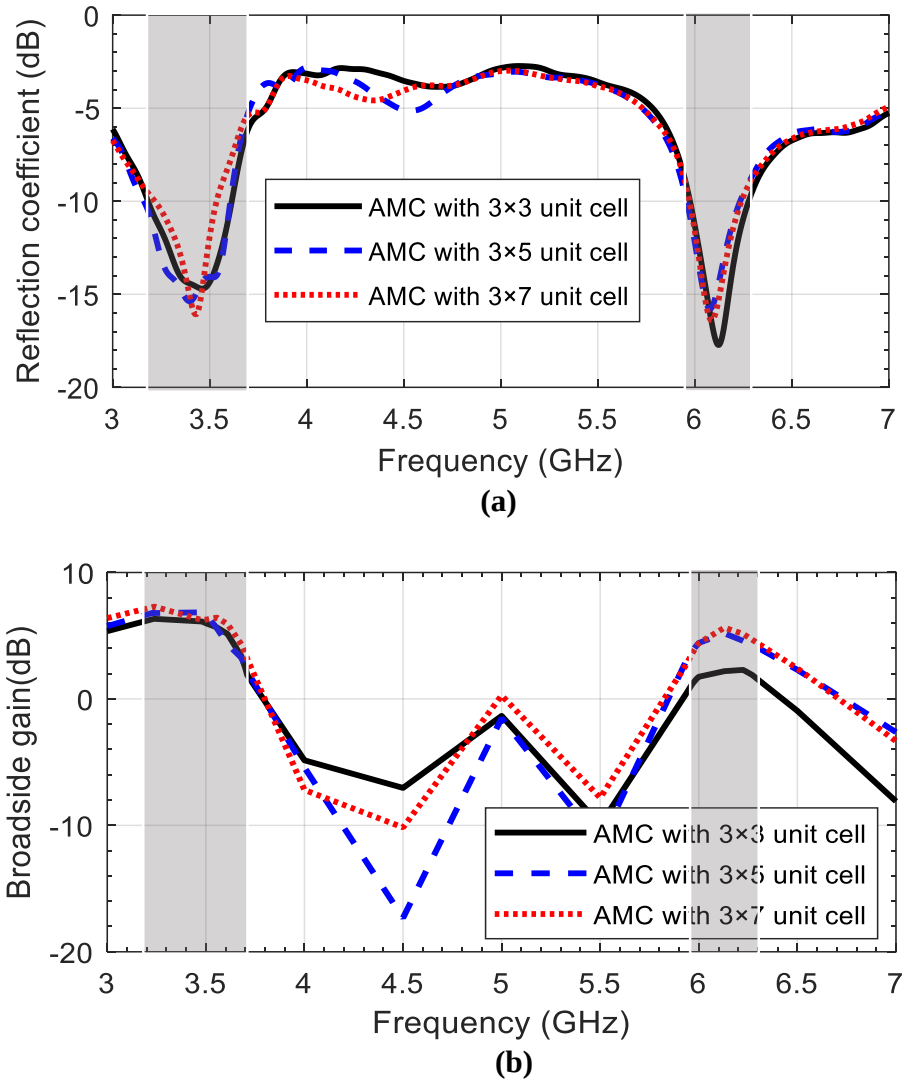

Figure 4.32: Effect of the modified dual-band AMC unit cell numbers on the antenna characteristics, (a) Reflection coefficient, (b) Realized Gain.

Table 4.7: Dimensions of the dual-band antenna laded with the dual-band AMC reflector

Parameter	L_S	W_S	L_P	W_P	L_{P1}	L_{P2}	W_{P1}	W_{P2}
Value (mm)	50	50	27	20	25.6	22.8	18.6	15.8
Parameter	T	W_g	L_f	W_f	H_1	H_2	H_{air}	Gap
Value (mm)	0.3	10	15	2.39	1.6	3.2	8	1.1

4.3.4 Proposed structure contribution

Finally, a comparison between the proposed work and other recently published works is listed in Table 4.8. The proposed dual-band monopole antenna, based on the modified dual-band AMC reflector, exhibits the highest gain enhancement of 11 dB with shorter distance ($0.09\lambda_L$) between the antenna and AMC reflector compared to [93, 97]. It is seen that the antennas designed in [92] and [107] have shorter distances between the antenna and their reflectors, but they demonstrate lower gain enhancement compared to our design.
The proposed configuration can exhibit two frequency bands in the range of (3,16-3,60) GHz and (6,96-6,23) GHz centred at 3.40 and 6.10 GHz with an enhanced directional gain of 6.83 and 5.20 dB Respectively which cover sub 6 GHz (n78) and sub 7GHz (n96) 5G applications.

Table 4.8: Comparison between the proposed and other similar works

Ref	AMC size (mm^2)	No.of band	H_{air} (mm)	Freq (GHz)	peak Gain (dB)	Max gain enhancement
[92]	90×90	3	3 ($0.04\lambda_L$)	2.4, 3.5, 5.5	4.8, 5.1, 6.2	3
[93]	90 × 90	3	23 ($0.19\lambda_L$)	2.45, 3.5, 4.6, 5.8	/	5.54
[97]	45×60	3	30.5 ($0.25\lambda_L$)	2.4, 2.5, 3.5, 5.5, 5.8	5.8, 5.53, 4.49,6.45 6.49	6.44
[106]	104×104	2	8 ($0.09\lambda_L$)	2.4, 5.2	7.2, 7.3	2.88
[107]	75×50	3	2 ($0.04\lambda_L$)	2.45, 5.8	8, 9	3
[108]	80×80	2	8 ($0.064\lambda_L$)	2.45, 5.8	5, 7.5	4.5
This work	64.9×50	2	8 ($0.09\lambda_L$)	3.40, 6.10	6.83, 5.20	11.12

H_{air} is the sapce between the antenna and the AMC reflector.

4.4 Conclusion

In this chapter, the effectiveness of employing a multiband Artificial Magnetic Conductor (AMC) reflector has been investigated for the purposes of miniaturization, reduction of backward radiation, and gain enhancement.
In the first application,a trap-loaded pyramidal antenna loaded with triband AMC reflector is suggested. The results indicate that by replacing the previous bulky cutoff open-ended waveguide with a triband AMC reflector, a substantial reduction in the overall antenna size while concurrently maintaining lower levels of backward radiation. The reduction encompasses a 37% decrease along both the x and y-axes, coupled with a remarkable 67% reduction along the z-axis. The antenna prototype has been fabricated and tested. Both simulation and experimental results indicate that the proposed structure has quasi-hemispheric radiation pattern. The measured directivity levels of 5.12 dB, 6.60 dB, and 7 dB are accompanied by significant backward radiation values of -8 dB, -14 dB, and -12.6 dB at the three resonant frequencies 1.197 GHz, 1.575 GHz, and 2.245 GHz, respectively. While for the second application, A dual-band monopole antenna associated with dual-band artificial magnetic conductor (AMC) reflector is presented for 5G application (sub 6 GHz (n78)-sub 7 GHz (n96)). The AMC reflector is loaded on the back of the antenna structure as reflector for gain enhancement. Indeed a significant gain enhancement is achieved over the two operating bands. The multiband AMC surface demonstrates its ability to enhance the antenna performances which make it useful in several applications.

General conclusion

This thesis focuses on leveraging the properties of wideband and multiband artificial reflectors to design novel antenna structures. The aim of employing the artificial reflectors is to address key challenges in antenna performances, such as improving gain, expanding bandwidth, achieving miniaturization, and reducing backward radiation. The selection of the AMC forms is based on surface current methodology, which plays a crucial role in preventing performance degradation, particularly in terms of radiation.

The first chapter introduces several designs of wideband and multiband antennas, along with their methodologies for achieving wideband and multiband characteristics. It discusses their types used for aerospace applications and explores feeding techniques used to feed microstrip antennas, examining their advantages and disadvantages. Through this exploration, we gain insights into the impact of different parameters, including antenna geometry, feeding technique, and radiation pattern diagram. This analysis enable the identification and selection of optimal parameters for enhancing overall performance.

The second chapter presents the concept of artificial reflectors, and outlines the principal analytical and numerical methods employed for modeling and characterizing these surfaces. Additionally, a comprehensive review of antennas based on wideband and multiband artificial reflectors is conducted to identify diverse geometries and investigate characteristics used in this field. This review also facilitates the comparison of the findings with existing work, proving the effectiveness of the design.

The third chapter presents the efficacy of AMC surfaces when employed as reflectors for wideband antennas, with a specific focus on their potential advantages in stabilizing gain, reducing the antenna profile height, and enhancing the front-to-back ratio. By studying the surface current distribution on AMC surfaces, we effectively stabilized the

bowtie antenna gain, achieving a stable gain with a minimal variation of 0.85 dB across a wide bandwidth of 50%. Furthermore, our investigation revealed the application of AMC surfaces in reducing the antenna profile height and improving the front-to-back ratio of UHF-RFID reader antennas. By integrating AMC surfaces as reflectors, we successfully achieved a substantial reduction in antenna profile, corresponding to a 45% reduction, with high measured gain and a front-to-back ratio of more than 5 dB and 24 dB across the entire UHF-RFID band, respectively.

The fourth chapter presents the efficacy of AMC surfaces for multiband antennas, focusing on their potential advantages in miniaturization, reducing backward radiation, and enhancing gain across multiple operating bands. A trap-loaded pyramidal antenna backed with a triband artificial magnetic conductor is designed for the GNSS system (GPS/GALILEO/MicroSat). By integrating a triband AMC reflector with a conventional multiband pyramidal antenna, we achieved a significant reduction in overall antenna size by 37%, 37%, and 67% along the x, y, and z-axes, respectively, while maintaining similar radiation performance. This integration also enhances gain across multiple operating bands. Therefore, a dual-band AMC reflector is introduced at the back of a dual-band monopole antenna for 5G communication. This design resulted in significantly enhanced directional gains of 6.83 dB and 5.20 dB centered at the two operating frequencies of 3.40 GHz and 6.10 GHz, respectively.

Antenna prototypes have been simulated using CST Microwave Studio software, fabricated, and measured, confirming their proper operation. Moreover, the obtained results were compared to similar published works, demonstrating highly attractive performances of the AMC reflector for several application. As future perspectives of this thesis, we propose:

- Explore the concept of reconfigurable AMC surfaces by adding lumped capacitors or varactor diodes in a unit cell design to flexibly manipulate the working frequency and bandwidth of the AMC.
- Develop mathematical models of AMC surfaces, especially multiband AMC surfaces in order to facilitate the design of these structures.

Bibliography

[1] G. Kumar and K. Ray. *Broadband microstrip antennas*. Artech house, 2002.

[2] Constantine A Balanis. *Antenna theory: analysis and design*. John wiley & sons, 2016.

[3] Georges A Deschamps. Microstrip microwave antennas. In *Proceedings of the Third Symposium on the USAF Antenna Research and Development Program, Oct*, pages 18–22, 1953.

[4] R. Munson and J. Krutsinger. Single slot cavity antenna assembly, January 23 1973. US Patent 3,713,162.

[5] RJIT Munson. Conformal microstrip antennas and microstrip phased arrays. *IEEE Transactions on Antennas and propagation*, 22(1):74–78, 1974.

[6] J Howell. Microstrip antennas. *IEEE Transactions on Antennas and Propagation*, 23(1):90–93, 1975.

[7] Zhi Ning Chen and Michael Yan Wah Chia. *Broadband planar antennas: design and applications*. John Wiley & Sons, 2006.

[8] X Begaud et al. *Ultra wide band antennas*. Wiley Online Library, 2011.

[9] K. Jung, R.L. Campbell, P. Hanaway, M.F. Andrews, C. McCuen, W.R. Eisenstadt, and R.M. Fox. Marchand balun embedded probe. *IEEE transactions on microwave theory and techniques*, 56(5):1207–1214, 2008.

[10] K.M.P. Aghdam, R. Faraji-Dana, and J. Rashed-Mohassel. Optimization of microstrip tapered balun for sinuous antenna feeding circuits. In *2004 10th International Symposium on Antenna Technology and Applied Electromagnetics and URSI Conference*, pages 1–4. IEEE, 2004.

[11] Y.G. Kim, D.s. Woo, K. W. Kim, and Y.K. Cho. A new ultra-wideband microstrip-to-CPS transition. In *2007 IEEE/MTT-S International Microwave Symposium*, pages 1563–1566. IEEE, 2007.

[12] T. Huynh and K.F. Lee. Single-layer single-patch wideband microstrip antenna. *Electronics letters*, 31(16):1310–1312, 1995.

[13] A. Mirkamali, P.S. Hall, and M. Soleimani. Elliptical multiple-ring monopole antennas. *Microwave and Optical Technology Letters*, 48(1):4–8, 2006.

[14] Y.T. Liu, S.W. Su, C.L. Tang, H.T. Chen, and K.L. Wong. On-vehicle low-profile metal-plate antenna forAMPS/GSM/DCS/PCS/UMTS multiband operations. *Microwave and Optical Technology Letters*, 41(2):144–146, 2004.

[15] Y.S. Liu, J.S. Sun, R.H. Lu, and Y.J. Lee. New multiband printed meander antenna for wireless applications. *Microwave and optical technology letters*, 47(6):539–543, 2005.

[16] P. Erätuuli, P. Haapala, and P. Vainikainen. Dual frequency wire antennas. *Electronics Letters*, 32(12):1051–1052, 1996.

[17] F. Ferrero, C. Luxey, G. Jacquemod, and R. Staraj. Dual-band circularly polarized microstrip antenna for satellite applications. *IEEE Antennas and Wireless Propagation Letters*, 4:13–15, 2005.

[18] D.M. Pozar and S.M. Duffy. A dual-band circularly polarized aperture-coupled stacked microstrip antenna for global positioning satellite. *IEEE transactions on antennas and propagation*, 45(11):1618–1625, 1997.

[19] J. Anguera, G. Font, C. Puente, C. Borja, and J. Soler. Multifrequency microstrip patch antenna using multiple stacked elements. *IEEE microwave and wireless components letters*, 13(3):123–124, 2003.

[20] K.L. Lau and K.M. Luk. A wide-band circularly polarized L-probe coupled patch antenna for dual-band operation. *IEEE transactions on antennas and propagation*, 53(8):2636–2644, 2005.

[21] C.S. Lee, V. Nalbandian, and F. Schwering. Planar dual-band microstrip antenna. *IEEE transactions on antennas and propagation*, 43(8):892–894, 1995.

[22] T. Taga and K. Tsunekawa. Performance analysis of a built-in planar inverted F antenna for 800 mhz band portable radio units. *IEEE Journal on Selected Areas in Communications*, 5(5):921–929, 1987.

[23] Pascal Ciais. *Antennes multistandards pour communications mobiles*. PhD thesis, Nice, 2004.

[24] P. Le Thuc. *Antennes imprimées miniatures pour systèmes de télécommunications: applications aux communications mobiles*. PhD thesis, Nice, 2003.

[25] C.R. Rowell and R.D. Murch. A compact PIFA suitable for dual-frequency 900/1800-mhz operation. *IEEE Transactions on antennas and propagation*, 46(4):596–598, 1998.

[26] Y.X. Guo, I. Ang, and M.Y.W. Chia. Compact internal multiband antennas for mobile handsets. *IEEE Antennas and Wireless Propagation Letters*, 2:143–146, 2003.

[27] J.S. Row. Dual-frequency triangular planar inverted-F antenna. *IEEE transactions on antennas and propagation*, 53(2):874–876, 2005.

[28] K.L. Wong and K.P. Yang. Modified planar inverted-F antenna. *Electronics letters*, 34(1):7–8, 1998.

[29] P.S. Liu, Z.D.and Hall and D. Wake. Dual-frequency planar inverted-F antenna. *IEEE Transactions on antennas and propagation*, 45(10):1451–1458, 1997.

[30] J.Y. Dauvignaca L. Zaid, G. Kossiavas, J. Cazajous, and A. Papiemik. Dual-frequency and broad-band antennas with stacked quarter wavelength elements. *IEEE Transactions on Antennas and Propagation*, 47(4):654–660, 1999.

[31] C.W. Chiu and F.L. Lin. Compact dual-band PIFA with multi-resonators. *Electronics Letters*, 38(12):538–540, 2002.

[32] G.K.H. Lui and R.D. Murch. Compact dual-frequencyPIFA designs using lc resonators. *IEEE Transactions on Antennas and Propagation*, 49(7):1016–1019, 2001.

[33] C. Puente Baliarda, J. Romeu Robert, R. Pous Andrés, X. Garcia, and F. Benitez. Fractal multiband antenna based on the sierpinski gasket. *Electronics Letters*, 32(1):1–2, 1996.

[34] S. Wong and B.L. Ooi. Analysis and bandwidth enhancement of sierpinski carpet antenna. *Microwave and optical technology letters*, 31(1):13–18, 2001.

[35] J. Chang, S. Jung, and S. Lee. Triangular fractal antenna. *Microwave and optical technology letters*, 27(1):41–46, 2000.

[36] J.C. Liu, D.C. Chang, D. Soong, C.H. Chen, C.Y. Wu, and L. Yao. Circular fractal antenna approaches with descrates circle theorem for multiband/wideband applications. *Microwave and optical technology letters*, 44(5):404–408, 2005.

[37] K. Siakavara and F. Tsaldaris. A multi-wideband microstrip antenna designed by the square-curve fractal technique. *Microwave and Optical Technology Letters*, 41(3):180–185, 2004.

[38] D.R. Newcomb. Multi-band vertical antenna. *United Patent Official Gazette[U. S. PAT. OFF. GAZ.]*,, 998(2):726, 1980.

[39] H.K. Morgan. Multifrequency tuned antenna system. *Electronics, vol*, 1940.

[40] D. Lamensdorf and M.A. Smolinski. Dual-band quadrifilar helix antenna. In *IEEE Antennas and Propagation Society International Symposium (IEEE Cat. No. 02CH37313)*, volume 3, pages 488–491. IEEE, 2002.

[41] J.P. Gianvittorio and Y. Rahmat-Samii. Fractal yagi antennas: Design, simulation, and fabrication. *Microwave and optical technology letters*, 41(5):375–380, 2004.

[42] B. Rama Rao, M.A. Smolinski, C.C. Quach, and E.N. Rosario. Triple-band GPS trap-loaded inverted l antenna array. *Microwave and Optical Technology Letters*, 38(1):35–37, 2003.

[43] W.A. Imbriale and L. Boccia. *Space Antenna Handbook*. Wiley Online Library, 2012.

[44] Surrey satellite technology ltd. home page. http://www.sstl.co.uk,accessed June 3, 2024.

[45] S. Gao, K. Clark, M. Unwin, J. Zackrisson, W.A. Shiroma, J.M. Akagi, K. Maynard, P. Garner, L. Boccia, G. Amendola, et al. Antennas for modern small satellites. *IEEE Antennas and Propagation Magazine*, 51(4):40–56, 2009.

[46] T. Macnamara. *Introduction to antenna placement and installation.* John Wiley & Sons, 2010.

[47] M. Saravanan and M.J.S. Rangachar. A novel rectangular patch antenna with double L-probe fed for radar altimeter application. In *2016 International Conference on Wireless Communications, Signal Processing and Networking (WiSPNET)*, pages 1777–1780. IEEE, 2016.

[48] M. Grelier. *Miniaturisation des antennes large bande à l'aide de matériaux artificiels.* PhD thesis, Télécom ParisTech, 2011.

[49] B. A. Munk. *Frequency selective surfaces: theory and design.* John Wiley & Sons, 2005.

[50] J. B. Pendry, A.J. Holden, W.J. Stewart, and I. Youngs. Extremely low frequency plasmons in metallic mesostructures. *Physical review letters*, 76(25):4773, 1996.

[51] J.B. Pendry, A.J. Holden, D.J. Robbins, and W.J. Stewart. Magnetism from conductors and enhanced nonlinear phenomena. *IEEE transactions on microwave theory and techniques*, 47(11):2075–2084, 1999.

[52] D.R. Smith, W.J. Padilla, D.C. Vier, S.C Nemat-Nasser, and S. Schultz. Composite medium with simultaneously negative permeability and permittivity. *Physical review letters*, 84(18):4184, 2000.

[53] V.G. Veselago. The electrodynamics of substances with simultaneously negative values of ε and μ. *Soviet Physics Uspekhi*, 10(4):509–514, 1968.

[54] J. B. Pendry. Negative refraction makes a perfect lens. *Physical review letters*, 85(18):3966, 2000.

[55] D. Schurig, J. Mock, B.J. Justice, J.b. Cummer, S.and Pendry, A. Starr, and D. Smith. Metamaterial electromagnetic cloak at microwave frequencies. *Science*, 314(5801):977–980, 2006.

[56] D. Sievenpiper, L. Zhang, R.F.J Broas, N.G. Alexopolous, and E. Yablonovitch. High-impedance electromagnetic surfaces with a forbidden frequency band. *IEEE Transactions on Microwave Theory and techniques*, 47(11):2059–2074, 1999.

[57] F. Yang and Y. Rahmat-Samii. *Electromagnetic band gap structures in antenna engineering*. Cambridge university press Cambridge, UK, 2009.

[58] E. Yablonovitch. Inhibited spontaneous emission in solid-state physics and electronics. *Physical review letters*, 58(20):2059, 1987.

[59] M. Abegaonkar, L. Kurra, and S.K. Koul. *Printed resonant periodic structures and their applications*. CRC Press, 2016.

[60] M Rahman and MA Stuchly. Transmission line–periodic circuit representation of planar microwave photonic bandgap structures. *Microwave and optical technology letters*, 30(1):15–19, 2001.

[61] T. Weiland. Time domain electromagnetic field computation with finite difference methods. *International Journal of Numerical Modelling: Electronic Networks, Devices and Fields*, 9(4):295–319, 1996.

[62] A. Taflove, SC Hagness, and M. Piket-May. Computational electromagnetics: the finite-difference time-domain method. *The Electrical Engineering Handbook*, 3(629-670):15, 2005.

[63] K. Yee. Numerical solution of initial boundary value problems involving maxwell's equations in isotropic media. *IEEE Transactions on antennas and propagation*, 14(3):302–307, 1966.

[64] M.Z. Azad and M. Ali. Novel wideband directional dipole antenna on a mushroom like EBG structure. *IEEE Transactions on antennas and propagation*, 56(5):1242–1250, 2008.

[65] G.M. Zhong, Y.W.and Yang and L.R. Zhong. Gain enhancement of bow-tie antenna using fractal wideband artificial magnetic conductor ground. *Electronics Letters*, 51(4):315–317, 2015.

[66] A.P. Volkov, V.V. Kakshin, I.Y. Ryzhov, K.V. Kozlov, and A.Y. Grinev. Wideband low-profile dual-polarized antenna with AMC reflector. *Progress in Electromagnetics Research Letters*, 88:15–20, 2020.

[67] X. Li, Y.C. Jiao, and L. Zhang. Wideband low-profile CPW-fed slot-loop antenna using an artificial magnetic conductor. *Electronics Letters*, 54(11):673–674, 2018.

[68] A. Foroozesh and L. Shafai. Investigation into the application of artificial magnetic conductors to bandwidth broadening, gain enhancement and beam shaping of low profile and conventional monopole antennas. *IEEE Transactions on Antennas and Propagation*, 59(1):4–20, 2010.

[69] Y. Murakami, T. Hori, and M. Fujimoto. Optimum reflector configuration for dipole antenna by using artificial magnetic conductor. In *2013 International Workshop on Antenna Technology (iWAT)*, pages 277–280. IEEE, 2013.

[70] Y. Murakami, T. Hori, and M. Fujimoto. Optimum design of dipole antenan with amc reflector. In *2014 IEEE Antennas and Propagation Society International Symposium (APSURSI)*, pages 813–814. IEEE, 2014.

[71] C. Joshi, A.C. Lepage, J. Sarrazin, and X. Begaud. Enhanced broadside gain of an ultrawideband diamond dipole antenna using a hybrid reflector. *IEEE Transactions on Antennas and Propagation*, 64(7):3269–3274, 2016.

[72] D. Chen, W. Yang, Q. Xue, and W. Che. A wideband low-profile antenna using hybrid metasurface structure. *Microwave and Optical Technology Letters*, 63(3):965–969, 2021.

[73] Qizhou Che, Dongxu Chen, and Wenquan Che. A miniaturized wideband antenna using hybrid L/T-shaped metasurface structure. *Microwave and Optical Technology Letters*, 63(8):2186–2191, 2021.

[74] M. Li, Q.L. Li, B.o. Wang, C.F. Zhou, and S.W. Cheung. A low-profile dual-polarized dipole antenna using wideband AMC reflector. *IEEE Transactions on Antennas and Propagation*, 66(5):2610–2615, 2018.

[75] J. Yeo and D. Kim. Design of a wideband artificial magnetic conductor (AMC) ground plane for low-profile antennas. *Journal of Electromagnetic Waves and Applications*, 22(16):2125–2134, 2008.

[76] R.M. Mateos, C. Craeye, and G. Toso. High-gain wideband low-profile antenna. *Microwave and Optical Technology Letters*, 48(12):2615–2619, 2006.

[77] B. Zhang, P. Yao, and J. Duan. Gain-enhanced antenna backed with the fractal artificial magnetic conductor. *IET Microwaves, Antennas & Propagation*, 12(9):1457–1460, 2018.

[78] A. Mohanty and S. Sahu. Compact wideband hybrid fractal antenna loaded on AMC reflector with enhanced gain for hybrid wireless cellular networks. *AEU-International Journal of Electronics and Communications*, 138:153837, 2021.

[79] D. Feng, H. Zhai, L. Xi, S. Yang, K. Zhang, and D. Yang. A broadband low-profile circular-polarized antenna on an AMC reflector. *IEEE Antennas and Wireless Propagation Letters*, 16:2840–2843, 2017.

[80] Z.D. Wang, S. Huang, J.L. Liu, Z.L. Lv, and X.B. Tang. A low profile wideband linearly polarized slot antenna using a circular AMC surface. In *2020 9th Asia-Pacific Conference on Antennas and Propagation (APCAP)*, pages 1–2. IEEE, 2020.

[81] H.Q. Xiong, C.J. Zhang, and M.S. Tong. Wideband low-profile dual-polarized antenna based on a gain-enhanced EBG reflector. *IEEE Transactions on Components, Packaging and Manufacturing Technology*, 12(2):391–394, 2021.

[82] H. Malekpoor and M. Shahraki. Printed slot antenna fed by CPW supported by broadband planar artificial magnetic conductor with enhanced features. *Journal of Communications Technology and Electronics*, 67(4):375–386, 2022.

[83] M. Rahman and M.A. Stuchly. Circularly polarised patch antenna with periodic structure. *IEE Proceedings-Microwaves, Antennas and Propagation*, 149(3):141–146, 2002.

[84] D. Qu, L. Shafai, and A. Foroozesh. Improving microstrip patch antenna performance using EBG substrates. *IEE Proceedings-Microwaves, Antennas and Propagation*, 153(6):558–563, 2006.

[85] M. Ameen, A. Mishra, and R.K. Chaudhary. Dual-band CRLH-TL inspired antenna loaded with metasurface for airborne applications. *Microwave and Optical Technology Letters*, 63(4):1249–1256, 2021.

[86] Z. Duan, J. Rui, L.J. Xu, and G. Wen. A low-profile dual-band dual-polarized tightly spaced antenna array with artificial magnetic conductor surface for 5G micro base station application. *International Journal of RF and Microwave Computer-Aided Engineering*, 32(7):e23192, 2022.

[87] Q. Liu, H. Liu, W. He, and S. He. A low-profile dual-band dual-polarized antenna with an amc reflector for 5G communications. *IEEE Access*, 8:24072–24080, 2020.

[88] S. Zhu and R. Langley. Dual-band wearable antennas over EBG substrate. *Electronics Letters*, 43(3):1, 2007.

[89] M.E. de Cos and F. Las-Heras. Dual-band uniplanar CPW-fed monopole/EBG combination with bandwidth enhancement. *IEEE Antennas and Wireless Propagation Letters*, 11:365–368, 2012.

[90] S. Roy and U. Chakraborty. Metamaterial-embedded dual wideband microstrip antenna for 2.4 GHz WLAN and 8.2 GHz ITU band applications. *Waves in Random and Complex Media*, 30(2):193–207, 2020.

[91] A. Badisa, B.T.P. Madhav, K. Srilatha, M.C. Rao, and S. Das. A circularly polarized quad-band wearable textile antenna integrated with triple band AMC reflector for wban applications. *Progress In Electromagnetics Research C*, 121:1–18, 2022.

[92] J. Lai, J. Wang, W. Sun, R. Zhao, and H. Zeng. A low profile artificial magnetic conductor based tri-band antenna for wearable applications. *Microwave and Optical Technology Letters*, 64(1):123–129, 2022.

[93] Y. Gong, S. Yang, B. Li, Y. Chen, F. Tong, and C. Yu. Multi-band and high gain antenna using AMC ground characterized with four zero-phases of reflection coefficient. *IEEE Access*, 8:171457–171468, 2020.

[94] V. Rajavel and D. Ghoshal. A compact triband antenna using artificial magnetic conductor for wireless body area network communicationsfront. *Wireless Networks*, pages 1–23, 2023.

[95] S. Yang, C. Yu, X. Yang, and J. Zhao. A tri-band flexible antenna based on tri-band AMC reflector for gain enhancement and SAR reduction. *AEU-International Journal of Electronics and Communications*, 168:154715, 2023.

[96] J.J. Xie, Y.Z. Yin, J. Wang, and S.L. Pan. A novel tri-band circular slot patch antenna with an EBG structure for WLAN/WiMAX applications. *Journal of Electromagnetic Waves and Applications*, 26(4):493–502, 2012.

[97] C. Yu, S. Yang, Y. Chen, and D. Zeng. Radiation enhancement for a triband microstrip antenna using an AMC reflector characterized with three zero-phases in reflection coefficient. *Journal of Electromagnetic Waves and Applications*, 33(14):1846–1859, 2019.

[98] Rafael Gonçalves Licursi de Mello, Anne Claire Lepage, and Xavier Begaud. A low-profile, triple-band, and wideband antenna using dual-band AMC. *Sensors*, 23(4):1920, 2023.

[99] A. Soliman, D. Elsheakh, E. Abdallah, and H. El-Henawy. CPW fed planar PIFA with applied electromagnetic band-gap ground plane. In *2013 IEEE Antennas and Propagation Society International Symposium (APSURSI)*, pages 282–283. IEEE, 2013.

[100] A. Fattouche, L. Mouffok, S. Hebib, and M. Bitchikh. A compact wideband antenna with an integrated balun. In *2020 XXXIIIrd General Assembly and Scientific Symposium of the International Union of Radio Science*, pages 1–4. IEEE, 2020.

[101] K. Boumaaza, S. Hebib, Y. Bennani, and L. Mouffok. Broadband U-slot patch antenna for RFID-UHF reader. In *2019 International Conference on Advanced Electrical Engineering (ICAEE)*, pages 1–4. IEEE, 2019.

[102] F. Yang, K. Ma, Y. Qian, and T. Itoh. A uniplanar compact photonic-bandgap (UC-PBG) structure and its applications for microwave circuit. *IEEE Transactions on microwave theory and techniques*, 47(8):1509–1514, 1999.

[103] S. Hebib, H. Aubert, O. Pascal, N. Fonseca, L. Ries, and J. Lopez. Multiband pyramidal antenna loaded with a cutoff open-ended waveguide. *IEEE Transactions on Antennas and Propagation*, 57(1):266–270, 2009.

[104] A. Fattouche, L. Mouffok, S. Hebib, and A. Mansoul. A triple band artificial magnetic conductor: design & analytical model. *Progress In Electromagnetics Research Letters*, 104:161–168, 2022.

[105] S. Noor, M. Jusoh, T. Sabapathy, A. Rambe, H. Vettikalladi, A. M. Albishi, and M. Himdi. A patch antenna with enhanced gain and bandwidth for Sub-6 GHz and sub-7 GHz 5G wireless applications. *Electronics*, 12(12):2555, 2023.

[106] H. Zhai, K. Zhang, S. Yang, and D. Feng. A low-profile dual-band dual-polarized antenna with an AMC surface for WLAN applications. *IEEE Antennas and Wireless Propagation Letters*, 16:2692–2695, 2017.

[107] A. Mersani, L. Osman, and J. Ribero. Performance of dual-band AMC antenna for wireless local area network applications. *IET Microwaves, Antennas & Propagation*, 12(6):872–878, 2018.

[108] M. Abdelghany, M. Fathy Abo Sree, A. Desai, and A. Ibrahim. Gain improvement of a dual-band CPW monopole antenna for sub-6 GHz 5G applications using AMC structures. *Electronics*, 11(14):2211, 2022.

[109] Starlab MVG system datasheet. URL: https://www.keysight.com/us/en/assets/9018-61222/brochures/9018-61222.pdf, accessed june 3,2024.

[110] L. Duchesne, P. Garreau, N. Robic, A. Gandois, P. Iversen, and G. Barone. Compact multi-probe antenna test station for rapid testing of antennas and wireless terminals. In *2004 IEEE 15th International Symposium on Personal, Indoor and Mobile Radio Communications (IEEE Cat. No. 04TH8754)*, volume 1, pages 632–636. IEEE, 2004.

[111] S. Hebib. *Nouvelle topologie d'antennes multi-bandes pour applications spatiales*. PhD thesis, Université Paul Sabatier-Toulouse III, 2008.

Appendix A

Antenna characteristics

The IEEE Standard Definitions of Terms for Antennas (IEEE Std 145–1983) define an antenna or aerial as a device used for transmitting or receiving radio waves. Essentially, the antenna serves as a connection point between free space and a guiding device. The guiding device, typically in the form of a coaxial cable or a waveguide, facilitates the transfer of electromagnetic energy between the transmitting source and the antenna, or between the antenna and the receiver. When energy flows from the source to the antenna, the setup is referred to as a transmitting antenna, whereas when the energy is received by the antenna from the environment, it is termed a receiving antenna [2].
Before exploring the antenna design and performance, it is crucial to establish a clear understanding of the fundamental characteristics that define an antenna's behavior. These characteristics provide valuable insights into how an antenna interacts with electromagnetic waves and performs its intended function. In this context, we will explore some of the most prominent antenna characteristics, including the radiation pattern, directivity, efficiency, gain, polarization, input impedance, reflection coefficient, and bandwidth. Understanding these characteristics is essential for engineers and researchers in optimizing antenna performances for various applications.

A.1 Radiation pattern

An antenna radiation pattern, also known as an antenna pattern, is defined as a mathematical function or a graphical representation of the radiation properties of the antenna as a function of space coordinates. In most cases, the radiation pattern is

determined in the far-field region and it is represented as a function of the directional coordinates [2]. Various part of a radiation pattern are often referred to as lobes, which can be further classified into major or main lobes, minor lobes, side lobes, and back lobes. Figure A.1 and Figure A.2, illustrate a symmetrical three-dimensional, two dimensional polar pattern, respectively, featuring multiple radiation lobes.

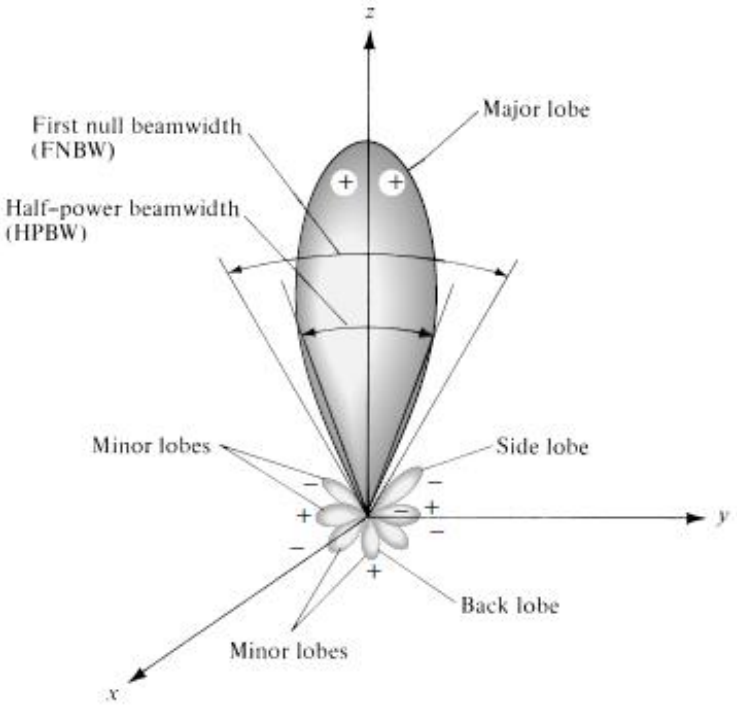

Figure A.1:3D Radiation pattern.

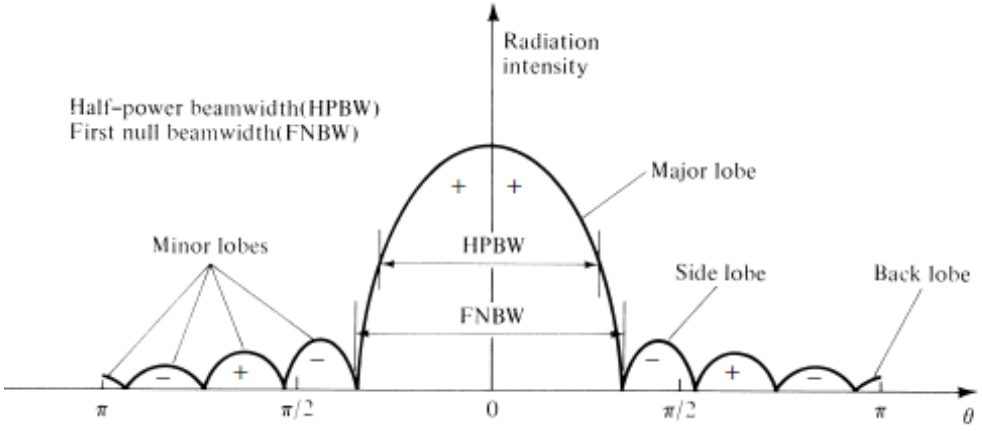

Figure A.2: 2D Radiation pattern.

It can be observed that the radiation pattern consists of multiple lobes [2] , including:
• Major lobe: also known as the main beam, is defined as "the radiation lobe containing the direction of maximum radiation. In Figure A.2, the major lobe is pointing in the direction of $\theta = 0°$.
• Minor lobe: is any lobe except a major lobe. All the lobes with the exception of the major lobe can be classified as minor lobes as it is indicated in Figure A.1 and Figure A.2.
• Side lobe: defined as a radiation lobe in any direction other than the intended lobe typically, it is adjacent to the main lobe.
• Back lobe: defined as a radiation lobe whose axis makes an angle of approximately 180° with respect to the main beam of an antenna. (which mean direction opposite to that of the major lobe) while front-to-back ratio is defined as the ratio of the power radiated in the main lobe (the forward direction) of the antenna to the power radiated in the opposite direction (the back lobe).
• Beamwidth : The beamwidth of a pattern is defined as the angular separation between two identical points on opposite sides of the pattern maximum. In an antenna pattern, there are several types of beamwidths including the Half-Power Beamwidth (HPBW), which is defined by IEEE as: the angle between the two directions in which the radiation intensity is half the value of the beam maximum. Another important beamwidth is the angular separation between the first nulls of the pattern, referred to as the First-Null Beamwidth (FNBW). Both the HPBW and FNBW are illustrated for the pattern in Figure A.1 and Figure A.2.

A.2 Directivity

The directivity of an antenna is defined as the ratio of the radiation intensity in a given direction from the antenna to the average radiation intensity over all directions, where the average radiation intensity is equal to the total power radiated by the antenna divided by 4 (which represents the average radiation intensity of an isotropic antenna). In mathematical form, is given in Equation (A.1) :

$$D = \frac{U}{U_0} = \frac{4\pi U}{P_{rad}} \tag{A.1}$$

U = radiation intensity (W/unit solid angle). U_0 = radiation intensity of isotropic source (W/unit solid angle) and P_{rad} = total radiated power (W).

A.3 Gain

The gain of an antenna, in a specific direction, is a measure of how well the antenna concentrates transmitted or received electromagnetic radiation in that direction compared to an ideal isotropic radiator. It refers to the ratio of the intensity, in a given direction, to the radiation intensity that would be obtained if the power accepted by the antenna were radiated isotropically. The radiation intensity corresponding to isotropic power is equal to the power accepted (input) by the antenna divided by 4π [2]. It can be expressed as:

$$Gain = 4\pi \frac{\text{Radiation intensity}}{\text{Total input (accepted) power}} = 4\pi \frac{U(\theta, \phi)}{P_{in}} \tag{A.2}$$

A.4 Efficiency

The determination of efficiency is one of the fundamental steps in quantifying the performance of an antenna. This parameter represents the amount of power actually radiated by the antenna compared to the input power to the same antenna. For a given direction, the ratio of antenna gain (G) to directivity (D) also gives the efficiency (η_{ray}) for that direction. It can be expressed as:

$$\eta_{ray} = \frac{G}{D} \tag{A.3}$$

A.5 Polarization

Based on [2], the polarization of an antenna in a particular direction refers to the polarization of the electromagnetic wave that is emitted or radiated by the antenna. The polarization of a radiated wave refers to the orientation of its electric field. It describes how the electric field vectors of the radiated wave are oriented in space as the wave propagates away from the antenna.

Polarization can be categorized as linear, circular, or elliptical. When the electric field vector at a point in space remains aligned along a straight line over time, the field is considered linearly polarized. However, in general, the path traced by the electric field vector forms an ellipse, resulting in elliptical polarization. Linear and circular polarizations are specific instances of elliptical polarization, occurring when the ellipse degenerates into a straight line or a circle, respectively. The direction of rotation of

the electric field vector is either clockwise (CW) or counterclockwise (CCW). Clockwise rotation corresponds to right-hand polarization, while counterclockwise rotation corresponds to left-hand polarization.

A.6 Input impedance

Input impedance is defined as the impedance presented by an antenna at its terminals, or the ratio of the voltage to current at a pair of terminals, or the ratio of the appropriate components of the electric to magnetic fields at a point. It can be expressed as [2]:

$$Z_A = R_A + jX_A \tag{A.4}$$

Z_A = antenna impedance at terminals (ohms).
R_A = antenna resistance at terminals (ohms): It represents a dissipation term. It is related, on one hand, to the radiated power and, on the other hand, to the power lost due to Joule heating.
X_A = antenna reactance at terminals (ohms): It is related to the reactive power stored in the vicinity of the antenna.

A.7 Bandwidth

The bandwidth of an antenna refers to the frequency range over which the antenna's performance meets a specified standard for various characteristics. the bandwidth can be understood as the range of frequencies, both above and below a center frequency where the antenna's characteristics (such as input impedance, radiation pattern, beamwidth, polarization, side lobe level, gain, beam direction, radiation efficiency) remain within an acceptable range of values compared to those at the center frequency.

Appendix B

MVG StarLab anechoic chamber overview

StarLab, designed for near-field analysis, provides a compact system for measuring electromagnetic fields in close proximity to the source, rather than in the far-field. The field radiated by the Device Under Test (DUT) is sampled using a probe array consisting of 15 wideband probes spaced evenly along the circumference of a circular support structure [109].

Figure B.1:MVG StarLab anechoic chamber [109].

1- Arch of probe array (choice of two probes can be interleaved (DP 400-6000 or DP 6000-18000).
2- DUT (Device Under Test) antenna.
3- Styrofoam or ultra-rigid mast (support).

The DUT is positioned at the center of the arch on top of a Styrofoam column, which is rotatable by a motor. This rotation enables the sampling of the radiated field over the entire sphere surrounding the DUT. The support structure for the probes has the capability to rotate around its center, facilitating measurements with any desired number of probes, allowing for oversampling of the radiated field.
To achieve a full-sphere measurement, the probe array is electronically scanned in elevation, while concurrently rotating the Device under Test (DUT) by 180° in azimuth (as illustrated in Figure B.1). This approach enables a rapid and comprehensive 3D measurement, capturing data across the entire spherical region around the DUT [109].

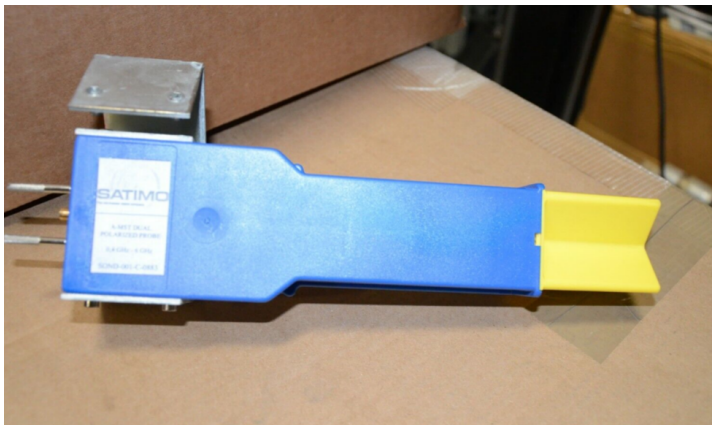

Figure B.2:SATIMO measurements Probe [110].

The StarLab system incorporates 15 probes that are evenly spaced along a circular arch with equal angular intervals. Each probe is equipped with a pair of orthogonal printed antennas, meticulously designed to exhibit broadband characteristics and deliver excellent performance across a wide frequency range. The two antennas within each probe are linearly polarized and aligned to represent vertical and horizontal polarizations. Importantly, these probes are fully reciprocal, meaning they can operate seamlessly in both receive and transmit modes. This reciprocal nature enhances their versatility, allowing for comprehensive measurements and analyses in various scenarios

[109]. A dedicated Satimo measurement probe [110] designed for StarLab is illustrated in Figure B.2, and its primary characteristics are outlined in Table B.1.

Table B.1: Main characteristics of Satimo wideband probe [110]

Item	**Specified performance**
Frequency band	0.8 GHz - 6.0 GHz 6.0 GHz - 18 GHz
VSWR	< 2.5
Typical gain	-10dBi
Cross polarisation dc-coupling	>30dB
Typical half beamwidth angle (-3dB)	45°

To mitigate issues related to scattering and reflections caused by the support structure and cabling, the arch is coated with multi-layer conformal absorbing material. This material is designed to absorb and dissipate electromagnetic waves, reducing undesired effects that could interfere with the accuracy of measurements. The use of conformal absorbing material enhances the performance of the probe array by minimizing external influences during the sampling of the electromagnetic field.

The StarLab test station is linked to a PC, which control all the equipment components such as the probe array, azimuth and elevation motors, RF source, and RF measurement devices utilizing a streamlined software environment known as SatEnv. This software not only manages the equipment but also handles the acquisition, post-processing, and visualization of measurement data. In real-time, the user has the ability to observe the radiation pattern of the tested device, expressed in terms of radiated power or gain. This includes immediate visualization through various formats, such as 1-D pattern cuts in Cartesian or polar representation, 2-D data plots, or 3-D data plots [109].

Table B.2: Main features of the MVG StarLab [109]

Technology	• Near-field / Spherical • Near-field / Cylindrica
Measurement capabilities	Gain, Directivity, Beamwidth Cross polar discrimination, Sidelobe levels 3D radiation pattern, Radiation pattern in any polarization (linear or circular), Antenna efficiency.
Frequency bands	• StarLab 6 GHz: 650 MHz to 6 GHz. • StarLab 18 GHz: 650 MHz to 18 GHz.
Max. size of DUT	45 cm for spherical set-up
Max. weight of DUT	10 kg with Styrofoam mast
Typical dynamic range	• 650 MHz - 6 GHz: 70 dB • 6 GHz - 18 GHz: 60 dB
Oversampling	Arch rotation
Software **Measurement control, data acquisition and post processing**	WaveStudio Near-field/far-field transform MV-Sphere

Appendix C

Directivity calculation of the 4 port circularly polarized antenna

The measurements taken in the MVG SatrLab provide the field in spherical coordinates, namely (E_θ, E_ϕ) (see Figure C.1): In order to replace the feeding circuit, digital processing of these measurements allows for considering the quadrature excitation of the different radiating elements. Its mean to appropriately phase shift the fields [111].

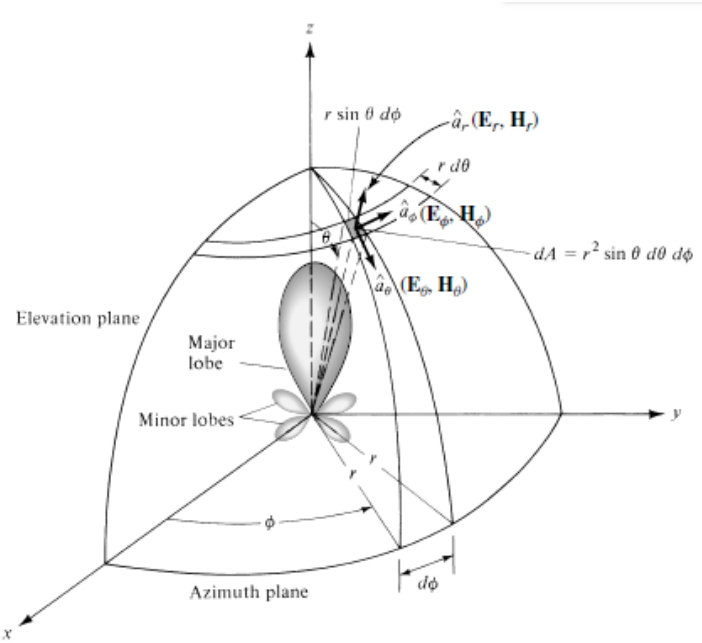

Figure C.1:The components E_θ and E_ϕ for a direction (θ, ϕ) [111].

Two cases are addressed in this thesis work. The first involves reconstructing the fields of the total antenna from the fields of a single element. This is mean to idealizing the

fabrication of feeding circuit and the antenna itself. For this purpose, it is essential to apply a sequential 90° rotation to the reference frame of the initial element to reconstruct the 4 elements. In the case of processing by ϕ cuts, this operation reduces to manipulations on matrices containing the different cuts in E_θ and E_ϕ. Once these manipulations are done, all that remains is to sum the various contributions of the phase corresponding to the excitation.
The second case involves reconstructing the fields from measurements of the 4 radiating elements. In this case, since the measurement frame is the same for all 4 elements, it is possible to immediately sum the fields provided in quadrature. Once the fields are reconstructed for the total antenna, we obtain circular polarization diagrams by applying the following formulas (C.1),(C.2) [111]:

$$E_{RHCP} = \frac{E_\theta + jE_\phi}{\sqrt{2}} \tag{C.1}$$

$$E_{LHCP} = \frac{E_\theta - jE_\phi}{\sqrt{2}} \tag{C.2}$$

While RHCP represents Right-Hand Circular Polarization and LHCP represents Left-Hand Circular Polarization.

The data obtained from measurements in the MVG StarLab are brut field values expressed in the spherical coordinate system. To facilitate comparison between diagrams, it is preferable to normalize them with respect to the same reference. Therefore, the diagrams presented in this thesis report are expressed in dB, normalized with respect to an isotropic equivalent source. The directivity is evaluated according to the formula (C.3) below [111]:

$$D(\theta,\phi) = \frac{|F(\theta,\phi)|^2}{\frac{1}{4\pi}\iint |F(\theta,\phi)|^2\, d\Omega} \tag{C.3}$$

where :|F(θ,ϕ)^2| It is the radiation pattern normalized with respect to the maximum radiation. This calculation involves the evaluation of a double integral. Some simplifying considerations will allow us to numerically approximate this integral, which in spherical coordinates is expressed as follows:

$$\iint |F(\theta,\phi)|^2 d\Omega = \int_{-\pi}^{\pi}\int_{0}^{\pi} |F(\theta,\phi)|^2 sin\theta\, d\theta\, d\phi \tag{C.4}$$

Firstly, the antenna studied in this thesis exhibit strong rotational symmetry due to the sequential 90° rotation of the base radiating element. A detailed examination of the differences between the radiation patterns for $\phi = 0°$ and $\phi = 45°$, shows that

the assumption of a rotationally symmetric pattern is legitimate for evaluating the directivity with sufficient accuracy. The integral to be calculated can thus be expressed in the following form:

$$\iint |F(\theta,\phi)|^2 d\Omega = 2\pi \int_0^{\pi} |F_{\phi=0}(\theta)|^2 sin\theta \, d\theta \tag{C.5}$$

The second simplification consists of numerically approximating the integral to be calculated, as follows:

$$\iint |F(\theta,\phi)|^2 d\Omega = 2\pi\Delta\theta \sum_{\theta=0}^{\pi} |F_{\phi=0}(\theta)|^2 sin\theta \tag{C.6}$$

where $\Delta\theta$ is the sampling step in θ. Therefore, the directivity of the antenna presented in this thesis can be calculated using the following formula:

$$D(\theta,\Phi) = \frac{2}{\Delta\theta} \cdot \frac{|F(\theta,\phi)|^2}{\sum_{\theta=0}^{\pi} |F_{\phi=0}(\theta)|^2 sin\theta} \tag{C.7}$$

Personal publications

Journals

S. Chenaoui, L. Mouffok, S. Hebib, A. Fattouche, D. Allane, S. Tedjini. Gain stability improvement of a wideband antenna using an artificial magnetic conductor. *Microwave and Optical Technology Letters*, 65(8), 2267-2277, 2023.

S. Chenaoui, L. Mouffok, S. Hebib. Low profile UHF-RFID reader antenna with high front-to-back ratio. *Progress In Electromagnetic Research Letters*,122, 15-20, 2024.

S. Chenaoui, L. Mouffok, S. Hebib, P.L. Auger, D. Allane, S. Tedjini. Miniaturization of a multiband pyramidal antenna using AMC reflector for satellite applications. *Submitted in International Journal of Communication Systems* , 2024.

International conferences

S. Chenaoui, L. Mouffok, S. Hebib. Investigation of an octagonal AMC reflector backed wideband antenna for gain stabilization. *In 2023 International Conference on Advances in Electronics, Control and Communication Systems (ICAECCS)* (pp. 1-5). IEEE, Algeria, March 2023,.